PLASTICITY OF NANOTWINNED ALUMINUM AND ALUMINUM ALLOY

A Dissertation

by

SICHUANG XUE

Submitted to the Office of Graduate and Professional Studies of
Texas A&M University
in partial fulfillment of the requirements for the degree of

DOCTOR OF PHILOSOPHY

Chair of Committee,	Xinghang Zhang
Co-Chair of Committee,	Hong Liang
Committee Members,	Haiyan Wang
	Choongho Yu
Head of Department,	Andreas A. Polycarpou

August 2017

Major Subject: Mechanical Engineering

ABSTRACT

Nanotwinned (nt) metals have been intensively studied and has shown unique mechanical properties, including high strength and high ductility. Although twins can be introduced into face-centered-cubic (fcc) metals by annealing (annealing twins), deformation (deformation twins) and growth (growth twins), most of these twinned metals have low stacking fault energy (SFE). The twinnability of fcc metals remains largely controlled by their SFE. Consequently, the high SFE of Al typically prohibits the formation of twins in aluminum (Al). This dissertation focuses on the introduction of several innovative strategies that can introduce high density growth twins in Al and Al alloys and study the influence of twinnability on strengthening and plastic deformation of these twinned alloys.

The growth twins were observed in a polycrystalline Al thin film fabricated by magnetron sputtering. And the twin formation mechanism was discussed in a thermodynamic view. Then, we show that high-density twin boundaries can be introduced in Al films by tailoring the texture of the films without any seed layers. Transmission Kikuchi diffraction and transmission electron microscopy studies on (111), (110) and (112) textured Al films. Epitaxial Al (112) film has the highest density of ITBs, because the twin variants (335) and (535) are separated by Al (102) islands, promoting the formation of ITBs. The smaller domain size can thus be achieved by introducing HAGBs into the twinned bicrystal structure to inhibit the abnormal growth of single variant. Furthermore, twin boundaries in Al appear to be stronger barriers to dislocations than

conventional high angle grain boundaries. Besides tailoring the twin structure by changing the growth orientation, alloying has been used in an Al matrix. The high strength epitaxial AlMg alloy has been fabricated with a high density twinned structure. The strong ITB barriers play an important role to strengthen the film. Combined with the solid-solution strengthening, the calculated flow stress correlated well with the experimental data.

The knowledge derived from this study may facilitate the design of high-strength, light-weight, and ductile Al alloys.

DEDICATION

This dissertation is dedicated to:

My parents, Enpei and Jun

My fiancee, Yating

ACKNOWLEDGEMENTS

Firstly, I want to express my sincere gratitude to my advisor, Prof. Xinghang Zhang, for his patience, encouragement, and immense knowledge. I would like to thank my committee members, Drs. Hong Liang, Haiyan Wang, and Choongho Yu, for their guidance and great suggestions that helped me to produce good results in the pursuit of my degree. Many thanks to Dr. Wang for sharing her laboratory facilities.

I appreciate all the help from the Mechanical Engineering department staff at Texas A&M University. Their patience and motivation impress me. I wish the best for you.

I am also grateful to Drs. Yue Liu and Youxing Chen at Los Alamos National Laboratory, Dr. Daniel Bufford at Sandia National Laboratory, Dr. Kaiyuan Yu at the China University of Petroleum. Without their help and guidance, I wouldn't have been able to go further.

Thanks to Dr. Winson Kuo at Materials Characterization Facility of Texas A&M University. Without his dedicated support, I would not get any useful EBSD data.

Thanks also go to my friends and colleagues, Zhe Fan, Jin Li, Qiang Li, Jie Jian, Jijie Huang, Fauzia Khatkhatay, Ruizhe Su, Jie Ding, Cuncai Fan, Yifan Zhang, Zhongxia Shang, and Jaehun Cho, from Texas A&M University and Purdue University for helping me a lot on my research and their companionship through my graduate school journey.

Finally, thanks to my mother and father for their encouragement and my fiancee for her patience and love.

CONTRIBUTORS AND FUNDING SOURCES

This work was supervised by a dissertation committee consisting of Professors Xinghang Zhang (advisor), Hong Liang (co-advisor), and Choongho Yu of the Department of Mechanical Engineering and Professor Haiyan Wang of the Department of Electrical & Computer Engineering.

I acknowledge funding from the DoE-OBES under grant no. DE-SC0016337. H. I also acknowledge the Texas A&M University Microscopy Center and Materials Characterization Facility for the use of numerous microscopes and other instruments.

NOMENCLATURE

NC	Nanocrystalline
UFG	Ultrafine grained
CG	Coarser-grained
PVD	Physical vapor deposition
GMR	Giant-magneto resistance
CLS	Confined layer slip
FCC	Face centered cubic
CTB	Coherent twin boundary
ITB	Incoherent twin boundary
GB	Grain boundary
MD	Molecular dynamics
GSFE	Generalized stacking fault energy
RAP	Random activation of partials
CVD	Chemical vapor deposition
EDX	Energy dispersive X-ray
EELS	Electron energy loss spectroscopy
STEM	Scanning transmission electron microscope
EBSD	Electron backscatter diffraction
TKD	Transmission Kikuchi Diffraction
SEM	Scanning electron microscope

τ	Applied stress
v	Poisson ratio
μ	Shear modulus

TABLE OF CONTENTS

Page

LIST OF FIGURES

Page

CHAPTER I

INTRODUCTION

I.1 Historical perspective

I.1.1 Size dependent strengthening

The grain size dependence of strengthening in metallic materials has attracted significant attentions since Hall [1] and Petch [2] found the phenomenon empirically that smaller grains lead to greater mechanical strength. The Hall-Petch strengthening model is typically described by

$$\sigma_y = \sigma_0 + kd^{-n} \qquad \text{Equation 1}$$

Here, σ_y is the yield stress of the material, σ_0 is the friction stress, k is the Hall-Petch slope, d is the grain size, and n is a constant, typically ~ 0.5. In equation 1, σ_0 represents the stress to move the dislocations along their slip plane based on the Peierls [3] and Nabarro's [4] calculation, which is also known as the Peierls-Nabarro force. The Hall-petch slope, k, represents the barrier strength of the grain boundary to slip transmission of dislocations based on the dislocation pile-up model, while the d^{-n} quantifies the contribution from grain boundary spacing.

When grain boundaries act as the dislocation obstacles, the dislocations emitted from a source inside the grain pile up against the grain boundaries along the slip plane. The number of dislocations (N) pile-up against the boundaries under an applied shear

stress, τ, scales with the distance between source and boundaries (L), which is shown as the equation 2 below [5].

$$\mathrm{N} = \frac{\pi L(1-v)(\tau-\tau_0)}{\mu b}, \qquad \text{Equation 2}$$

Where μ is the shear modulus, v is the Poisson ratio, b is the magnitude of Burgers vector, τ_0 is the lattice friction stress. Once the leading dislocation in the pile-up is able to pass through the boundaries or can trigger a glide dislocation on the other side of the boundaries, the pile-up stress is equal to the barrier strength τ^* of the boundaries for the slip transmission and can be described as

$$\mathrm{N}(\tau - \tau_0) = \tau^*, \qquad \text{Equation 3}$$

Based on the equation 2 and 3, the applied shear stress can be rewritten as:

$$\tau = \tau_0 + (\frac{\tau^* \mu b}{\pi(1-v)L})^{1/2}, \qquad \text{Equation 4}$$

Comparison to equation 1 yields $k = (\frac{\tau^* \mu b}{\pi(1-v)})^{1/2}$. Thus, by measuring the Hall-Petch slope, the barrier strength τ^* can be calculated. Since the parallel dislocations (in the pile-up) with the same sign repel with each other, the number of dislocations in the pile-up is confined by the grain size.

Consequently equation 3 indicates that the less the dislocation pile-ups against the boundaries, the higher the applied stress, τ, to trigger the slip transmission.

A dispersed network of obstacles also can block mobile dislocations and the strengthening effect can be expressed by the Taylor dispersed barrier strengthening model

$$\Delta\sigma_y = \mu b\sqrt{\rho}, \qquad \text{Equation 5}$$

where ρ is the barrier density and the $\Delta\sigma_y$ is the increment of the yield strength. The Taylor dispersed barrier strengthening model and Hall-petch model describe two major strengthening mechanisms in metallic materials, and have proved to be successful to predict the strength of the metal.

I.1.2 Strengthening at the nanoscale

Following the Hall-Petch relationship on size dependent strengthening, it is natural to ask is it possible to achieve high strength in metals by reaching a minimum grain size? Researchers employed various material fabrication methods to tailor the grain size from micro level to nanometer level, and successfully synthesized nanocrystalline (NC , grain size < 100 nm) and ultrafine grained (UFG , 100nm <grain size < 1000nm) metals. Over a wide range of the grain size (> 100 nm), the Hall-petch relationship in general predicates the strength of the materials well. Indeed, NC metals often exhibit dramatically higher yield strength compared to their coarser-grained (CG) counterparts [6]. However, the Hall-Petch relationship breaks down for the smaller grains when grain size d < 20nm, because dislocation sources and pile-up are not expected to operate inside these tiny nanograins due to both grain size effect and the much higher fraction of GBs [7-11]. Hence, other than significant dislocation activities, GB shear, rotation, and sliding in NC metals can be activated to facilitate the plastic deformation. The rapid sequence of initial grain realignments has been observed by in-situ TEM tensile tests in NC nickel [12]. Moreover, using *in-situ* high-resolution TEM tensile studies on NC Pt shows that the dislocation climb is the underlying mechanism of grain rotation instead of the GB sliding or the

diffusional creep [13]. Recently, K. Lu et al. reported ultrahigh hardness NC NiMo alloy by suppressing the GB-mediated process, which confirmed the crucial role of the stable GBs in determining the plastic flow and hardness of NC materials [14].

The ultrahigh strength of NC metals is often accompanied by substantial reduction of ductility due to tensile or shear instability [6, 15]. Moreover, high density GBs can lead to the degradation of corrosion resistance, thermal stability, and the electrical conductivity because of the higher interfacial energies of GBs. Therefore, grain boundary engineering that replaces high energy GBs by low energy interfaces attracted increasing attention.

I.1.3 Layer interface strengthening mechanisms

The mechanical behaviors of multilayers fabricated by physical vapor deposition (PVD) techniques have drawn broad attention. The ability to fine tune the layer thickness as small as 1 nm is well suited for the fundamental studies on the effects of length scale on strengthening mechanisms in multilayer composites [16, 17]. Various vapor deposited multilayer systems, such as metal-metal [18-22]and metal-intermetallic [23], have been investigated and prominent size effect has been reported. For example, although bulk Cu and Ni have low yield strength (10-50 MPa), Cu/Ni multilayers shows high flow stress, ~ 2 GPa, when individual layer thickness is 2.5 nm [21]. Furthermore, abundant metallic multilayer films have shown giant-magneto resistance (GMR) [24, 25], good mechanical deformability and high strength [26, 27], and remarkable radiation tolerance [28, 29].

There are three major types of interface strengthening models for metallic multilayers. The schematic in Fig. 1.1 illustrates these three different strengthening mechanisms at different individual layer thickness (h). When h is larger than 50 nm, the

Hall-Petch type dislocation pile-up mechanism dominates the strength of multilayers. When 50nm > h > 10nm, Dislocation cannot form a pile-up in these fine layers. Instead, the confined layer slip (CLS) mechanism operates, which needs less applied stress to activate the migration of dislocations, compared with the dislocation pile-up model. In CLS regime, single dislocation loops propagate parallel to the interfaces. When h is less than 5 nm, the CLS is superseded by single dislocation dominated interface crossing mechanism and the maximum hardness is obtained in most of the metallic multilayer films at this region. The interface barrier strength for the single glide dislocation transmission is independent of the h, but could drop when the core size of dislocations is on the order of h. Multiple factors, such as Koehler stress[30, 31], twining [19, 21, 32, 33], texture [18], misfit dislocation [34-38], and interface shear strength [39, 40], contribute to the interface barrier strength in metallic multilayers.

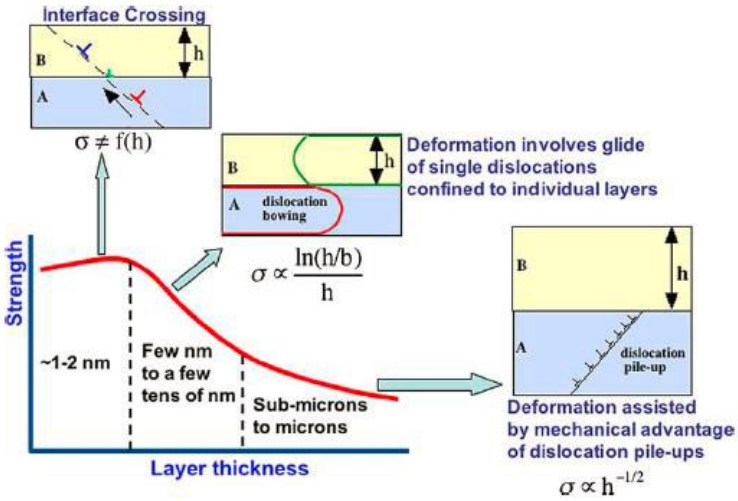

Figure 1.1 Schematic of the strengthening mechanisms in metallic multilayer at varying individual layer thickness [5].

To present a clear picture on the interface barrier strength models, the following section will list several factors that are major contributors to the barrier strength. The lattice parameter difference between multilayers can generate coherency stress or misfit dislocations based on the magnitude of mismatch strain. When the lattice mismatch strain is small (<1%), the elastic strain between the interface can accommodate the lattice mismatch to maintain coherency at interface. The elastic strain energy builds up with increase of the layer thickness. The critical layer thickness h_c to form a misfit dislocation can be calculated by [41]

$$h_c = \frac{b}{2\pi f}\frac{(1-v\cos^2\alpha)}{(1+v)\cos\lambda[\ln(\frac{h_c}{b})+1]}, \qquad \text{Equation 6}$$

Where f is mismatch strain, v is Poisson's ratio, and α is the angle between the dislocation line and Burgers vector. If the interface mismatch strain is less than 5%, a semi-coherent interface can form with misfit dislocations along the interface to release the long range coherency stresses [42]. An interface with mismatch strain greater than 5% often loses coherency and results in incoherent interface without coherency stresses. Compared with coherent systems, incoherent interfaces are more effective to block the dislocation transmission due to dislocation slip discontinuity [43].

Koehler stress is due to the elastic modulus difference between adjacent layers and affect the barrier strength significantly if there is a large modulus discrepancy [30]. The difference in stacking fault energy (SFE) can also affect interface barrier strength, which is illustrated in figure 1.2. Two multilayer system, Cu/Ni and Cu/Co, are compared. The SFE for Cu, Ni, and Co are 45, 125, and 24 mJ/m^2, respectively. In Cu/Ni system, the

partials transmission from Cu to Ni is difficult due to the higher SFE in Ni. To accommodate plastic flow by the slip of dislocations, two partials may have to constrict into one full dislocation before the dislocation transmission into Ni layer. Whereas in Cu/Co system, the partials can slip across the interface without any constriction. So the SFE difference can contribute to the interface barrier strength [44].

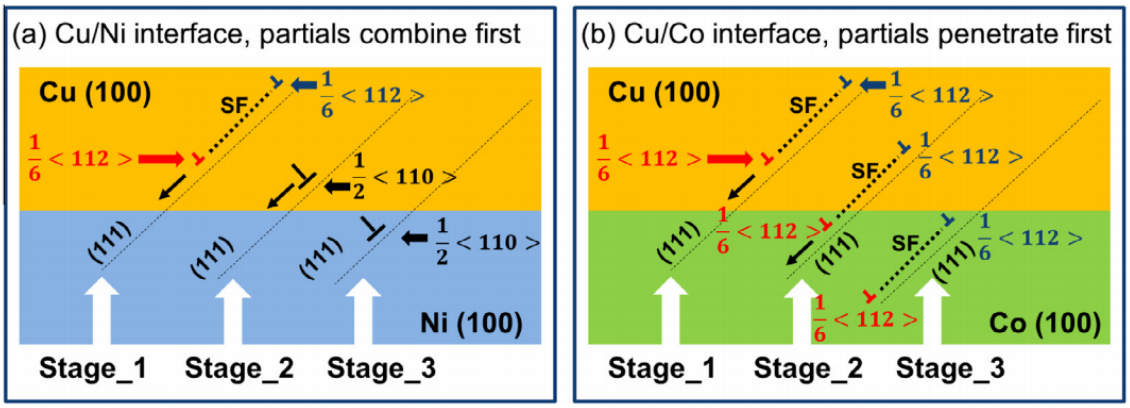

Figure 1.2 Hypothetical schematics show the partials transmissions difference between Cu/Ni and Cu/Co systems. (a) In Cu/Ni, partials need to be constrained into full dislocation to transport through the layer interface due to the high SEF of Ni. (b) In Cu/Co system, partials can slip across layer interface without the constriction [44].

The multilayer structure can successfully strengthen the film by introducing the interphase in an accurate way. However, multiple phases raise processing complexity and cost. The inhomogeneity of materials can trigger crack initiation and stress concentration, and reduce thermal conductivity. To avoid phase segregation and inhomogeneity induced by the disparity in chemical potentials, single-phase materials (elemental metals, solid solution alloys) are preferred in many applications. The emergence of new material

processing techniques enhances the capability on the microstructure control of single-phase materials. Because of the versatile material processing techniques especially at nanoscale, high strength, ductile single-phase materials have been fabricated recently.

I.1.4 Strengthening in single-phase materials

I.1.4.1 Special grain boundary strengthening

As mentioned in section I.1.1, GBs provide a substantial strengthening effect for materials. However, dislocation transmission is a vague description without any detail on the process of GBs and dislocations interaction. Especially, at the atomic scale, the various types of GBs have different response to the dislocations caused by different energy barriers strength. Is there any special GB can provide high barrier strength and also prevent stress concentration? To answers this question, the individual GBs mechanical behavior need to be understood. But, it is hard to observe the mechanical behavior of individual GBs experimentally. The MD simulation sheds light on the understanding of the physics process of the dislocation- GB interaction for each specified GBs. Based on the MD result, the energy barriers related to the dislocation nucleation and transmission has been calculated and the GBs with lower interfacial energy have been identified as the effective interface to provide a stronger barrier for the slip transmission [45].

Figure 1.3 shows the calculated GB energy profile for several types of GBs in Ni. Three types of GBs are compared, <110> tilt boundary, <001> tilt boundary and <111> twist boundary. Special Σ GBs are defined based on the coincident site lattice (CSL) concept, which is derived from the ratio of the overall number of atoms at the interface to

the atoms that are in coincidental sites at each lattice. Σ3 GBs have the lowest energy, which can be obtained via a 60° twist along <111> axis or 109.47° tilt along <110> axis. These Σ3 GB is also known as twin boundaries (TBs).

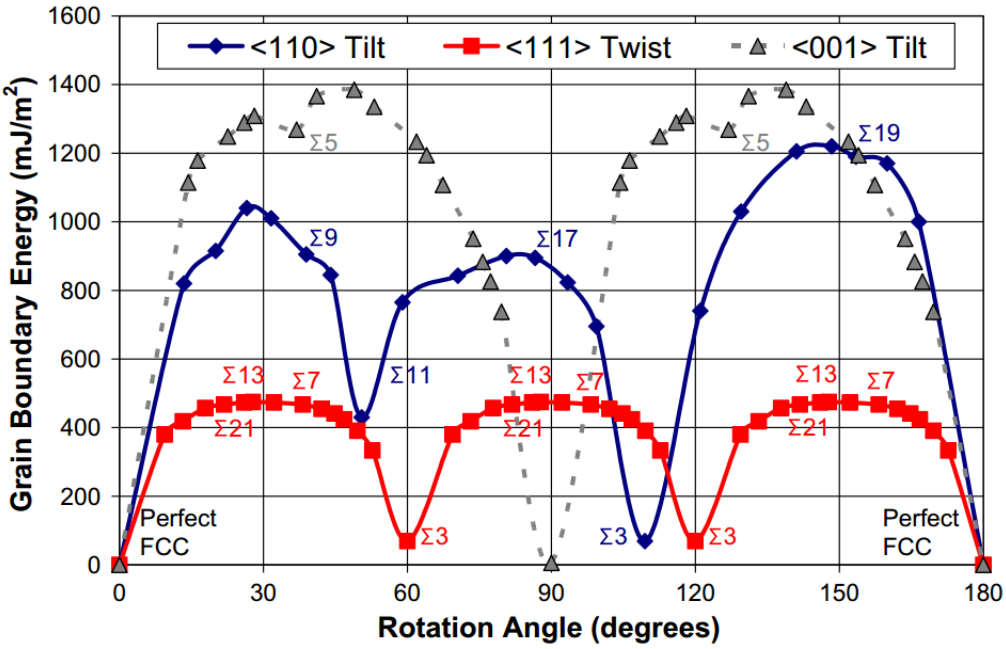

Figure 1.3 The grain boundary energy profile for various GBs generated by tilting along <110>, <001> and twisting along <111> orientations in Ni constriction [45].

Face centered cubic (FCC) metals have two types of , Σ3 GBs, Σ3(111) coherent twin boundary (CTB) and Σ3(112) incoherent twin boundary (ITB). The low GB energy of TBs arises from their coherent structure and less free volume at the interface as shown in Figure 1.4(b).

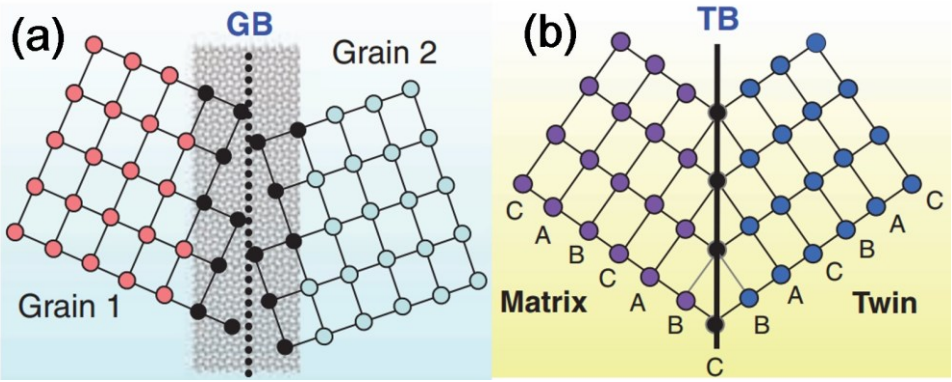

Figure 1.4 The schematics of normal grain boundary and coherent twin boundary. (a) A typical grain boundary. (b) Coherent twin boundary [46].

CTBs, ITBs and normal GBs have dramatically different interfacial energies because of their different structure configurations. For instance, the interfacial energy of CTB and ITB in Al is 75 [47] and 223-357 mJ/m^2 [48, 49] respectively, whereas a normal grain boundary energy is ~ 1000 mJ/ m^2 [50]. The low energy of CTBs indicates that CTBs are thermodynamically more stable than normal GBs.

As shown in figure 1.5, metals with high-density twin structures (twin spacing < 100 nm) show not only high strength, but also good ductility, resulting from the hardening of TBs when they continuously lose coherency under plastic deformation [51, 52]. It is quite different from nc metals that typically have high strength but low ductility. As shown in Fig. 1.5, nc Cu has higher strength but poorer ductility compared to polycrystalline coarse-grained Cu, due to the suppression of dislocation-mediated plasticity in small grains.

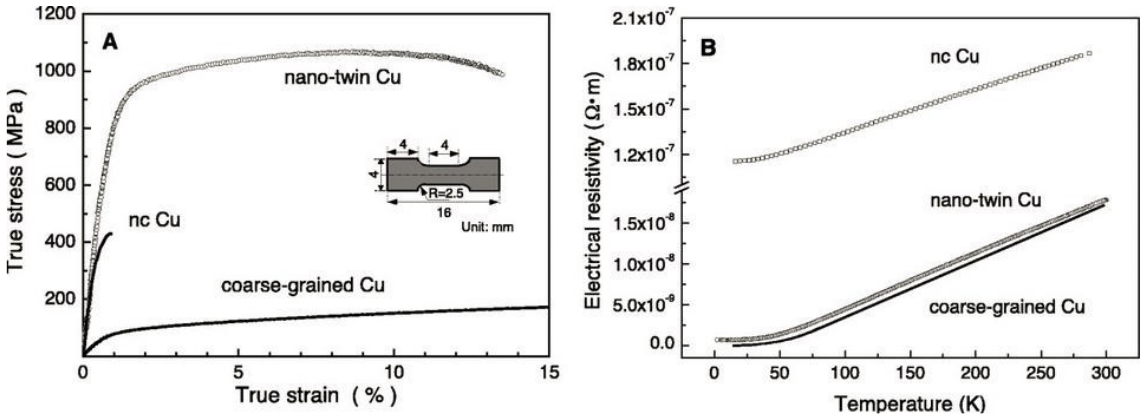

Figure 1.5 (a) Tensile test for the nanotwinned Cu, nanocrystalline Cu, and coarse-grained Cu; (b) electrical resistivity change with the increase of temperature for nanotwinned Cu, nanocrystalline Cu, and coarse-grained Cu [52].

Moreover, the electrical resistivity of nt Cu is nearly identical to that of coarse-grained Cu, whereas the nc Cu has a much higher electrical resistivity due to the high density GBs that scatter electrons significantly [52]. Similarly, as figure 1.6 shows, softening also happens in nc Cu when the twin thickness is below 15 nm [53]. To understand the softening mechanism in nt Cu, MD simulations have been employed [54]. Based on the MD simulation result, the classical Hall-Petch strengthening due to the pile-up and transmission transforms to a dislocation-nucleation-controlled softening phenomenon resulting from TB migration triggered by the slip of partials along TBs when the twin spacing is less than 10 nm.

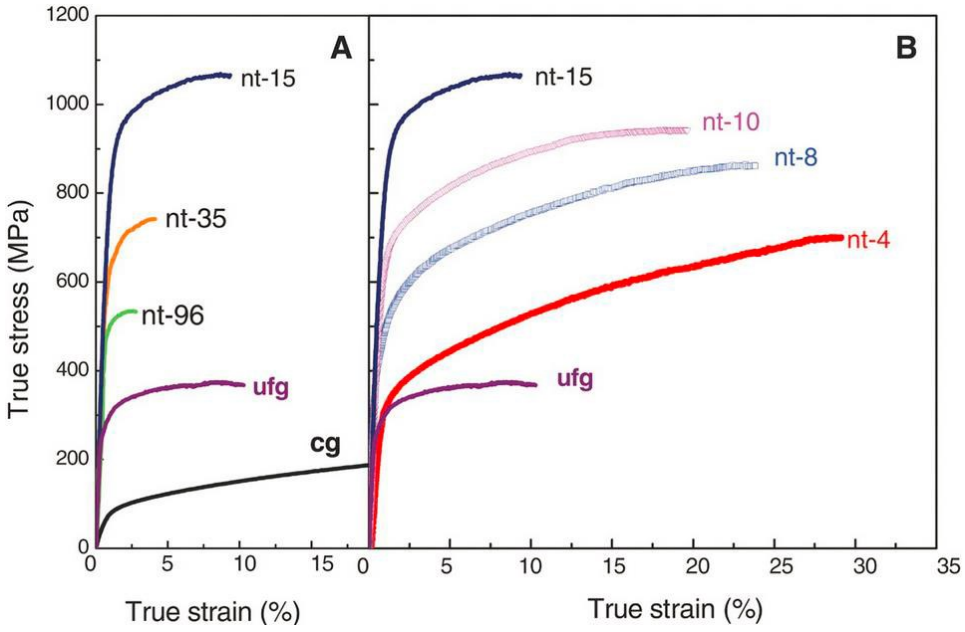

Figure 1.6 Tensile test of Cu with different twin density (same grain size) [53].

I.1.4.2 Heterogeneous nanostructured metals

Recently, heterogeneous nanostructures have been found promising to promote strength-ductility synergy due to the mixture of soft and hard regions [55, 56]. As shown in figure 1.7, the strength-ductility synergy is achieved via combination of coarse grains and nc grains. Soft regions have better ductility than hard regions with small grains, so that strain gradients develop during plastic deformation. To accommodate the strain gradients, geometrically necessary dislocations (GNDs) build up, leading to enhanced work hardening [57].

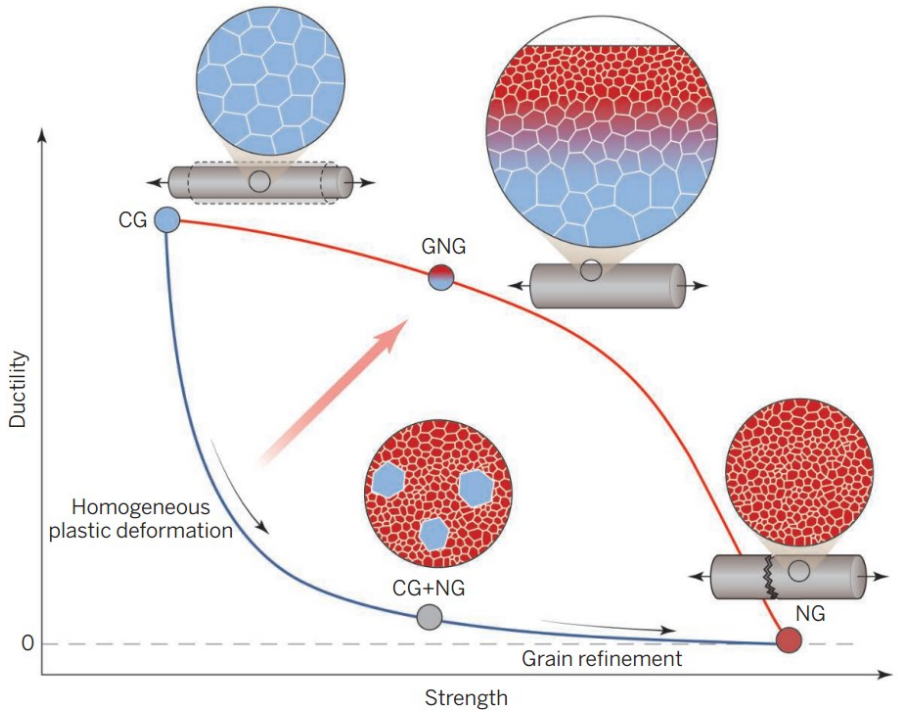

Figure 1.7 Strength-ductility synergy. The coarse-grained metals have good ductility with lower strength whereas the nanocrystalline metals have the opposite phenomenon. The similar strength-ductility trade-offs happen for random mixtures of nanograins and coarse grains. By introducing the gradient structure, the strength-ductility synergy is obtained) [55].

In this section, we overview the strengthening mechanisms for different interfaces and structures. When the grain size is less than several nanometers, the strength of nc metals deviated from the Hall-Petch slope due to the transformation of deformation mechanisms. Compared to the nc metals, the multilayer films show more details on the factors which can contribute to the interface barrier strength. Moreover, the Σ3 TBs are introduced as a way to achieve the strength-ductility synergy which is also can be attained by the gradient nc structure. In next section, we will focus on the formation mechanism of twin since it is a promising structure to strength the material with less loss of ductility.

I.2 Formation mechanisms of twin boundary

The term “twin” refers to a special crystal interface in which the crystal structure has a symmetrical relation on either side. In face-centered cubic (fcc) metals, the twin structures can be induced by annealing, deformation, and growth process. Since k. Lu [52] reported the ultrahigh strength Cu with high-density nanoscale growth twins, nt metals have attracted intense attention and showed various unique properties. Cu with nanotwins have excellent electrical conductivity [52, 58] while maintaining high mechanical strength. Nt metals, such as Cu and Ag [59-62], also show better thermal stability than monolithic NC metals [63-65]. The mechanical properties of nt metals have also been extensively studied, and certain nt metals have shown high strength and high ductility [52-54, 59, 66-70]. Since these appealing mechanical properties are induced by nanotwins, it is critical to understand the formation mechanism of twins to guide the synthesis of nt metals. In the following section, the formation mechanism of growth twins in fcc metal will be discussed. We will focus on two types of TBs, the Σ3 {111} coherent twin boundary (CTB) and Σ3 {112} incoherent twin boundary (ITB).

I.2.1 Formation mechanism of coherent twin boundary

I.2.1.1 Growth twin formation mechanisms

In fcc metal, the atomic stacking sequence along [111] is abcabc. During the growth process, if atoms land in the wrong position by growth accidents, a stacking fault will

form. Consecutive growth accidents will lead to the formation of twin embryo, and the stacking sequence may become abcabc|bacb. The Capital C indicate the TB and the onset of wrong stacking. According to the general description of the growth process of twin, the stacking fault energy (γ_{sf}) plays an important role in controlling the formation probability of twin nucleus. The higher the SFE, the lower the twin formation probability. Thus most studies on nt metals have focused on the low γ_{sf} metals. From a thermodynamics point of view, Zhang et al. [19] postulated a model to calculate the probability of forming a twinned nucleus during vapor-to-solid transformation using magnetron sputtering. The twin formation probability is proportional to the critical radius difference between a perfect and twinned nucleus. If the difference is small, the twinned nucleus has a high possibility to survive, which means the twin fraction in the metal will increase considerably. In detail, the critical radius of the perfect nucleus and twinned nucleus can be expressed as:

$$r^*_{perfect} = \frac{\gamma}{\Delta G_V} = \frac{\gamma}{\left(\frac{kT}{\Omega} ln\left[\frac{J\sqrt{2\pi mkT}}{P_S}\right]\right)} \quad \text{Equation 7}$$

$$r^*_{parallel} = \frac{\gamma}{\Delta G_V - \frac{\gamma_t}{h}} = \frac{\gamma}{\left(\frac{kT}{\Omega} ln\left[\frac{J\sqrt{2\pi mkT}}{P_S}\right] - \frac{\gamma_t}{h}\right)} \quad \text{Equation 8}$$

where the r and h are the respective nucleus radius and height. γ is the surface energy and ΔG_V is the bulk free energy difference between solid and vapor per unit volume driving the nucleation. γ_t is the respective energy of CTB. k is the Boltzmann constant, Ω is the atomic volume and T is the substrate temperature, J is the deposition flux, m is the atomic mass of the deposited metal, P_S is the vapor pressure above solid. The critical radius difference between the parallel (or inclined) twin nucleus and the 'perfect' nucleus is expressed as

$$\Delta\gamma_{pp}^{*} = \gamma_{para}^{*} - \gamma_{perfect}^{*} \qquad \text{Equation 9}$$

According to the equations (7), (8), and (9), either low TB energy or high deposition flux promotes the formation of growth twins in metal by physical vapor deposition. Fig. 1.8 (a) shows the influence of deposition rates on the critical radius difference between perfect nucleus referring to the perfect crystal structure without defects and twin nucleus referring to CTB structure in the film. The highly twinned Ag film is shown in Fig. 1.8(b)[60].

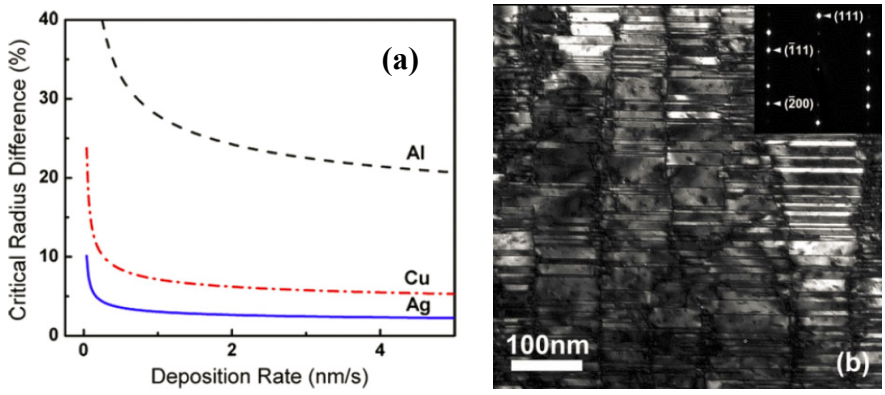

Figure 1.8 (a) The plot of radius differences between perfect and twin nucleus at different deposition rates; (b) the transmission electron microscope image of highly twinned Ag film, the straight line indicated the TBs form edge-on view (Reprinted from [60], Copyright (2011), with permission from Elsevier).

Anderoglu [71] et al. deposited pure Cu at different deposition rates by magnetron sputtering. As shown in Fig. 1.9, the twin spacing decreases when the deposition rate increases, which correlates well with the chart in Fig. 1.8(a). Increasing the deposition rate can decrease the critical radius difference, and thus results in the higher twin formation

possibility due to the smaller twin critical nucleus radius. If we can make the two critical radius comparable, the twin fraction will rise considerably. In addition to the thermodynamics view, the formation of twins can be interpreted from kinetics point of view. General speaking, at low deposition rates, incoming atoms landed on the surface of the film have sufficient time to diffuse to the perfect lattice sites to achieve the lowest potential energy. In contrast, higher deposition rate leads to reduced diffusion time for adatoms, and thus promote the formation of more growth defects.

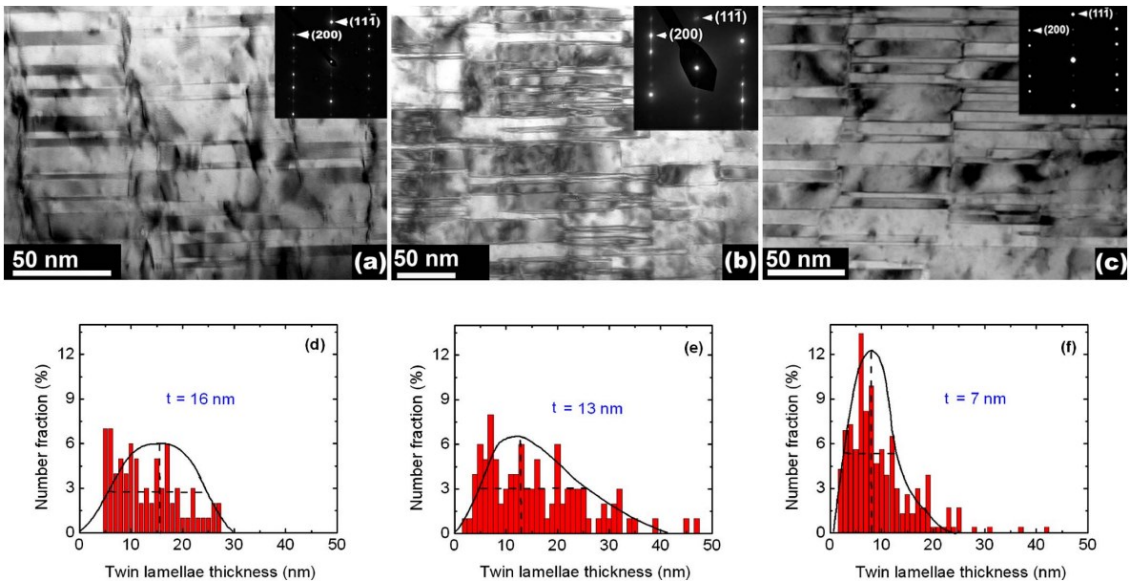

Figure 1.9 Cross-section TEM images of pure Cu with different deposition rates. (a) 0.9 nm/s, (b) 3nm/s, (c) 4nm/s. (d)-(f) statistical distribution of twin spacing in deposited Cu film at different deposition rates, correspondingly [71].

For monolithic fcc metals with low SFE, magnetron sputtering works well to introduce high-density growth twins. However, it is difficult to induce high-density CTBs into metals with high SFE as indicated in Fig. 1.8(a) Al has a large critical radius difference even at high deposition rate (4nm/s) due to its high SFE (166 mJ/m^2). The epitaxial growth of thin film by PVD has provided another approach to promote the formation of growth twin. A systematic study on various metallic multilayers leads to two criteria to introduce growth twins into high SFE metals [72]. The first criterion emphasizes the need for a low SFE buffer layer that can readily form high-density twin seeds; and the second criterion highlights the significance of global coherency between coherent similar interface (between constituents with identical planar indices) or local coherency between coherent dissimilar interfaces (between constituents with different planar indices) that allow twins to propagate across layer interfaces.

Liu [73] postulated the twin nucleation mechanism via shear stress induced Shockley partials. More specifically, in the Cu/Ni multilayer system, incoming atoms land on the terraces of islands and diffuse to the equilibrium sites. With the increase of film thickness, as shown in Fig. 1.10, there is no stress at the surface of the free edge. Nevertheless, the biaxial stress builds up quickly inside the island due to the mismatch strain between film and substrate. The mismatch stress between Cu and Ni is transferred by shear stress. The shear stress at the corner of the islands may facilitate the formation of partials and the slip of the partials. The consecutive slip of partial dislocation may promote the formation of a twin. The shear stress generated by the mismatch stress can be roughly estimated as follows [74]

$$\tau \approx \sigma_m \sqrt{\frac{kh_f}{2\pi x}} \qquad \text{Equation 10}$$

where σ_m is the biaxial mismatch stress in films, h_f is the film thickness, and x is the distance from film edge. k is the biaxial modulus ratio, it can be calculated by

$$k = \frac{\frac{E_S}{1-v_S}}{\frac{E_f}{1-v_f}} \qquad \text{Equation 11}$$

where E and v are the modulus and Poisson's ration of substrate and film. At the location away from film edge, the shear stress at the interface of Cu and Ni drop quickly compared with the film edge. In the Cu/Ni multilayer, the shear stress is about to be 1.3-2.2 GPa when x is 1-3 times larger than the film thickness, which is high enough to initiate the slip of partial dislocation (540 MPa is necessary to create the Shockley partials in Cu).

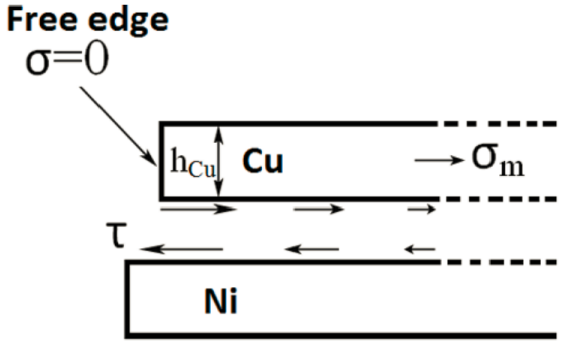

Figure 1.10 Schematics for shear stress in Cu/Ni multilayer interface [73].

Besides the epitaxial mechanism and shear stress induced nucleation of growth twins in high SFE Ni (125 mJ/m^2), Zhang [75] et al. fabricated high-density twins in Ni by electrodeposition. Parallel nanotwins and parallelogram twins were formed under different electrodeposition conditions. However, there is still no comprehensive explanation of twin formation mechanism for electrodeposition process. The high deposition rate may contribute to the twin formation in high SFE fcc metals.

I.2.1.2 Deformation twin formation mechanisms

The dislocation slip accommodates the plastic deformation of metals in most cases. Deformation twinning mechanism can also operate under high strain rate [76-78] or low temperature [79, 80] to accomodate the plastic flow. The followings briefly summarize deformation induced twin nucleation mechanisms.

Homogeneous [81, 82] and heterogeneous [83-85] nucleation are two major characteristics to classify the nucleation of deformation twin. The heterogeneous twin nucleation needs less stress than the homogeneous nucleation [86, 87] and indirect experimental evidence show a good correlation of stress between heterogeneous nucleation models and experiments [86].

I.2.1.2.1 Molecular dynamics (MD) simulations

For deformation twinning in fcc metals, the partial dislocation slip on consecutive {111} planes triggers the formation of deformation twins. The relevant energy landscape for the creation of fault surface is related to the rigid displacements along <112> direction,

also called the generalized stacking fault energy (GSFE) profile. As shown in figure 1.11, the GSFE profiles for various fcc metals, to slip one-half of a crystal structure rigidly about the other half crystal along Burgers vector (1/6[112]), the atoms need to overcome the energy barrier of γ_U which is the maximum energy during the atoms shuffling based on the Peierls dislocation slip concept [3]. γ_I is the stable or intrinsic stacking fault energy and γ_U is the unstable stacking fault energy. The formation of a stable SF is the precursor for the deformation twin nucleation process. Rice divided the formation of a microtwin into two steps [88]. First, GB emits a leading partial due to the high stress concentration and leave an intrinsic SF ribbon behind. Second, another leading partial is emitted from the GBs and slip above the slip plane of first leading partial to form the twin nucleus. After the third leading partial slip on the adjacent plane, a stable microtwin is formed. MD simulations have shown that the microtwin can grow by increasing stress [89]. However, at step two, the emitting of trailing partial dislocation on the identical plane of first leading partial will be favorable under specific circumstances, a process that is related to the SFE, temperature, and strain rate. Thus, the competition between the emitting the second leading partial on adjacent plane and the emitting the trailing partial at the same slip plane of first leading partial is the key criterion for the formation of a deformation twin.

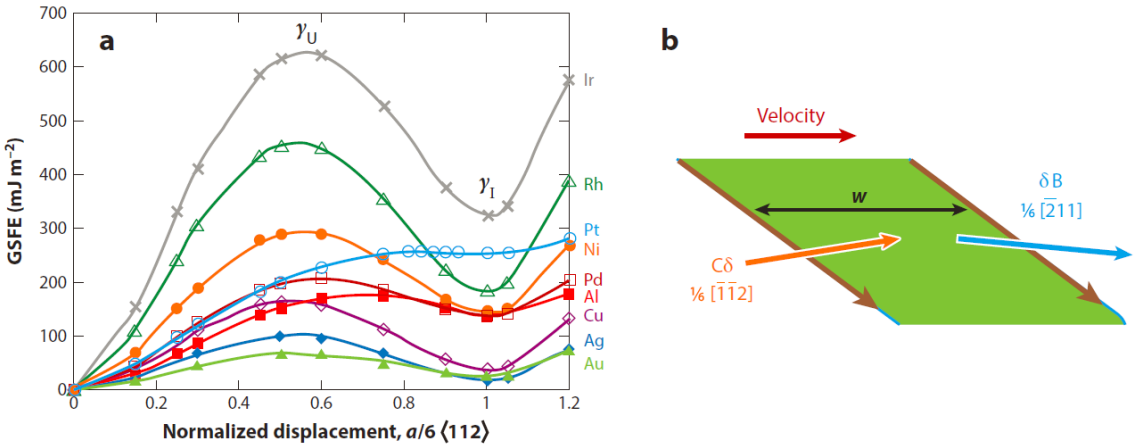

Figure 1.11 (a) The profiles of Generalized stacking fault energy for fcc metals computed by density functional theory. (b) The stacking fault energy is related to the equilibrium width w between two partials on same slip plane [90].

The criterion for the onset of deformation twining in Al under the Pierls framework for the dislocation emission at the crack tip has been calculated by Hai [89]. They found the deformation mechanisms strongly depend on both the loading mode and crystallographic orientation. For the specific loading mode and orientation that maximizes resolved shear stress along the direction of Burgers vector of a partial, the formation of deformation twinning is favorable, whereas the dislocation slip is initiated if the maximum resolved shear stress is along the direction of Burgers vector of a full dislocation. However, the model didn't mention the competition between the twinning and dislocation slip. To quantitatively describe the process of twinning and dislocation slip, a comprehensive model has been built, wherein the twinning tendency is defined as T, T= $\lambda_{crit}\sqrt{\gamma_{us}/\gamma_{ut}}$ [91]. In the equation, the γ_{us} is the unstable stacking fault energy and γ_{ut} is the unstable twinning energy, which is the energy barrier for the formation of twin. λ_{crit} is the

additional energy to emit the trailing partial compared to the leading partial, which is proportional to the γ_{us}/γ_I. So, the metals with high γ_{us}/γ_I ratio are prone to form twin due to the high energy of the emitting of trailing partial dislocation. The second term, γ_{us}/γ_{ut} which delineate the difficulty of deformation twinning relative to the dislocation slip is less than λ_{crit}. It will be difficult to form twin if the ratio is small, which means the high γ_{ut} make the second leading partial hard to emit. In general, when T > 1, the plastic deformation is controlled by the twinning and when T < 1, the dislocation slip dominates the deformation. But, two important factors, the temperature and strain rate, are not considered in this simulation. To correct the model, Warner et al. built a model incorporated the factor of the strain rate and temperature [92]. They confirmed that there is a transition from twining to full dislocation slip when the strain rate decreases. In detail, they calculated the relationship between activation energy for twinning or dislocation slip and strain rate at room temperature shown in figure 1.12. The x axis is the applied stress intensity that correlates to the strain rate, and y axis is the activation energy for trailing partial or twining partial. For extremely high strain rate, even the Al or Pt can form deformation twin instead of the full dislocation slip. If the strain rate is lower than the crossover of the trailing partial and twinning partial, the emitting of trailing partial is more favorable. For low SFE metals, the slip of trailing partials does not means the recombination of the partials, whereas the high SFE metals do favor the recombination of trailing and leading partials.

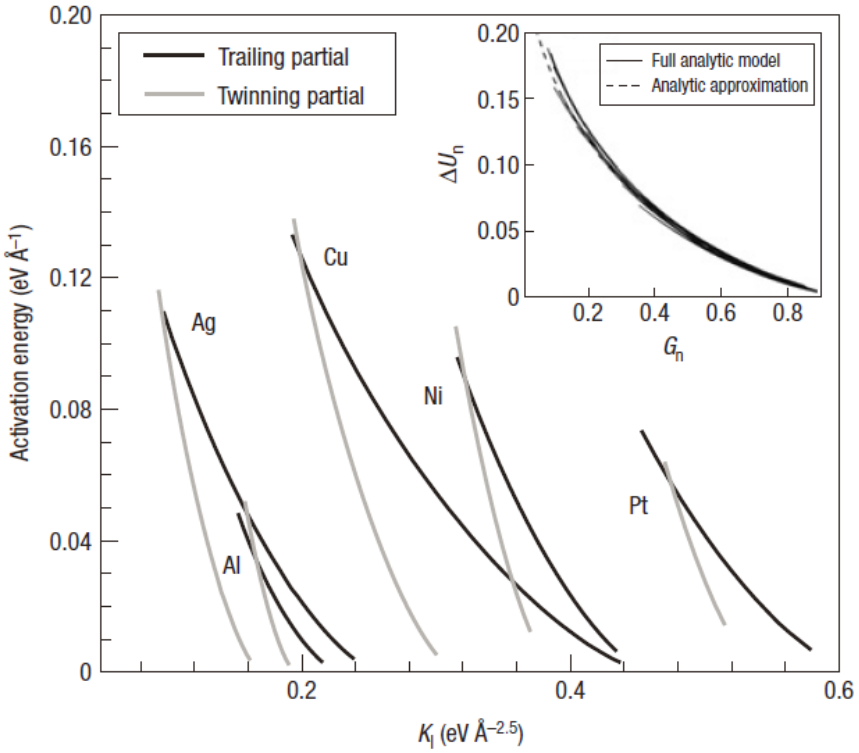

Figure 1.12. The chart for the relationship between the activation energy per unit length and applied strain rate [92].

Although this model can predict the deformation mechanisms of fcc metals at different strain rate, the physical meaning of the transition for twinning to dislocation slip is still not clear. Additionally, the model only focuses on the competition of trailing partial slip and second leading partial slip after the emitting of the first leading partial, which is the precursor to form a stable twin nucleus. Kibey et al. move forward to predict the stress to form a stable twin nucleus in fcc metals [93] and found the monotonic dependence of twinning stress on γ_{ut}.

Different from the models listed above, Yamakov et al. [8, 94, 95] used the separation distance of partials to characterize the twinning tendency in nc fcc metals. If the grain size is less than the separation distance, twinning will be favorable, whereas the dislocation slip will prevail if the grain size is larger than the separation distance. Based on the equation 12, the separation distance r_{split} is controlled by the SFE Γ and applied stress σ. Where b is the Burgers vector of partials, m is the Schmid factor and K is a factor which depends on the Schmid factor and elastic constants. By using a high strain rate deformation to trigger the high stress concentration on GBs, the separation distance of high SFE fcc metals can dramatically increase to several nanometers which is the grain size scale of the nc metals. During high strain rate deformation process in nc Al, a GB or triple junction will emit a leading partial that glides through the grain interior and leave a SF behind. If the grain size is smaller than the separation distance, before the emission of a trailing partial at same slip plane, the leading partial is already wiped out at the opposite GB. That is how a SF can be formed in high SFE metals under high applied stress.

$$r_{split} = K\frac{b^2}{\Gamma - bm\sigma} \qquad \text{Equation 12}$$

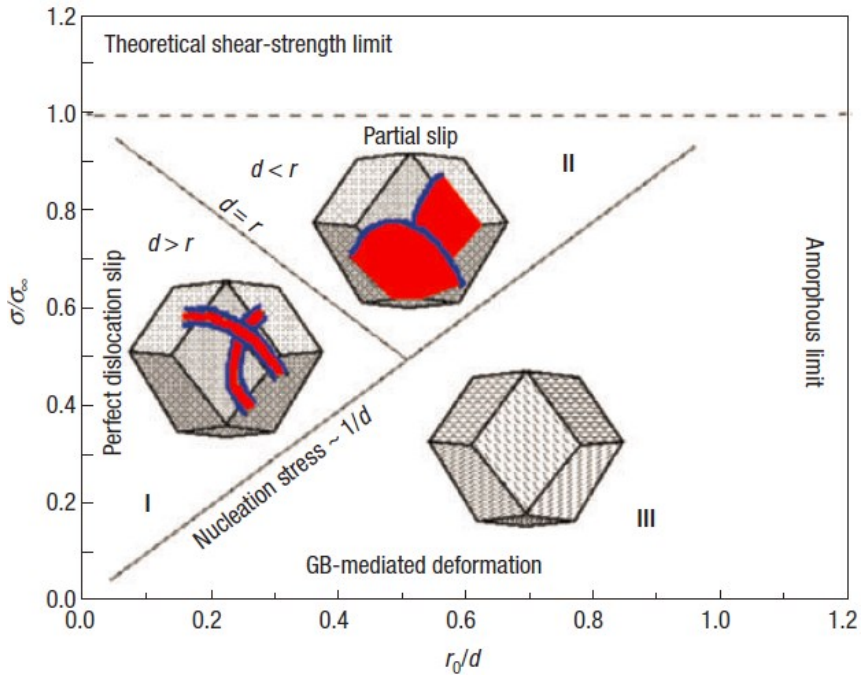

Figure 1.13. The deformation mechanism map including the influence of grain size (x axis) and applied stress (y axis) [8].

Figure 1.13 shows the transition map of deformation mechanisms in nc metals. In region three, the applied stress is less than the partial emission stress, which only triggers the GB-mediated deformation. In region two, the separation distance is larger than the grain size, and thus stable SFs form in the metal. In region one, only full dislocation can be observed due to the small separation distance compared to the grain size. Although the simulation predicts the deformation mechanism transition in nc Al metal well, still there is no clear physical meaning of the competition of twining and full dislocation slip.

Zhao et al. [96] observed the macro deformation twins in single crystal Al under ultra-high strain rate ($\sim 10^6$ s^{-1}) via dynamic equal angular pressing. MD simulation has been employed to decipher the formation mechanism of deformation twin. They found

that the transition from full dislocation propagation to twinning only happen when dislocation activities experience a stagnation due to the formation of dislocation tangles. Then twinning is triggered to accommodate the plastic flow more efficiently based on the different migration velocity of dislocation slip and twinning as shown in figure 1.14.

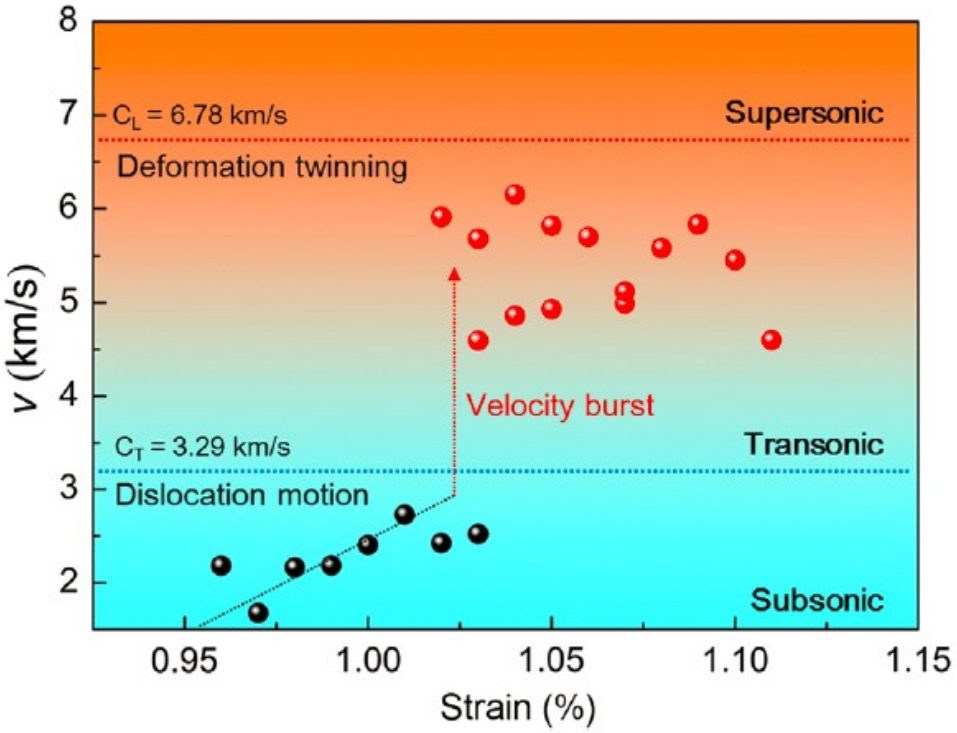

Figure 1.14 The dislocations and deformation twinning speed at different volumetric strain [96].

The speed of leading partial increases at higher strain but still below the transonic. An obvious strain rate burst is captured due to the transition from the dislocation slip to twinning. The transition results from the stress accumulation due to the discrepancy between the high strain rate and low slip velocity, which means the dislocation slip cannot

efficiently accommodate the plastic flow and is replaced by twinning, which has a higher propagation speed.

Another interesting question arises and remains unanswered. Why twinning has a higher velocity than dislocation slip although the essence of twinning is also the dislocation slip?

I.2.1.2.2 Experimental observations of twinning mechanisms

To probe the deformation mechanisms in materials, a combination of MD simulations and experimental observation would be a better strategy than using either method alone. In this section, the different twinning mechanisms are presented below according to the result from experimental observation and MD simulations.

The first one is overlapping of SFs [97, 98]. Two SFs on adjacent slip planes can overlap to form a two atomic layer twin. Although theoretically, this twin structure can grow by forming more SFs on adjacent slip plane in the interior of nc grain, there is still no evidence to show the thicker twins more than two atomic layers. So, the overlapping of SFs may not play an important part in the deformation process of nc metals. The possible reason is the lacking of a continuous growth mechanism that relies on the incidental formation of SFs. The schematics of this mechanism is shown in figure 1.15 A. Besides the formation SFs inside the grain, another variant of the overlapping mechanism has been observed experimentally (Figure 1.15 B). For the B scenario, a SF first nucleates at GB and slipped into grain interior. Then another SF which formed inside the grain slip toward the SF nucleated at GB on an adjacent plane. Incidentally, they partially overlap to form a two atomic layer thick twin. If all the SFs were connected to GBs in two

scenarios, the formation mechanisms may be similar to the normal twin nucleus triggered by a consecutive partial slip from GBs.

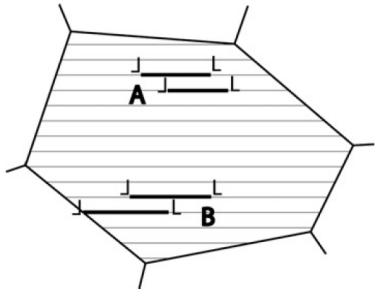

Figure 1.15. The twin formation due to the overlapping of stacking faults. The thin line across the grain is the {111} slip planes, and thick lines represent the stacking faults [99].

The second twin formation mechanism is partial emission from GBs which has been illustrated in MD simulations [8, 89, 91, 95]. The phenomenon has also been confirmed in nc Ni experimentally [100, 101]. This twinning mechanism is the most commonly reported case in fcc nc metals. So, it is vital to understand the process for the partials emission from GBs. Experimental studies show that the non-equilibrium GB can readily emit partial dislocations to form deformation twin [10, 102, 103]. But, the existence of partials on every slip plane in the GB to grow a single twin is not possible both statistically and practically. Zhu et al. [100] proposed a dislocation reaction and cross-slip mechanisms to emit partials on successive slip plane at GBs to form deformation twins.

When the emitted partials have the same Burger vector (b), the formation of a deformation twin can introduce huge macroscopic strain (nb). However, the different

Burger vector of emission partials can lower the macroscopic strain generated by the deformation twinning. In this section, the formation mechanism of a deformation twin with zero macroscopic strain is presented.

Figure 1.16 shows typical TEM micrographs of deformation twins in nc Al, Ni, and Cu processed by severe plastic deformation techniques. As indicated in white dash line, the GB segments sustain their original smooth shape without visible kink and distortion when intersected with TBs. Zhu et al. [104] postulated a partial emission sequence with zero sum Burger vector for the deformation twin named random activation of partials (RAP). It is hard to drive three different Burger vectors partials by global shear stress simultaneously. One possible argument is that the individual partials are triggered randomly due to the local shear stresses one at a time, since the local shear stress in nc could significantly diverge from the global shear stress. Moreover, the local stress state can easily alter by the GB activity like sliding and rotation [12, 105]. The zero strain deformation twin can raise another question: how can the global strain be conducted to relieve the global stress? First, the zero strain twins do contribute to the global strain due to GB sliding and rotation. Second, the twinning process can dissipate the applied stress and accumulate energy effectively. Although the zero strain twin has no direct contribution to the macroscopic deformation, they can favorably reorient the crystal orientation to contribute to the bulk deformation.

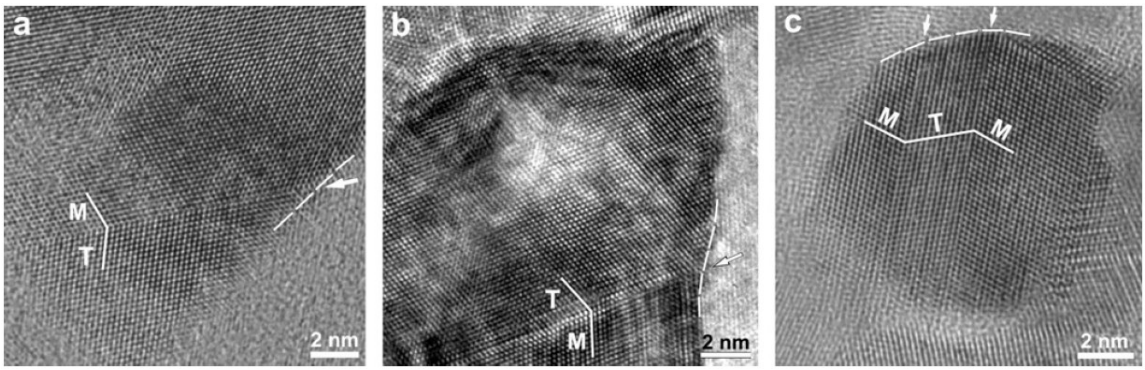

Figure 1.16. High-resolution TEM micrographs of deformation twin with zero macroscopic strain in (a) cry-milling Al, (b) electrodeposition Ni, and (c) high-pressure torsion Cu [104].

The forth deformation twin formation mechanism is the GB splitting and migration. Ashby and Harper first postulated this type of deformation twin in 1967 [106]. And the mechanism is confirmed by MD [95] and experimental observation [107]. The GB segment needs to split and then migrate to form a twin and a new GB segment.

Recently, multifold deformation twins have been observed experimentally [108-110]. The sequential twinning mechanism was postulated by Zhu et al. [110] to explain the formation process of the multifold twin structures. To form the multifold deformation twin, a regular twofold twin needs to form first as the precursor (figure 17a). Then, upper crystal emits successive partials that have b1 Burgers vector to form twin domain III, which converts a twofold twin to a threefold twin structure (Figure 1.17b). The coherent TB is TB2, and incoherent TB is TB3. And a fourfold twin can be formed by partials slip in threefold twin (Figure 1.17c). There is another possibility that the b3 and b4 partials slip simultaneously in threefold twin and form the fivefold twin directly (Figure 1.17d).

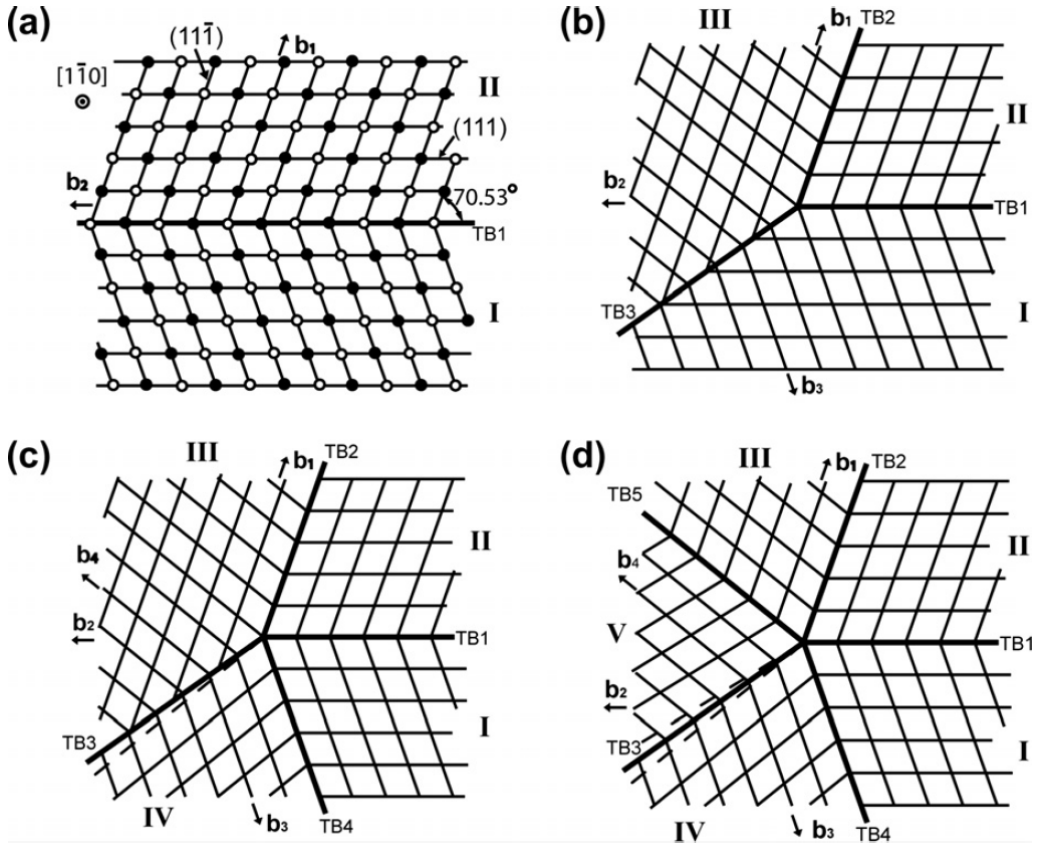

Figure 1.17 The schematics to show the formation of multifold twin structure based on a regular twofold twin structure [99].

I.2.2 Formation mechanism of incoherent twin boundary

The Σ3 {112} incoherent twin boundary is described as three {111}<112> partial dislocations with different Burgers vectors of type a/6<211> periodically occurring on successive {111} planes. The sum of their Burgers vectors is equal to 0.

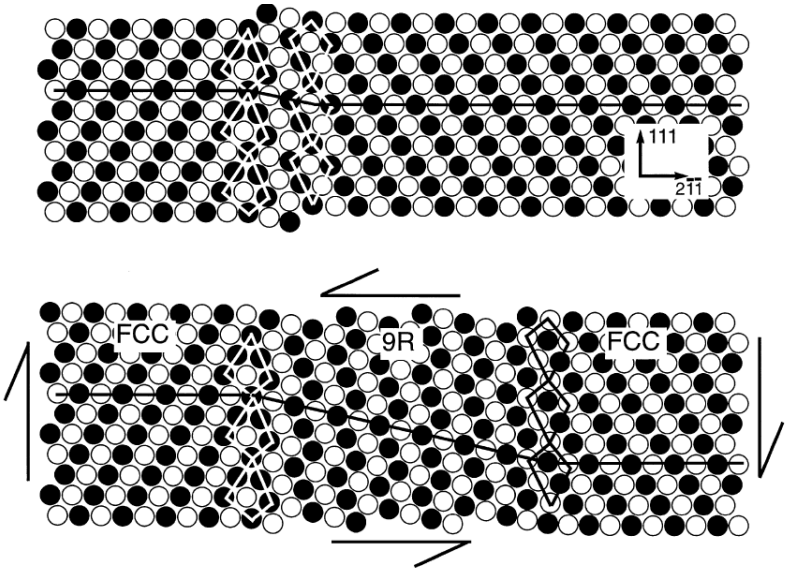

Figure 1.18 An atomistic model of the Σ=3{112} interface in copper. The simulation shows the increase in 9R width predicted upon application of a shear strain parallel with the interface [111].

The dissociation of ITB can result in a narrow, several nanometer wide slabs of 9R phase. The stacking sequence of 9R phase can be described as a close-packed stacking of fcc {111} planes with inserted intrinsic stacking fault in every three atomic layers. Observation of the ITB dissociation have been made in gold [112], silver [113, 114], and copper [115, 116]. The dissociation width of ITB is determined by SFE and local stress. Figure 18 shows the atomistic model of ITB dissociation [116]. There are two formation mechanisms of ITB in fcc metals. One is the tilt GB formation due to the crystal orientation difference at bicrystal interface. Another is the deformation twinning via the consecutive slip of Shockley partials.

I.2.2.1 The incoherent twin formation mechanisms via growth

The Σ3 {112} boundary is one kind of <110> symmetric tilt grain boundary structure. Rittner [117] simulated 21 <110> symmetric tilt grain boundaries (GBs) using an embedded-atom method potential. According to the calculation, the different tilt angle between two crystals results in 21 different boundary planes. When the tilt angle is about 70°, the Σ3 {112} boundary will form to lower the GB energy. The Σ3 {112} boundary dissociation mechanism (9R) involves the creation of SFs, Rittner [118] suggested that it only occurs in low SFE metals. Experimentally, Au shows the GB dissociation [119], whereas there is no GB dissociation in Al Σ3 {112} boundary [113]. Bufford [120] fabricated highly twinned epitaxial Al/Ag multilayer film using magnetron sputtering. As figure 1.19 shows, the domain boundaries are the Σ3 {112} ITBs. The formation of this ITB may be because of the different columns crystal orientations during growth process. When crystal orientation of two adjacent columns has a 60° difference, the boundary column prefer to form Σ3 {112} to decrease the potential energy of the film. Wolf [121] also showed the structure energy correlation for symmetrical tilt GBs in Figure 1.20.

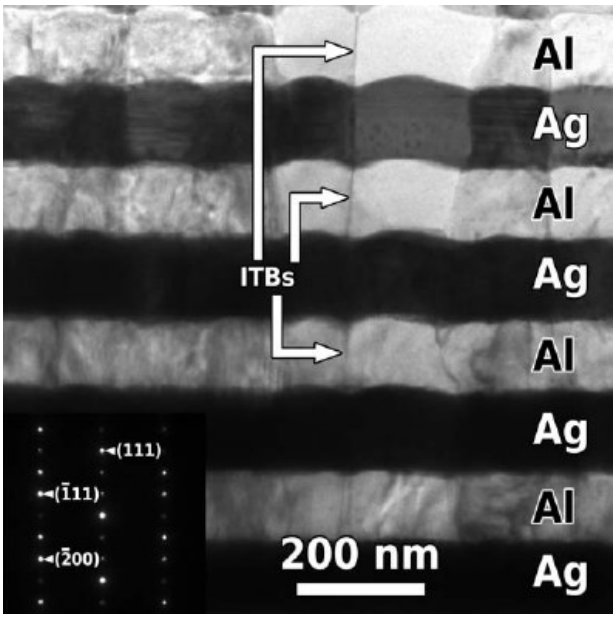

Figure 1.19 Cross-section TEM micrograph of the Ag 100nm/ Al 100nm epitaxial multilayer film from Si <011> zone axis [120].

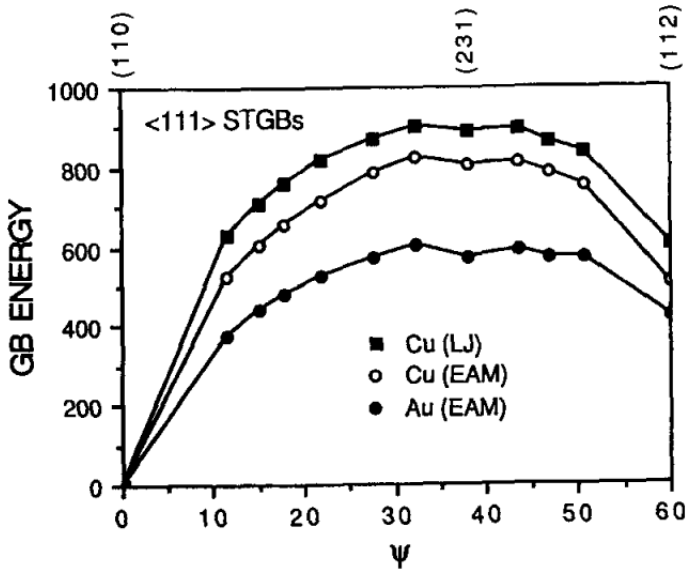

Figure 1.20 Energy for symmetrical tilt grain boundaries on planes normal to <111> [121].

I.2.2.2 The formation mechanism of deformation incoherent twin boundary

Liu [122] reported the observation of zero-strain deformation twin in Ag. The movement of Σ3 {112} ITB facilitated the growth of CTB perpendicular to the ITB. They postulated a hypotheses that the GB, which is close to Σ3 {112} dissociated into one ITB and the other GB to explain the nucleation of deformation ITB based on the experimental observation. Ma [123] suggested that under externally applied stress, the cooperative slip of three Shockley partials produced the zero-strain ITB. Figure 1.7 shows the ITB dissociation under external stress. At stage A, GBs nucleate a twin, and a temporary near-equilibrium ITB is generated at the twin front. They claimed that GB dissociations result in the formation of ITBs and the cooperative slip of Shockley particles inside the ITB induced the formation of CTB along the slip plane of Shockley particles.

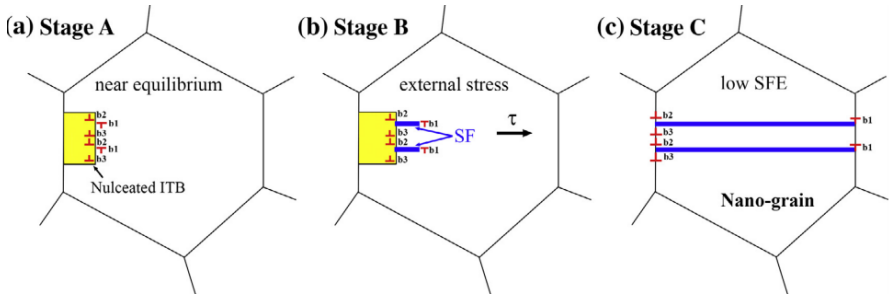

Figure 1.21. Schematic illustration of breakdown process of Σ3 {112} ITB in low SFE F.C.C. alloy [123].

The previous observations indicated that the formation of deformation ITB needs the dissociation of GBs that have similar crystal orientation to the Σ3 {112} boundary.

Under externally applied stress, the pre-existing partials inside the GBs slipped along (111) planes and formed the ITB and CTB spontaneously.

I.3 Mechanical properties of twinned metals

There are various ways to strengthen the materials like GB strengthening, solid solution strengthening, second phase strengthening, strain hardening, and martensite strengthening. In the following section, several TB strengthening mechanisms will be discussed.

In general, when a dislocation interacts with CTBs, it may either: (1) cut through the TB; (2) dissociate into partials and slip along TBs. However, there are many factors that may alter the TB and dislocation interaction processes. To discuss the TB strengthening effect, we will focus on several key factors, including SFE, plastic anisotropy, and morphology of twins.

In the previous section, we discussed the influence of SFE on the formation of a twin. It raises another question: how does SFE impact the interaction between the dislocation and TBs? In this section, we will start with the monoclinic FCC metals with different SFE and divert to the alloys to discuss why the SFE can control the interaction process.

When a screw dislocation interacts with the CTB, it will be redirected into the TB and split into two partials which move along the TB in the opposite direction for Al with high SFE [67]. For the Cu and Ni with lower SFE, the primary interaction mode is the direct cutting through CTB mechanism without any slip in the TB plane. The screw dislocation interaction with TB in Al happens spontaneously once the dislocation

approaches the CTB, whereas the cutting-through mechanism needs applied stress to initiate for Cu and Ni. At even more complicated situation involving the interaction between non-screw dislocations and CTBs, the dislocation in Al still prefers to slip along the CTB. But, when the applied stress is high, the dislocation can also cut through the CTB [124]. The dislocation activity in Ni is similar to that in Al.

However, partials in Cu are prone to slip along twin plane rather than TBs due to its low SFE. To rationalize the dislocation activity in monoclinic fcc metals for both screw or non-screw dislocations, a parameter is introduced in equation 13 to qualify the lattice resistance for the partial re-nucleation along glide planes or the TBs. The higher the R or R', the larger the resistance. Based on the calculated fault energy that the authors provided [124], the negative R' in Al suggests that the dominant role of relaxations when the dislocations arrive at the CTB. However, based on the calculated fault energy from others papers [91, 92, 125], the unstable TB energy should be larger than the SFE. This discrepancy for Al needs more evidence to verify especially from direct observation of the interaction between the TB and dislocations.

$$R = \frac{\gamma_{us}-\gamma_s}{\mu b_s}\ (normal\ glide\ plane), \quad R' = \frac{\gamma_{ut}-\gamma_s}{\mu b_s}\ (TB) \quad \text{Equation 13}$$

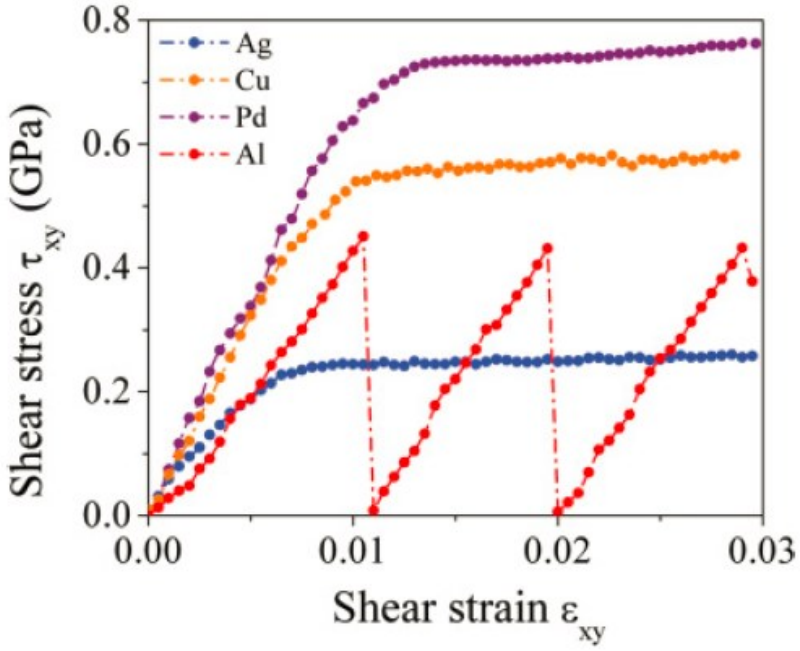

Figure 1.22 The strain-stress curve of ITB in Ag, Cu, Pd and Al [49].

In addition to CTBs, an ITB also can act as a strong barrier for the transmission of dislocations. Since the ITB consists of arrays of partial dislocations, the response of pre-existing partials under the shear stress varies for the metals with different SFE. As shown in figure 1.22 [49], one type (type 1) shear stress in Ag, Cu, and Pd increases gradually followed by a plateau, whereas Al (type 2) contains periodic load drop with linearly stress increment. For the type 1, the applied stress can dissociate the ITB to the 9R phase. In contrast, the ITB will move vertically to the slip plane of the partials to create steps between the matrix and twin structure.

Since the SFE plays an important role in the interaction of dislocation with TBs, there are increasing studies on tailoring the mechanical properties of twinned metals by

changing the SFE. Zhu et al. [126] observed high ductility and high strength Cu by alloying with 10 wt.% Zn (Figure 1.23). Due to low SFE in CuZn, high-density twin and stacking fault can form after the high-pressure torsion. More deformation twins can be triggered during the tensile test to block the dislocation activity resulting in the high strain hardening rate. Thus, the ductility has increased. High strength has been ascribed to the high-density twin, solid solution hardening, and the smaller grain size.

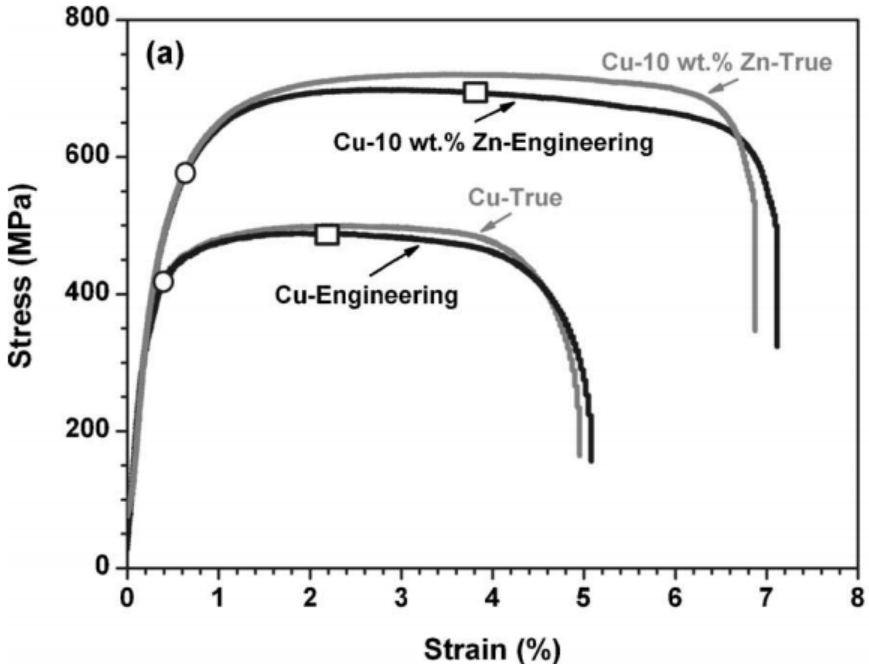

Figure 1.23 The tensile engineering and true strain-stress curve for Cu and Cu-10wt%Zn [126].

However, the addition of Zn in the Cu leads to significant solid solution hardening, making it difficult to isolate the contribution from the lower SFE. In another system, NiCo alloy, the influence of Co solid solution strengthening is insignificant due to the similar

atomic diameters of Ni and Co. Sun et al. found a higher strength and better ductility of NiCo alloy by adding more Co (as Co decreases the SFE of Ni) [127].

I.4 Thin film deposition technique and growth mechanisms

There are various techniques to fabricate thin films. In general, all methods can be divided into a solution-based deposition and vapor deposition, which represents the liquid-to-solid or vapor-to-solid phase transformations. Under the category of vapor deposition, there is physical vapor deposition (PVD) and chemical vapor deposition (CVD). PVD includes a broad range of vapor-phase deposition technologies. During PVD process, the solid materials are physically ejected in the form of atoms, molecules, and clusters. Then, all these vapors condense on a surface. During the condensation, nucleation of solid phase occurs, followed by the growth of solid phase. Different form the PVD, CVD uses chemical reactions on surfaces to despite the film. In this section, we will focus on the PVD and the corresponding film growth mechanisms.

I.4.1 Physical vapor deposition

Different methods are used to vaporize solid materials in PVD techniques. One way to vaporize materials is thermal evaporation, which often melts the target at a high temperature to generate a vapor of atoms. Another technique is the magnetron sputtering. Ionized inert gasses bombard the target surface, the ejected atoms and molecules form a continuous stream of plasma that carry the atoms/molecules towards substrate surface. Reactive gasses, such as nitrogen, can be used to fabricate nitride films.

Thermal evaporated has atoms have low kinetic energy. In contrast, magnetron sputtering can introduce high kinetic energy into vaporized atoms or clusters, which leads to dense films.

I.4.2 Film growth

The properties of thin films fabricated by PVD are controlled by the film growth process, which can be tuned by the following key factors: (1) the morphology, chemistry, and the stability of the surface; (2) the deposition process and the configurations of system- e.g. the incidence angle, the deposition flux, the temperature of deposition, gaseous contamination, the kinetic energy of the ionic atoms; (3) film growth process – e.g. the mobility of the incoming adatoms on the surface, nucleation, the formation of interface, growth morphology of the film, the stress evolution, the formation of defects and interface; (4) post-deposition processing- e.g. thermal treatment, deformation, surface corrosion. To achieve consistent film structure, all the factors must be controlled. In this section, we will focus on the film growth process related to the adatoms nucleation, growth, and structure evolution.

I.4.2.1 The nucleation modes

During condensation, atoms lose their energy by bonding to other atoms, which can be the atoms of the substrate or the other incoming atoms. The surface mobility correlates closely with the bonding energy, which can be measured by thermal desorption techniques. If there is a week interaction between the adatoms and surface, the adatoms have high surface mobility and may be trapped by preferential nucleation sites where strong bonding arises from a change in chemistry or the coordination number increment.

According to the nature of the interaction, three nucleation mechanisms have been identified: (1) the Frank-van der Merwe mode, which is the layer-by-layer growth mode due to the growth of the low surface energy films on the high surface energy substrates; (2) the Volmer-Weber mode, which is in form of island growth resulting from interaction between high surface energy films and low surface energy substrates; and (3) Stranski-Krastanov mode represents the combination of layer growth and island growth due to the similar surface energy of films and substrates.

I.4.2.2 Microstructure evolution of during growth of films

The growth process includes the nucleation, island or layer growth, the coalescence of the island due to their impingement, the formation of a continuous structure, the steady-state film growth. After nucleation, the island coalescence will trigger by the surface energy minimization. Thus, the islands with low surface energy will grow by consuming the high surface energy islands through the diffusion process. Due to the preferential growth during the island coalescence, a film may form preferred orientation with low surface energy crystal planes. Secondary nucleation also happens due to the new open substrate area resulted from the rapid coalescence. Coarsening processes are controlled both by temperature and island size. For a larger island, especially at low temperature, a slow coarsening process is controlled by GB migration, which will stop until the grain size is sufficiently large. Then the film forms a continuous structure and steps into the steady-state growth region. To characterize the film structure evolution at different deposition temperature, three different regions have been identified [128]. At low deposition

temperature, a film forms an dense structure with a fiber texture due to the negligible adatom diffusion process. The columns sustain random orientation of the nuclei due to the poor adatom mobility. The columns contain small equiaxed grains or completely amorphous. At higher deposition temperature, the surface diffusion of adatom is obvious, causing local epitaxial growth with pronounced columnar structure. During the grain growth process, the competition between differently orientated grains is the primary feature which has been illustrated by Gimer et al. [129] for Aluminum growth. At even higher deposition temperature, due to severe bulk diffusion, GB migration will not stop after the island coalescence. Low surface energy grain will grow at the expense of the grain with unfavorable orientation.

I.4.3 Epitaxial growth

Epitaxy means the deposited crystalline layer mimics the surface lattice structure of the substrate. Homoepitaxy refers to the case where the film and substrate are of the same material, and is widely used in the semiconductor industry to deposit Si films on the Si substrates. In contrast, heteroepitaxy refers to the case where epitaxial film has different chemical composition and/or crystal structure with the substrate. As figure 1.24 shown, the TaN/TiN thin film grows epitaxially on Si(100) substrate [130]. First, TiN grows on the Si substrate epitaxially accommodated by arrays of misfit dislocations arranged at the interface (Figure 1.24(c)). Subsequently a TaN layer is deposited on top of TiN. Heteroepitaxial growth has the advantages on electrical, mechanical, and optoelectronic

performance due to the improved texture of films with less detrimental GBs that deflect electrons.

To characterize mismatch between the film and substrate interface in the heteroepitaxial system, the mismatch strain f is defined in equation 14, where a_s is the substrate lattice parameter and a_f is the film lattice parameter. During the film growth, when the film is thin, the mismatch strain can be accommodated by the coherency strain. With the increase of film thickness, the strain energy builds up simultaneously and exceeds the maximum strain that coherent interface can sustain. Then a misfit dislocation forms to release to the misfit strain [131, 132].

$$f = \frac{a_s - a_f}{0.5(a_s + a_f)} \qquad \text{Equation 14}$$

So, the total elastic energy due to the misfit strain between the film and substrate can be expressed by the combination of coherency strain energy and the energy of a misfit dislocation. The equation 15 shows the relationship between total elastic energy and coherency strain and misfit dislocation energy.

$$E_{tot} = \varepsilon_c^2 Bh + \frac{\mu_f b}{2\pi(1-v)}(f - \varepsilon_c)\left[\ln\left(\frac{h}{b}\right) + 1\right] \qquad \text{Equation 15}$$

Where ε_c is the coherency strain. B is biaxial modulus. Using equation 15, the critical layer thickness to form the misfit dislocation can be calculated when $\frac{dE_{tot}}{d\varepsilon_c} = 0$.

Besides the misfit dislocations, misfit twins can also form to release the elastic strain generated by the misfit strain between the film and substrate in Si/Ge, Ga/As and Pd/Ni systems [133-135]. Instead of forming perfect dislocations, twinning partial dislocations can form at the interface as the precursor of twin nucleus.

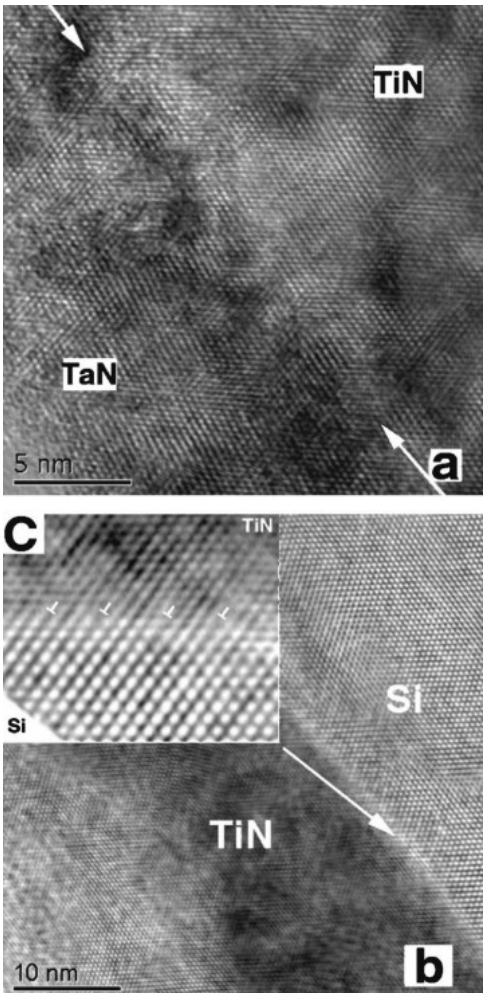

Figure 1.24 High-resolution TEM micrographs of TaN/TiN/Si(100) film. (a) the interface of TaN/TiN; (b) the interface of TiN/Si; (c) the enlarged micrograph of the interface between Si and TiN with the misfit dislocations [130].

I.5 Scope and goals

The motivation of this thesis includes several aspects related to the growth twin formation in fcc metals with high SFE, the alloying effect on the twin formation of Al-based materials, and the mechanical properties of the thin film with the different type of twins. We first discuss the synthesis of twinned Al film. The growth twin formation mechanism will be discussed. Then epitaxial nt Al films with different orientation will be synthesized, and the influence of the film growth orientation on twin formation will be studied. We apply the co-sputtering technique to deposit the Al-based alloy films with high-density growth twins. The doping effect on film microstructure evolution and twin formation ability will be studied.

Beside the microstructure analysis, the mechanical properties of twinned Al film and co-sputtered Al alloy will be examined by nanoindentation and *in-situ* pillar compression. Various factors (twin orientation, twin fraction, and domain size) that affect the strength and ductility of twinned films will be discussed. Al films are employed in numerous applications, such as movable parts in MEMS devices, as a metallization material for integrated circuits and flat panel LCD monitors. Therefore, Al with high strength from high-density twins is highly desirable.

CHAPTER II

EXPERIMENTAL

II.1 Magnetron sputtering

All the thin films were deposited using the magnetron sputtering with four 3'' circular sputtering source (TORUS® Kurt J. Lesker Company, Livermore, CA) system as shown in figure 2.1. The MDX1.5 KW power supply has been used for the sputtering. The high vacuum chamber is pumped by turbomolecular drag pump (Pfeiffer Vacuum Gmbh, Berliner, Germany) and cryopumps (cryo-torr cryopump, Trillium US Inc.).

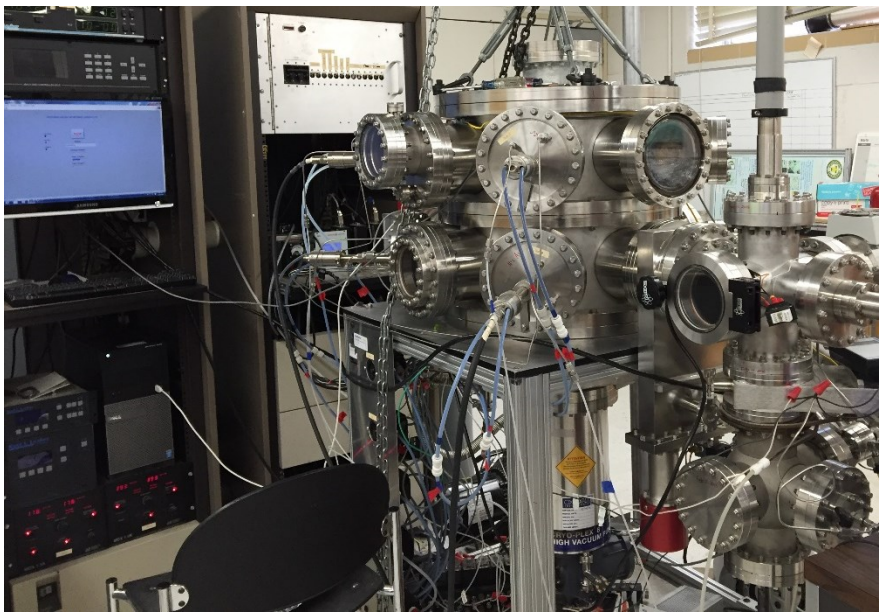

Figure 2.1 The set-up for custom-built magnetron sputtering system.

The base pressure of the chamber is 3-8×10^{-8} torr before the deposition. Ultra-high purity Ar gas was used as the source to generate the plasma during the deposition. The

single crystal silicon substrates (Desert Silicon LLC) were used as the substrates in all deposition experiments. All the metal targets (Al, Ag, and Mg) have high purity (99.99%) with 3'' diameter. Silicon wafers with different orientations were etched by HF to remove native oxide before deposition. The primary parameter of the deposition is the deposition rate which was controlled by the deposition power. The higher the deposition power, the greater the deposition rate.

The simplified sputtering process is described below. First, the inert Ar gas flows into the sputter gun. The Ar atoms are ionized due to the applied DC voltage between the cathodes and anode. The Ar ions and electrons form the plasma which is confined by the magnetic field. Inside the magnetic field, the charged and energetic Ar ions accelerate towards the target and strip off the atoms from the target surface. These ejected atoms or atom clusters fly towards the substrates and form the film on the substrates.

II.2 X-ray diffraction (XRD)

XRD is used to identify the phase, crystal structure, chemical bonds, and even the disorder of the materials. The monochromatic beam of x-rays is directed onto the thin film sample, based on the Bragg's law; the crystal lattice can diffract the beam following the equation 16. Where λ is the incident x-ray wavelength, θ is the angle between the incident beam and the crystal plane which interact with the x-ray beam, d is the interplanar spacing and n is the order of diffraction.

$$n\lambda = 2dsin\theta \qquad \text{Equation 16}$$

The twin structure also can be detected by the XRD using the phi scan due to the symmetrical rotation between the twin crystal and matrix. Figure 2.2 shows [120] the phi

scan for {111} planes in different films. The [111] is a rotation axis with three-fold symmetry. Thus, the phi-scan ([111] rotation axis) for {111} planes shows three peaks in single crystal-like structure. Whereas, the twinned crystal double the number of {111} peak, as shown in Ag/Al films (second and third rows in figure 2.2).

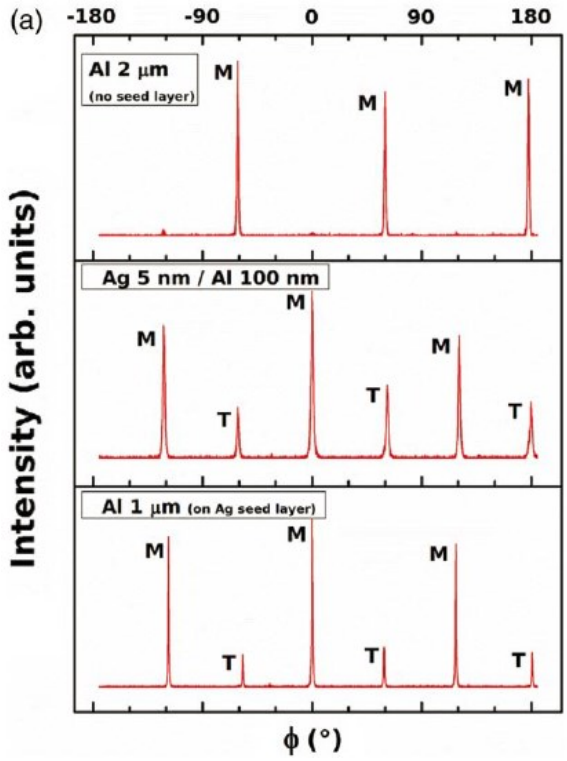

Figure 2.2 The X-ray diffraction of {111} phi-scan profiles of different films. M represents the matrix and T means the twin crystal [120].

Conventional 2θ scans were used to characterize the phase in thin films which were performed at PANalytical (Almelo, Netherlands) X'Pert PRO materials research diffractometer using Cu Kα radiation (λ= 1.5418 angstron).

II.3 Transmission electron microscopy (TEM)

TEM is a important tool to analyze the microstructure and chemical information, crystallographic details of the film on a fine scale. The resolution of the microscope is controlled by the wavelength of the incident source. For the optical microscopes, the wavelength is around the several hundred nanometers. In the case of the 200kV TEM microscope, the wavelength is 2.75 pm. However, the resolution in TEM is also restricted by the accumulated aberrations which are caused by the lenses in the TEM.

There are four major components in a TEM, which are the illumination system, electromagnetic lens, the sample holder, and the signal captured system. First, the illumination system provides the high energy electron beam. Usually, the electrons are emitted by heated tungsten or LaB_6 and confined into a roughly focused beam. To form monochromatic electrons, the beam passes through a small hole at the center of the anode which can also accelerate the passing beam. After electrons going through the hole in the center of the anode, the beam is focused and confined by a series of condenser lenses and apertures to form a coherent electron beam. Then, the beam hits and transmits the specimen and all the signals generated during the interaction between the sample, and the electron beam is captured by various detectors in TEM.

Bright field (BF) is the normal imaging technique. The contrast of the image comes from the intensity difference of different features which deflect the electron beam diversely. Dark filed imaging is an inverse of the bright field. Additionally, by controlling the beam and applied various detectors to collect different information. By scanning the

beam on a specimen and collecting the scattered electrons (also called high angle annular dark field scanning TEM), the micrograph can show the contrast based on the compositional difference. Normally, chemical analysis technique, like energy dispersive X-ray (EDX) spectroscopy and electron energy loss spectroscopy (EELS) is coupled with scanning TEM (STEM).

TEM and STEM were conducted by using an FEI Tecnai G2 F20 ST microscope equipped with a field emission Gun operated at 200 kV at Microscopy and Imaging Center.

II.4 Nanoindentation

The hardness of the materials can reflect the resistance of the material to the localized plastic deformation. Normally, the hardness of indentation is three times larger than the flow stress of materials. Since the thin films have a small volume that is insufficient for tensile test, the nanoindentation shows the superiority to probe the mechanical property in a small volume. Two steps are involved in the nanoindentation measurement. First, a diamond indenter is compressed into the materials using a pre-set load or displacement. Then, the indenter is retracted from the sample. During the retraction, the elastic deformation recovers while the plastic deformation can not recover and leave a residual indent on the surface. The indentation hardness is calculated by equation 17. Where P_{max} is the peak load, and A_C is the projected contact area.

$$H_{IT} = P_{max}/A_C \qquad \text{Equation 17}$$

A_C is calculated based on a mathematic area function which correlates with indentation depth h_C. Although the hardness calculation is obtained from the

nanoindentation load-displacement curve, it is still sensitive to different analysis methods like elastic contact model [136] and continuous stiffness method [137]. The elastic contact model is most commonly accepted method which contains three essential assumptions. First, it is a pure elastic deformation during the unloading process. Second, it can be combined with springs in series for the compliances of the specimens and indenter. Third, the contact between an indenter and the specimen can be modeled for the contact between a sphere and an isotropic elastic half-space using the equation 18. Where S is the contact stiffness which is the slope of unloading curve, and E_r is the reduced modulus.

$$\mathrm{s} = \frac{2E_r\sqrt{A_C}}{\sqrt{\pi}} \qquad \text{Equation 18}$$

The contact depth h_C can be calculated by the equation 19 found on these three assumptions. To illustrate the different indentation depth, figure 2.3 shows the schematic of a cross-section view of indentation area and the load-displacement curve for the indentation [138, 139]. Where h_{max} is maximum penetration depth, h_c is the contact depth, h_i is the intercept depth, and h_f is the depth after the unloading.

$$h_c = h_{max} - \varepsilon(h_{max} - h_i) \qquad \text{Equation 19}$$

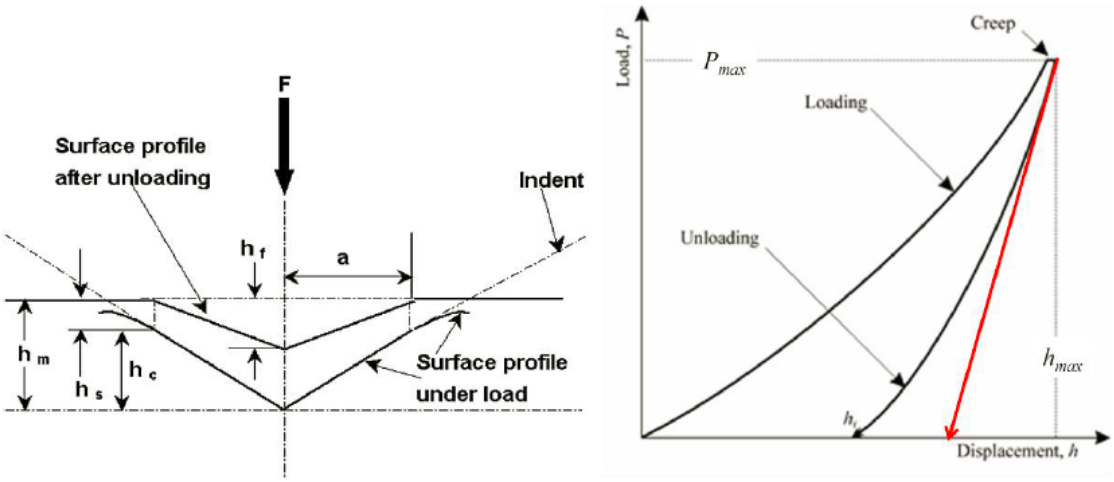

Figure 2.3 The cross-section of contact area for the indentation, the loading/ unloading curve [138, 139].

The reduced Young's modulus (E_r) can be expressed by the equation 20. Where the E_i is the indenter Young's modulus, and v_i is the Poisson's ratio of indenter, which is 1140 GPa. E and v are the specimen's Young's modulus and Poisson's ratio, respectively. Thus, to obtain the Young's modulus and the hardness of the test specimen, first, the contact stiffness and contact depth can be calculated based on the equation 19. Then, according to the mathematic relationship, the contact area can be calculated. The hardness is the result of maximum load divided by the contact area. The reduced Young's modulus then can be calculated by using equation 18. It is easy to get the Young's modulus of specimen from equation 20.

$$\frac{1}{E_r} = \left(\frac{1-v_i^2}{E_i}\right) + \left(\frac{1-v^2}{E}\right) \qquad \text{Equation 20}$$

II.5 Electron backscatter diffraction (EBSD) and Transmission kikuchi diffraction (TKD)

EBSD is a crystallographic technique that can provide the information of grain orientations, the texture of the materials, point-to-point orientation relationship and phases on the surfaces of materials. This technique has been widely used in metallurgical and materials fields due to multiple advantages, including the simple sample preparation procedure, the complementary information of the microstructure, and the high acquisition speed. In 1928, Nishikawa and Kikuchi observed a diffraction pattern from backscattering mode and transmission mode [140], which shed light on the identification of crystal structure by using the Kikuchi pattern. The EBSD set-up normally is equipped with a scanning electron microscope (SEM) as the source of the electrons. To acquire the backscatter diffraction signal, the sample is placed in the SEM chamber inclined to the incident electron beam with 30 degrees. And the phosphor screen is faced to the sample surface to detect the backscatter signal from a volume of the material, typically 20 nm deep from surface. Among all the backscatter signals, only the electrons diffracted based on the Bragg' law can generate the Kikuchi pattern that can be captured by the camera screen.

Normally, the minimum spatial resolution of EBSD is around 50 nm [141], which is caused by two reasons. First, the long working distance is a need for the sample to fulfill the geometry limitation regarding the SEM pole piece and the EBSD detector due to the large tilting angle of the sample. Second, high sample tilting also causes the enlarged interaction volume which also reduces the resolution. To improve the spatial resolution,

an alternative method which is called TKD has been used in the EBSD data acquisition. For the TKD, the sample must thin enough to transmit the electron beam. In this scenario, the diffraction happens on the lower surface of the thin sample when the electron beam passes the sample. Thus, it is possible to decrease the working distance based on the TKD set-up which is shown in figure 2.4 [142]. Due to the geometry, the specimen tilting angle is not required to title more than 10 degrees, which will avoid the enlarged interaction volume.

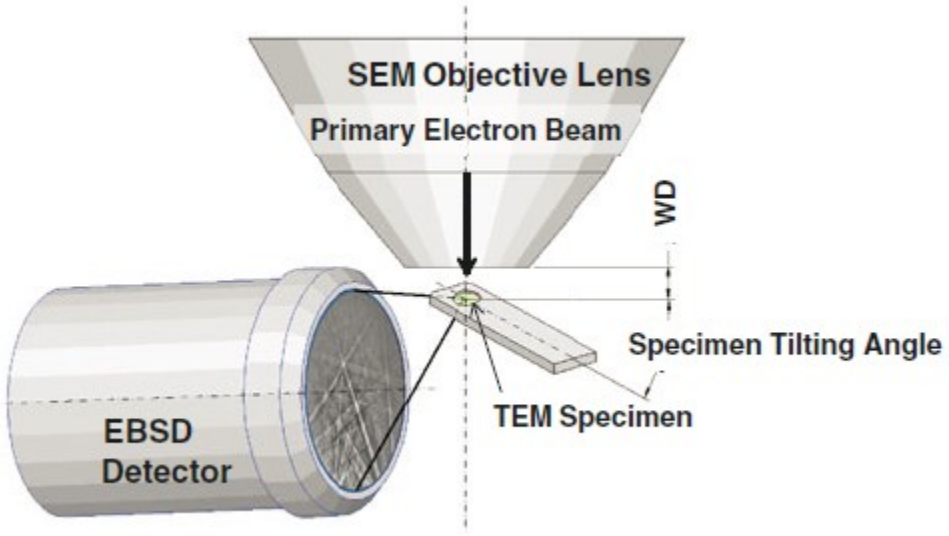

Figure 2.4 The schematic of the geometry for transmission Kikuchi diffraction set-up[142].

There are several parameters need to be tuned carefully to acquire a high-quality EBSD data regarding the high hit rate and low mean angular deviation, The working distance is the most important one among all the parameters, which also correlates with

the tilting angle of the specimen. As shown in figure 2.5 [142], the small tilting angle and the short working distance can enhance the quality of the Kikuchi pattern. Another factor is the acceleration voltage of the electron beam, to achieve the best condition, the proper voltage needs to be found. If the voltage is low, it is sensitive to the very thin area but not enough signal for the thicker area. The acceleration voltage which the electron beam is applied should tune based on the sample thickness.

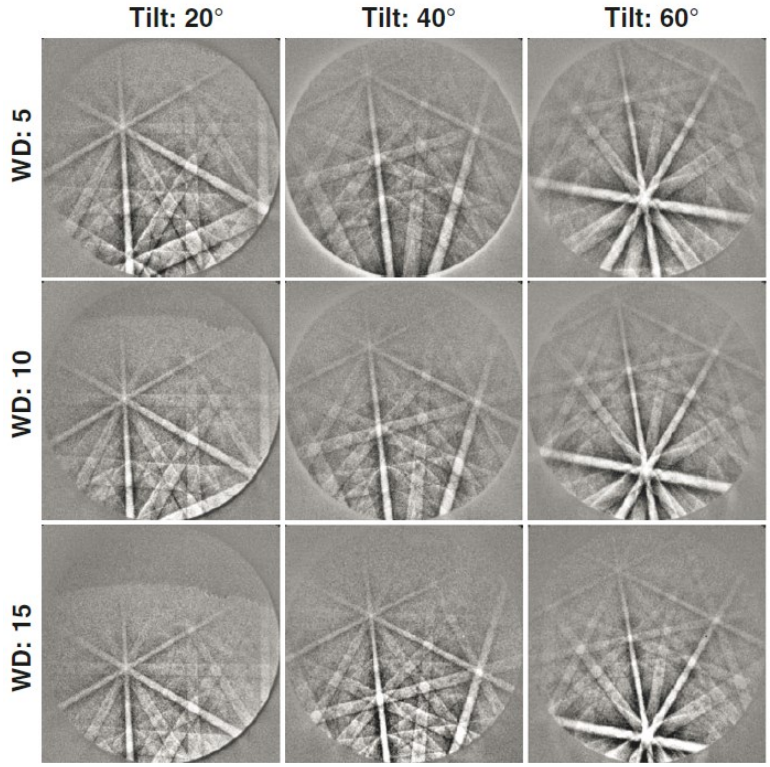

Figure 2.5 The Kikuchi pattern of Al thin film at a different working distance and tilting angle worked at 25 KV [142].

As figure 2.6 shows [143], it is obvious that good diffraction patterns can be captured from the specimen with the thickness between 70 nm and 400 nm using 22kV

acceleration voltage. But, compared with the thinner area (<100 nm), thicker area are more likely to generate overlapping patterns due to the tiny grain size and inclined GBs. So, the optimum range for good quality pattern is from 70 nm to 200 nm.

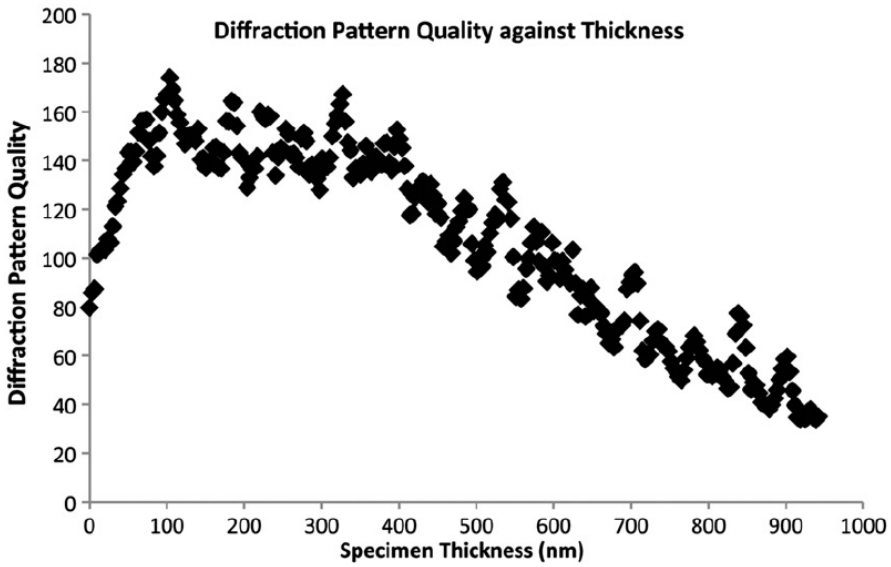

Figure 2.6 The profile of the pattern quality change as a function of specimen thickness [143].

Based on the pioneering work from Trimby [144], Suzuki [142] and, Patrick[143], the parameters used in this experiment for Al thin film are listed below. The specimens were mounted in the Oxford TKD sample holder, which clamped the TEM specimens at 20° tilting angles based on the horizontal plane of the sample holder. Then, the sample holder was mounted on the stage of Tescan FERA-3 with Schottky field emission electron source operated at 28 kV. There is no tilting on the SEM sample stage. Thus, the angle between the electron beam and the sample surface is 70°. The sample working distance is

5.5 mm to make sure the sample is above the level of the top of EBSD detector (Oxford NordlysNano high sensitivity camera). The beam spot size is 12nm and absorption current is around 1nA. These above are the settings for the SEM.

To acquire the high-quality Kikuchi diffraction patterns using Aztec 2.0 software, the following parameters are important. Optimized-TKD indexing mode can provide more accurate result compared with conventional band detection mode. The diffraction patterns were collected under 336 × 256 pixels image resolution, and the scan step size is 18nm. Indexing rates varied with the sample condition and film thickness and the range are between 70% and 95%. The TKD data were processed by Oxford CHANNEL software. The typical scan area in this experiment using TKD-EBSD is 5 × 3 micron.

CHAPTER III

THE FORMATION MECHANISMS OF GROWTH TWINS IN POLYCRYSTALLINE ALUMINUM WITH HIGH STACKING FAULT ENERGY*

III.1 Overview

Growth twins are scarcely observed in metals with high stacking fault energy, such as pure Al. In this study, however, we report the observation of growth twins in sputtered polycrystalline Al films on amorphous substrates and a majority of these growth twins are inclined to the growth direction (inclined twins). Although the fraction of twinned grains is low in general, it increases monotonically with increasing film thickness, reaches a maximum at the film thickness of 80 nm, and decreases gradually thereafter in the thicker films. The nucleation mechanism for the inclined twins is compared with that of the parallel growth twins in Al. Different twin formation mechanisms are discussed. This study provides an alternative perspective to evaluate the formation of growth twins in metals with high stacking fault energy.

---

* This chapter reprinted with permission form "The Formation Mechanisms of Growth Twins in Polycrystalline Aluminum with High Stacking Fault Energy" by S. Xue, Z. Fan, Y. Chen, J. Li, H. Wang, and X. Zhang, 2015. *Acta Materialia*, Volume 101, pp 62-70, Copyright 2015 by Elsevier.

III.2 Introduction

Nanotwinned (nt) metals have been intensely studied and show various unique properties. Cu with nanotwins have excellent electrical conductivity [52, 58] while maintaining high mechanical strength. Nt metals, such as Cu and Ag [59-62], also show better thermal stability than monolithic nanocrystalline (nc) metals [63-65]. The mechanical properties of nt metals have also been extensively studied [52-54, 59, 66-70, 99, 120, 145, 146]. Nanotwins enhance the mechanical properties of metals via various mechanisms, some of which are briefly summarized as follows. First, molecular dynamics (MD) simulations have shown that glide dislocations can be blocked by the $\sum 3\,(111)$ coherent twin boundary (CTB) [54, 67, 124, 147] and Σ3(112) incoherent twin boundary [49, 148, 149]. A very high stress is necessary to transmit dislocations across TBs [150, 151]. *In situ* nanoindentation studies of nt Cu confirm significant interactions between dislocations and CTBs/ITBs [147, 152]. Second, high density dislocations can accumulate at the CTBs and thus enhance work hardening capability and ductility comparing with nc metals [53, 153, 154]. Third, TBs are mobile manifested as detwinning in nt Cu as have been observed experimentally by *ex situ* shear deformation [145, 155-157] or *in situ* nanoindentation and validated by MD simulations [69, 152]. The stress for detwinning of fine nanotwins can be exceptionally low, ~ 100 MPa, much lower than the yield strength of nt Cu [152].

Prior studies on twins focus primarily on metals with low stacking fault energy (SFE), such as Cu, Ag, GaP and 330 stainless steels [19, 53, 66, 90, 120, 122, 145, 158-164]. Because of the appealing mechanical properties induced by TBs, there are increasing

interest in synthesis of twinned light-weight metals, such as Al. Although twins can be introduced into fcc metals by annealing (annealing twins), deformation (deformation twins) and growth (growth twins), the twinnability of fcc metals remains largely controlled by their SFE [19, 99, 100, 125, 158, 165]. Consequently it is much more difficult to introduce twins in high SFE metals than those with low SFE. The prediction of deformation twin in nc Al by molecular dynamics simulation [95, 125] leads to a series of successful discovery that shows twins can indeed be introduced via nanoindentation [166], tensile test [53] or cryomilling [97] in nc Al. These evidence give us a hint that although the Al has an inherently high SFE barrier to form twins, other factors, such as grain size [8, 167], strain rate [168, 169] and high stress concentration [89], may trigger the formation of twins.

Recently high-density growth twins and stacking faults have been fabricated in Al by introducing nt Ag buffer layers [22, 120, 170] by the magnetron sputtering technique. The Al film grown epitaxially on Ag replicates the microstructures including twins from the Ag seed layer because Ag and Al has identical lattice parameter and crystal structure. A systematic study on various metallic multilayers leads to two criteria for the introduction of growth twins into high SFE metals [72]. The first criterion emphasize the need for a low SFE buffer layer that can readily form high-density twinned seeds; and the second criterion highlights the significance of global coherency between coherent similar interface (between constituents with identical planar indices) or local coherency between coherent dissimilar interfaces (between constituents with different planar indices) that allow twins to propagate across layer interfaces. Although high-density growth twins have

been introduced into Al with the assistance of the buffer layers, whether growth twins can be synthesized in Al without low SFE metal buffer layers remains an unanswered question.

In this article, we present a simple method to introduce twins into polycrystalline Al films by DC magnetron sputtering without low SFE metallic seed layer. By controlling the film thickness, the fraction of twinned grains in Al can increase to nearly 10%. We also investigated the inverse film thickness effect on the formation of twins in thicker Al films. The twin formation mechanisms, including nucleation and growth of twins, are discussed.

III.3 Experimental

Polycrystalline Al films were deposited at room temperature by DC magnetron sputtering using 99.99% purity Al target onto Si substrates and sample grids supported with carbon film for transmission electron microscopy (TEM) studies. The aluminum films of different thickness (20-180 nm) were deposited by controlling deposition time under the same deposition rate, 0.7 nm/s. The base pressure of the vacuum system prior to deposition was ~8× 10^{-8} torr or better and Ar gas pressure was ~ 2.5× 10^{-3} torr during magnetron sputtering. TEM studies were performed on an FEI Tecnai F20 ST electron microscope operated at 200 kV and equipped with a Fischione ultra-high resolution high-angle annular dark field (HAADF) detector. For the statistic studies on the distributions of grain size and twin thickness, ~ 500 grains were measured for each specimen with different film thicknesses, and over 1,200 grains were counted for each film to calculate the fraction of twinned grains at different locations in order to establish statistical significance.

III.4 Results

Plan-view TEM micrographs are shown in Fig. 3.1 for polycrystalline Al films with different film thickness (h) deposited on TEM grids. In the 20 nm thick Al films in Fig. 3.1a, growth twins were observed as labeled selectively by arrows. The average grain size (D_{ave}) is 30 nm. The inserted selected area diffraction (SAD) pattern (collected with a large aperture to include numerous grains) shows numerous continuous rings, such as (111), (220) and (200) diffractions, arising from nc grains. When the film thickness (h) increases to 100 nm, the SAD pattern in Fig. 3.1e shows film texture barely changes. Meanwhile the grain size of the Al film increases to over 100 nm when h = 140 nm. Fig.3.2a shows a CTB multi-junction containing two 2-fold twins. The white dash box b in Fig. 3.2a is magnified in the high resolution TEM (HRTEM) micrograph in Fig. 3.2b. Each of the 2-fold twins contains 2 CTBs (CTB1 and 2). The two nodes are connected by a highly distorted boundary that is nearly parallel to the {111} plane. The fast Fourier transform (FFT) of Fig. 3.2b shows the relationship between the two sets of TBs in Fig. 3.2c. The two CTBs in node 1 are identified to be $(1\bar{1}1)$ and $(\bar{1}\bar{1}1)$ plane, respectively. The HRTEM micrograph of the box d (in Fig. 3.2a) shows stacking faults (SF) adjacent to the TB (Fig. 3.2d).

Statistical studies in Fig. 3.3a show that the average grain size (D_{ave}) increases monotonically from 30 to ~110 nm with film thickness when $h \leq 80$ nm; and it then approaches a plateau, ~140 nm, in thicker films. In parallel with the increase of film thickness, the average twin spacing (T_{ave}) also increases, from 12 to 44 nm, when $h \leq 80$ nm; and approaches 57 nm when h = 180 nm. The ratio of T_{ave}/D_{ave} is ~ 40% with little

dependence on film thickness. Fig. 3.4 summarizes the evolution of T_{ave} and D_{ave} with film thickness. Meanwhile the fraction of twinned grains rises monotonically and reaches a maximum of 9.5% when h = 80 nm, which is twice as much as the fraction of twinned grains in the 20 nm-thick films. The fraction of twinned grains then decreases thereafter in the thicker films.

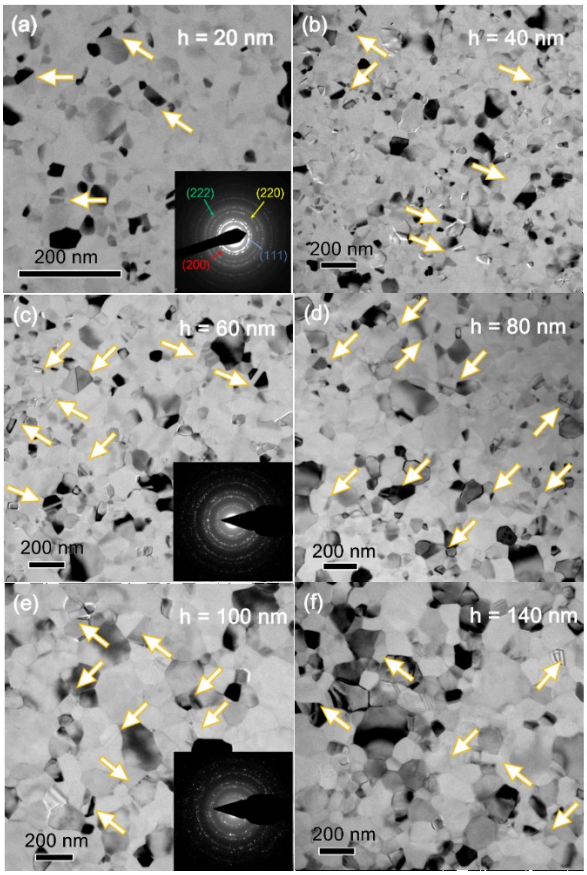

Figure 3.1 Transmission electron microscopy (TEM) micrographs of Al films with different film thickness showing the formation of growth twins. (a) h = 20 nm, (b) h = 40 nm, (c) h = 60 nm, (d) h = 80 nm, (e) h = 100 nm, (f) h = 140 nm. Twins were frequently observed as labeled selectively by arrows in the micrographs. The inserted selected area diffraction (SAD) patterns indicate the formation of polycrystalline Al films.

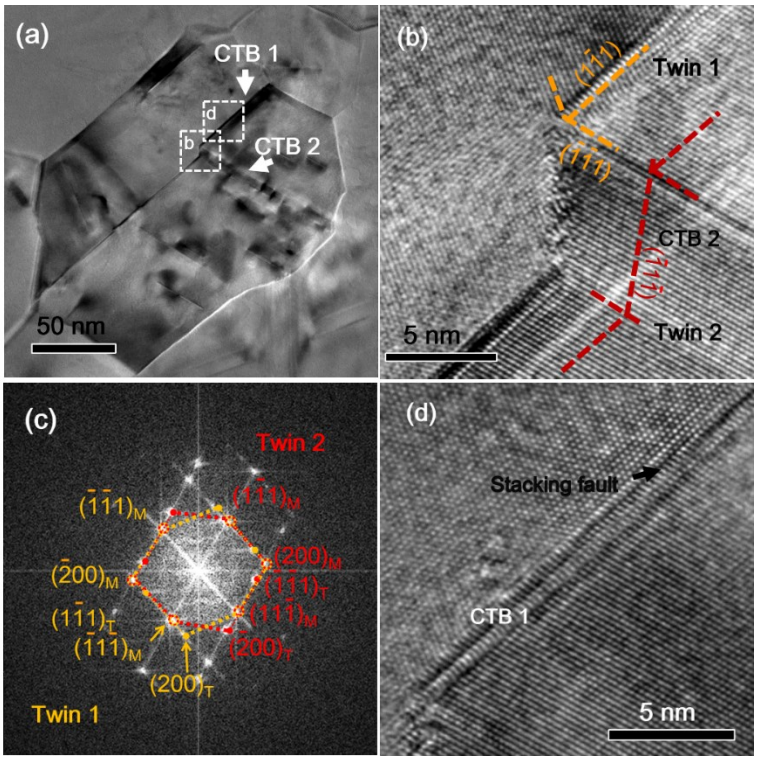

Figure 3.2. Microstructure of long coherent twin boundaries (CTBs) in twinned Al films. (a) Low magnification TEM micrograph of the CTB multi-junction in Al film, h = 40 nm. (b) HRTEM micrograph showing the intersection of CTBs at the junctions. (c) The fast Fourier transform (FFT) of the CTB junctions confirmation the formation of two sets of twins. (d) HRTEM micrograph showing the CTB1 decorated with stacking faults.

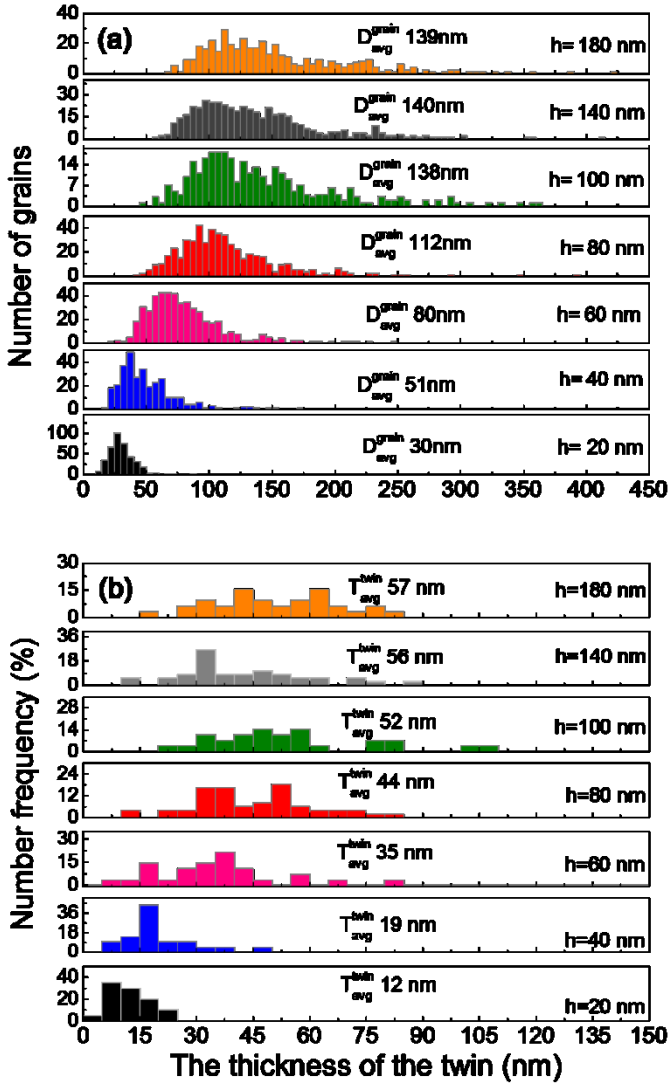

Figure 3.3. Statistic distributions of grain size and twin thickness for Al films with various film thickness. (a) Statistical variation of grain size with different film thickness. The average grain size increases monotonically up to ~138 nm with increasing film thickness to 100 nm, and then reaches a plateau. (b) In parallel the average twin thickness increases to ~ 52-56 nm when h = 100 nm, and reaches a saturation.

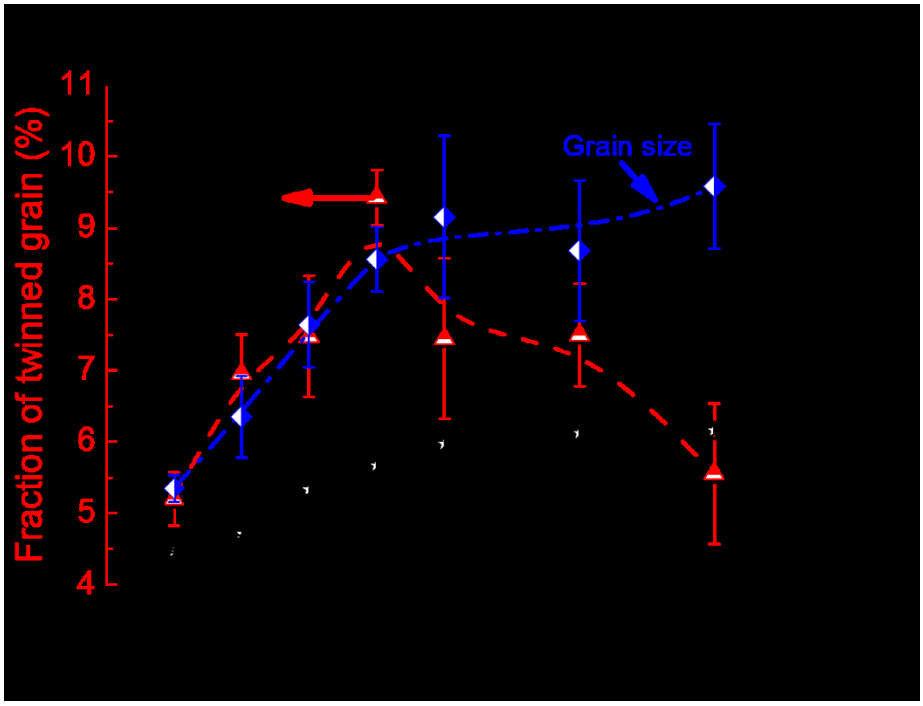

Figure 3.4. The evolution of fraction of twinned grains, average twin thickness and average grain size with Al film thickness. The fraction of twinned grains increases continuously with increasing film thickness, reaches a maximum of ~ 9% when h = 80 nm, and decreases thereafter in thicker films. The average twin thickness and grain sizes increase monotonically with film thickness and approach plateaus when h = 100 nm.

III.5 Discussion

III.5.1 The formation mechanisms of growth twins in Al

Our previous studies show that the epitaxial growth of Al on highly twinned Ag seed layer prompts the extension of nanotwins (nucleated in Ag) into Al films [120]. In this study, however, the twinned polycrystalline Al thin films were synthesized by DC magnetron sputtering without the assistance of any Ag seed layers. From the thermodynamics point of view, it has been shown that an increase in deposition rate will

prompt the formation of growth twins in metals [19]. Such a prediction has been validated in Cu experimentally [171]. Bufford *et al* [60] used the same twin nucleation model [19] to illustrate that twins are rarely observed in Al films even at a very high deposition rate because of its high SFE. However, the previous thermodynamic model, which was constructed based on the assumption that the TB is parallel to the substrate (referred to as a parallel twin hereafter), cannot predicate the emergence of growth twins (most of which are inclined twins) in the current polycrystalline Al films. Parallel twins have been frequently observed in sputtered nt metals, such as Cu, Ag and 330 stainless steels [58, 60, 151]. These sputtered twinned films typically have a strong {111} texture. In comparison, when the nt Ag films have [110] texture, inclined twins have been observed [60]. In the current study, nanotwins in polycrystalline Al were observed in plan-view TEM specimens, implying that a majority of these are inclined twins and TBs intersect the film surfaces.

Cross-section TEM (XTEM) micrographs in Fig. 3.5 (for the Al films grown on Si substrate) show several examples where inclined twins formed. In the first case as shown in Fig. 3.5a, the inclined twins (manifested by CTB) nucleated from Si-film interface and extended into the film (to a height of ~220 nm) until it is terminated by the columnar grain boundary. Note that this film is thicker than most of the films that were grown on TEM washer. The SAD pattern of the same film in Fig.3.5b shows the formation of a {111} CTB. Based on the observation of these inclined twins, we will discuss the revised thermodynamics model to describe the formation of the inclined twins in Al.

III.5.2 A revised thermodynamics model for the formation of inclined twins in metals with high SFE

We will compare the nucleation mechanisms of a perfect nucleus, a nucleus with a parallel twin and a nucleus with an inclined CTB as shown schematically in Fig. 3.6. The perfect nucleus in Fig. 3.6a has the {111} texture. The parallel twin nucleus in Fig. 3.6b has the same texture and the CTB is normal to the growth direction. For the inclined twin nucleus with {100} texture (the mechanism is similar for {110} texture), the {111} CTB formed a finite angle ($\neq 90^o$) with respect to the growth direction. As shown in Fig. 3.6c, the CTB separates the twin nucleus into a right and left section. The right portion of the nucleus has essentially a coherent interface with the matrix, whereas the left portion forms an ITB with the matrix. The angle θ between the CTB and the matrix/nucleus interface plane is the angle between (111) and (100) plane in this scenario. Based on the twin nucleation model developed by Zhang et al [19], during physical vapor deposition, the total Gibbs free energy of a disc-shaped 'perfect' nucleus (ΔG_1), the parallel twin nucleus (ΔG_2) and the inclined twin nucleus (ΔG_3) are given as:

$$\Delta G_1 = 2\pi r h\gamma - \pi r^2 h\Delta G_V \qquad \text{Equation 21,}$$

$$\Delta G_2 = 2\pi r h\gamma - \pi r^2 h\Delta G_V + \pi r^2\gamma_{CTB} \qquad \text{Equation 22, and}$$

$$\Delta G_3 = 2\pi r h\gamma - \pi r^2 h\Delta G_V + l(h/\sin\theta)\gamma_{CTB} + A_{ITB}\gamma_{ITB} \qquad \text{Equation 23;}$$

where the r and h are the respective nucleus radius and height. γ is the surface energy and ΔG_V is the bulk free energy difference between solid and vapor per unit volume driving the nucleation. γ_{CTB} and γ_{ITB} are the respective energy of CTB and ITB. A_{ITB} is the area of ITB at the film-substrate interface. The CTB in the inclined twin nucleus has a truncated

ellipse shape, which can be approximately to be a rectangle. The area of CTB can thus can be calculate as *lh,* where l, the length of the rectangle, is the intersection between the CTB and matrix as shown in Fig. 6c, and the other edge of the rectangle can be estimated as h/sinθ. If the area of the ITB $A_{ITB} = f\pi r^2$, where f is the fraction of the ITB area with respect to the area of the nucleus/matrix interface, then $l = 2\lambda r$, where λ is determined by f.

Then following the prior practice [19], the critical nucleation radius for different type of nucleus can be calculated as:

$$r^*_{perfect} = \frac{\gamma}{\Delta G_V} = \frac{\gamma}{\left(\frac{kT}{\Omega} ln\left[\frac{J\sqrt{2\pi mkT}}{P_S}\right]\right)} \qquad \text{Equation 24}$$

$$r^*_{parallel} = \frac{\gamma}{\Delta G_V - \frac{\gamma_t}{h}} = \frac{\gamma}{\left(\frac{kT}{\Omega} ln\left[\frac{J\sqrt{2\pi mkT}}{P_S}\right] - \frac{\gamma_t}{h}\right)} \qquad \text{Equation 25}$$

$$r^*_{inclined} = \frac{\gamma + \frac{\lambda\gamma_t}{\pi \sin\theta}}{\Delta G_V - \frac{f\gamma_{ITB}}{h}} = \frac{\gamma + \frac{\lambda\gamma_t}{\pi \sin\theta}}{\left(\frac{kT}{\Omega} ln\left[\frac{J\sqrt{2\pi mkT}}{P_S}\right] - \frac{f\gamma_{ITB}}{h}\right)} \qquad \text{Equation 26}$$

Where k is the Boltzmann constant, Ω is the atomic volume and T is the substrate temperature, J is the deposition flux, m is the atomic mass of the deposited metal, P_S is the vapor pressure above solid.

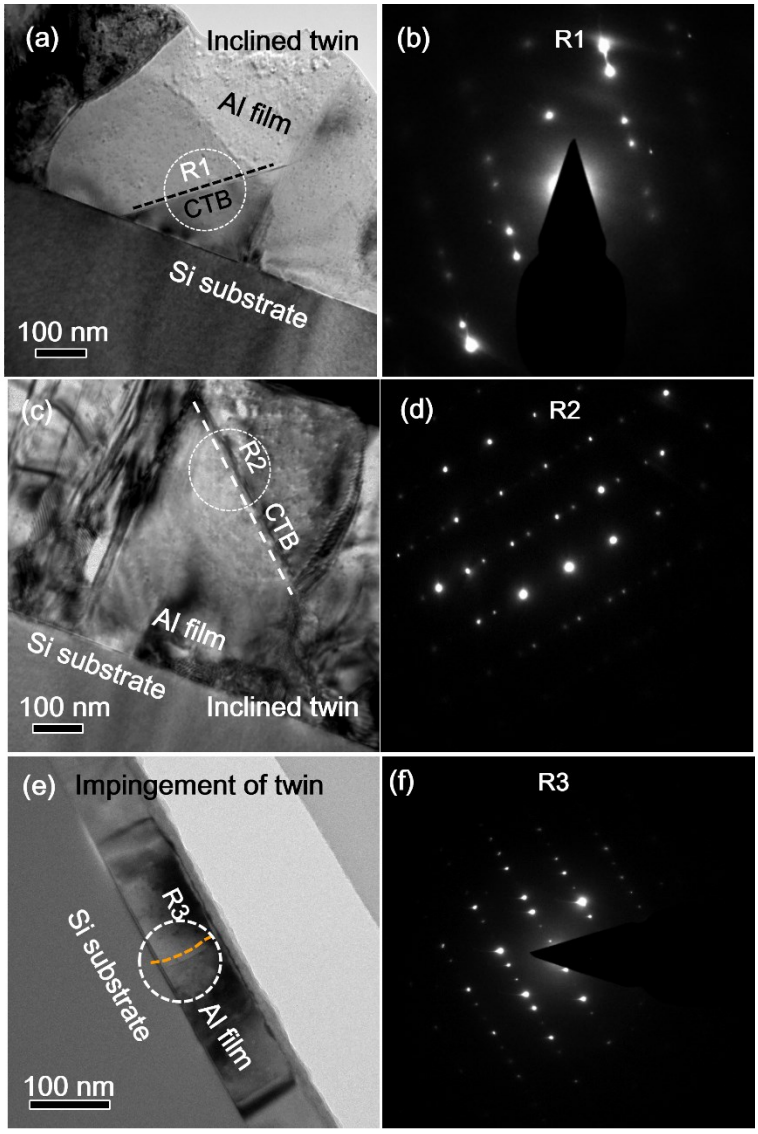

Figure 3.5. Microstructure of inclined twins in Al films on Si substrate. (a) Low magnification cross-section TEM micrograph of the twinned Al films, the inclined twin nucleated at the Si surface. (b) The SAD pattern of R1 in Fig. 5a. (c) Low magnification cross-section TEM micrograph of the twinned Al films, the inclined twin nucleated inside the Al films. (d) The SAD pattern of R2 in Fig. 5c. (f) the SAD pattern of R3 in Fig. 5e.

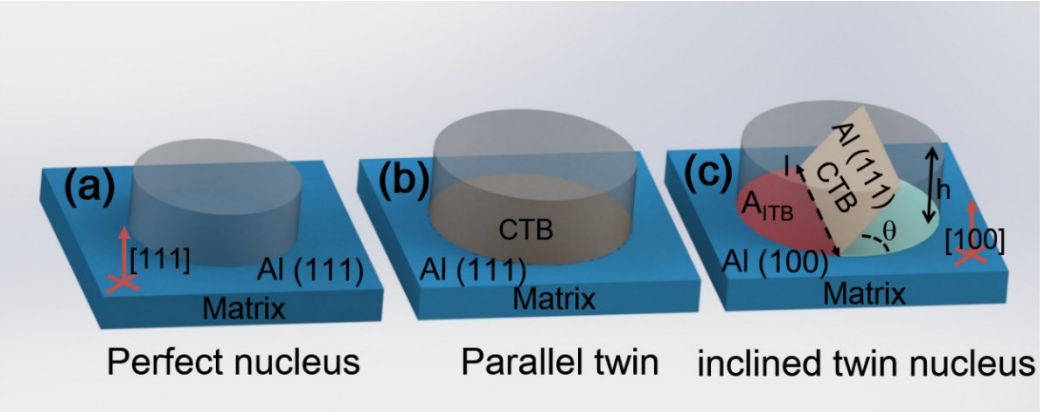

Figure 3.6. Schematic diagrams comparing the nucleation of (a) a perfect nucleus, (b) a parallel twinned nucleus and (c) a nucleus with inclined growth twin on Al matrix. (a) The perfect nucleus and the matrix has the same <111> crystal orientation. (b) The parallel twin nucleus forms (111) CTB on the (111) matrix. (c) A nucleus contains both inclined CTB and incoherent twin boundary (ITB) with the matrix. Note an example of (100) matrix is used to illustrate the concept without losing the generality of the model. A fraction of the matrix-nucleation interface contains ITB with an area of A_{ITB}, whereas the remaining of the nucleus has the same crystal orientation as that of the matrix.

The critical radius difference between the twin nucleus and the perfect nucleus can be used to gauge the possibility of forming different types of twins. The critical radius difference between the parallel (or inclined) twin nucleus and the 'perfect' nucleus is expressed as $\Delta\gamma^*_{pp} = \gamma^*_{para} - \gamma^*_{perfect}$ or $\Delta\gamma^*_{ip} = \gamma^*_{inclined} - \gamma^*_{perfect}$. The area fraction of the ITB in the inclined twin is an important variable that directly impacts the probability of nucleation of an inclined twin. By using f = 25%, 12%, 6%, we can compare the probability of nucleation of an inclined twin with that of a parallel twin. The following values were used in the calculation: γ = 1.3 J/m^2, K = 1.38$\times$10^{-23} J/K, T = 300 K, γ_t = 0.075 J/m^2 and γ_{ITB} = 0.3 J/m^2, h = 2.33$\times$10^{-10} m, P_s =1.07$\times$10^{-5} Pa, and Ω = 1.66$\times$10^{-29}

m^3/atom. J is deposition flux in units of monolayers deposited per second. Amonolayer of Al has an atomic area density of 1.41×10^{19} atom/ m^2 and the deposition rate in our experiments is 0.705 nm/s, thus J is estimated as $\sim 4.2 \times 10^{19}$ atom/ m^2s.

As shown in Fig 7, for the Al film with parallel twins, the value of $\Delta\gamma_{pp}^{*}/rp$ is more than 22% even if the deposition rate is 10 nm/s, implying that it is difficult to form parallel twins. When f = 25%, $\Delta\gamma_{ip}^{*}/rp$ is nearly the same as that of $\Delta\gamma_{pp}^{*}/rp$. However, a continuous decrease in f value can significantly reduce $\Delta\gamma_{ip}^{*}/rp$. When f = 6%, $\Delta\gamma_{ip}^{*}/rp$ drops to below 10% (the horizontal dash line in Fig. 7) at a deposition rate of 0.6 nm/s, implying the possibility to form inclined twins may have increased significantly at the current deposition conditions, 0.7 nm/s. This revised thermodynamic model suggests that the probability for the formation of an inclined growth twin could be much greater than that of a parallel twin, consistent with the observation of predominantly inclined growth twins in polycrystalline Al with high SFE.

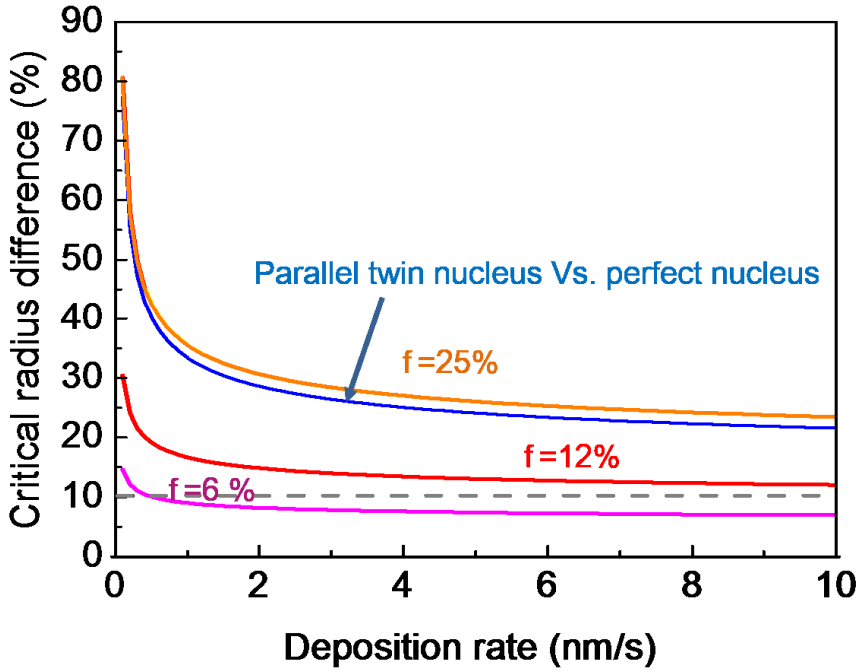

Figure 3.7 Plots of the percentage of critical radius difference between perfect nuclei and parallel twin nuclei $\Delta r_{para}/r_p$ (and between perfect and inclined twin nuclei $\Delta r_{incl}/r_p$, where $\Delta r_{para} = r_{para} - r_p$, $\Delta r_{incl} = r_{incl} - r_p$, and r_p, r_{para}, r_{incl} represent the radius of perfect, parallel and inclined twin nuclei respectively. For parallel twins, r_{para} is at least 25% greater than that of r_p even at a very high deposition rate, implying the nucleation of parallel growth twins in Al is very difficult in comparison for inclined twins, by reducing the area fraction of A_{ITB} to 12% (or less) of the contact area (between matrix and twin nuclei), r_{incl} is merely ~ 10% greater than that of r_p, implying the nucleation of inclined twins in Al is easier than the nucleation of parallel twins.

III.5.3 Promoting the formation of growth twins during the growth of films

Beside the twin embryo formed during the nucleation stage, the twin formation process in Al may also be closely related to the continuous growth of the films. Fig. 3.5b shows that the formation of an inclined CTB originated from the columnar grain boundary

in Al film. The SAD pattern in Fig.3.5d indicates the formation of the inclined growth twin.

As shown in Fig. 3.8a, nuclei with different orientations formed randomly on substrate. Some of the nuclei may contain twins (Fig. 3.8a) and occasionally certain adjacent nuclei may happen to have the twinned orientation as evidenced in XTEM studies in Fig. 3.5e. During island coalescence, larger islands with low surface and interface energy may consume smaller or unfavorably orientated islands driven by the decrease in interface and surface energy (Fig. 3.8b). Meanwhile as shown in Fig. 3.8c, the high angle grain boundaries between the grain 1 and 2, and 1 and 4, could be replaced by a CTB between the grain 1 and 4 as the CTB has much lower energy than a high angle grain boundary, leading to the formation of CTBs during the subsequent growth of the film.

III.5.4 The increase of the fraction of the twinned grains with film thickness (when h≤ 80nm)

As shown in Fig. 3.4, the fraction of the twinned grains rises monotonically to ~ 9.5% when the film thickness increases to 80 nm and decreases afterwards. The fraction of the twinned grains is defined as the number of twinned grains per unit area (P_{twin}) divided by the total number of grains per unit area (P_{grain}). So mathematically it appears that either an increase in P_{twin} or a decrease in P_{grain} will result in a greater fraction of the twinned grains.

However our studies in Fig. 3.9 shows that both P_{twin} and P_{grain} decrease continuously with increasing film thickness. For instance, the P_{twin} decreases from 46 to 18, and then to 7 twinned grains/μm^2 when h = 20, 40 and 80 nm, respectively. In parallel, the value of

P_{grain} decreases at a greater rate, from 861 to 261 and then to 84 grains/μm^2 when h = 20, 40 and 80 nm, respectively. The reduction in the number of grains in thicker films arises from the island coalescence process [172]. When the island coalesced, the twins were terminated at the same time. However, as CTBs typically have lower energy than high angle grain boundaries, they are more stable and may have greater probability to survive during the island coalescence process. Furthermore new TBs may form during impingement of islands as evidenced in Fig. 3.5c and illustrated in Fig. 3.8c. Consequently the fraction of twinned grains increases with increasing film thickness when h is 80 nm or less.

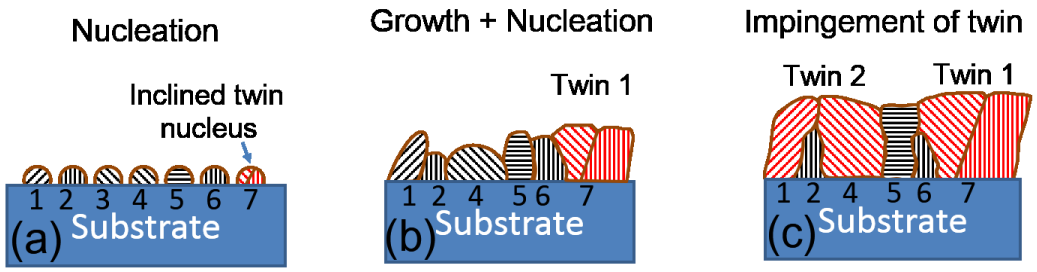

Figure 3.8. Schematics illustrating different twin formation mechanisms. In the first case, inclined twins may nucleate directly on the matrix as shown in (b). In the second case, two grains, 1 and 4, with twin orientation may impinge upon each other as shown in (c) to form a twin boundary during the growth of films.

III.5.5 The decrease of the fraction of the twinned grains with film thickness (when h≤ 80nm)

When h > 80 nm, the fraction of the twinned grains decreases as shown in Fig. 3.4. A notable phenomenon in this regime is that the average grain size approaches a plateau ~140 nm (or P_{grain} becomes a constant), because the films have entered the regime of a continuous growth of the columnar grains instead of islands coalescence. Correspondingly, the decrease of the fraction of the twinned grains results from the reduction of P_{twin}.

To explain the termination of twins during continuous growth of films when grain size saturates, we need to consider the energetics for the growth of CTB and ITB for the inclined twins. As shown schematically in Fig.3.10, the length of CTBs for inclined twins is proportional to the film thickness and hence the continuous growth of the CTBs with increasing film thickness will increase the total energy of the system. As the inclined CTBs extends to the film surface, there is no ITBs (or there is no extra energy necessary to create ITBs). It is important to realize that the termination of CTBs inside the films imply the necessity to form ITBs within the films. In Fig. 3.10a, there are two inclined twins (thin vs. thick) inside the film (h > 80 nm) during the early growth stage. As shown in Fig. 3.10b, if the total energy of the CTBs (W_{CTB}) of the thin twin exceeds the formation energy of the ITB (W_{ITB}), the possibility to form an ITB will increase and the formation of the ITB terminates the continuous growth of the CTBs. Consequently the number of twinned grains (examined from plan-view TEM) will decrease. But the thick twin may continue its growth with the increase of film thickness because the energy $W_{ITB} \geqslant W_{CTB}$, or it is much

more energetically costly to terminate a thick twin inside the film. The thick twin is eventually terminated when $W_{CTB} \geqslant W_{ITB}$ (Fig. 3.10c).

Foregoing discussions suggest that the growth of twins in thicker films could be affected by the energy minimization considering the energy difference between W_{ITB} and W_{CTB}. W_{ITB} can be approximated as $\alpha T_{twin} E_{ITB}$, where α is a constant related to the inclined twin angle and E_{ITB} is the formation energy of an ITB per unit area. Similarly, $W_{CTB} = bhE_{CTB}$, where b is a constant which related to the inclined twin angle and E_{CTB} is the energy of the CTB per unit area. α, b, E_{ITB} and E_{CTB} are constants independent of film thickness. When $W_{CTB} = W_{ITB}$, an inclined dash-dot line is obtained as shown in Fig. 3.11. As discussed previously, the energy discrepancy between the ITB and CTB suggests the possibility to form an ITB. When $W_{ITB} > W_{CTB}$ (to the left side of the straight line), it is energetically feasible to extend the inclined growth twins during the growth of films. Whereas when $W_{ITB} < W_{CTB}$ (to the right side of the straight line), the continuous growth of the CTBs becomes energetically unfavorable. Consequently, the growth of a CTB will be terminated, leading to a reduction of the fraction of the twinned grains.

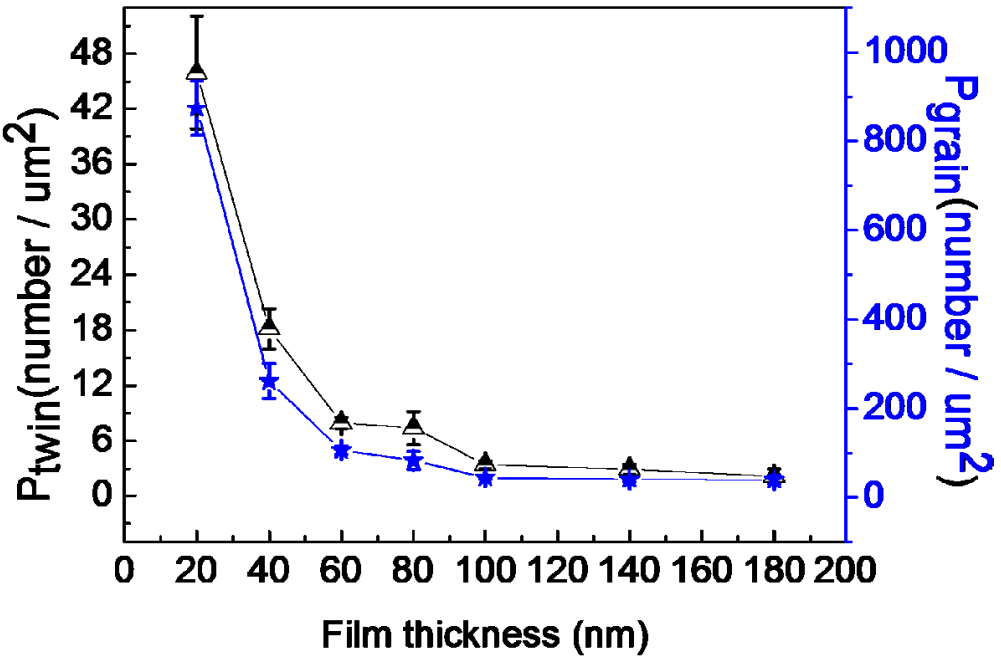

Figure 3.9. Plots of twinned grain density and grain density versus film thickness. Twinned grain density follows the tendency of grain density with the increase of film thickness. The density drops quickly before film thickness reach 60 nm and goes to plateaus gradually.

The reduction of the fraction of the twinned grains may also be related to the lack of continuous grain growth (or a lack of island coalescence). As mentioned earlier twins may nucleate during island coalescence, and thus the lack of island coalescence may reduce the probability to form growth twins. The current study on the formation of growth twins in polycrystalline Al is an important forward step towards the eventual goal - the synthesis of high density nanotwins in Al without buffer layers. There are numerous questions that remain to be examined in future studies, including the peculiar constant ratio between the average twin thickness and average grain size observed in this study.

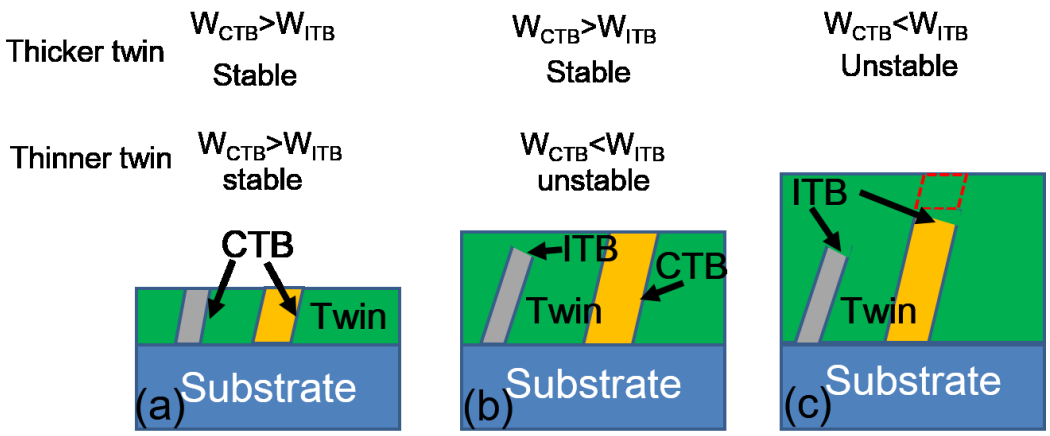

Figure 3.10. Schematics illustrating the termination of thin inclined twins and continuous growth of thick inclined twins in Al by using the energy balance concept. When the energy of CTBs is less than or equal to the formation energy of ITB, the inclined twins may grow continuously (a). In contrast, the growth of inclined twins become difficult when the opposite holds true. Thus, the growth of thinner twins terminates earlier than thicker twins (b-c).

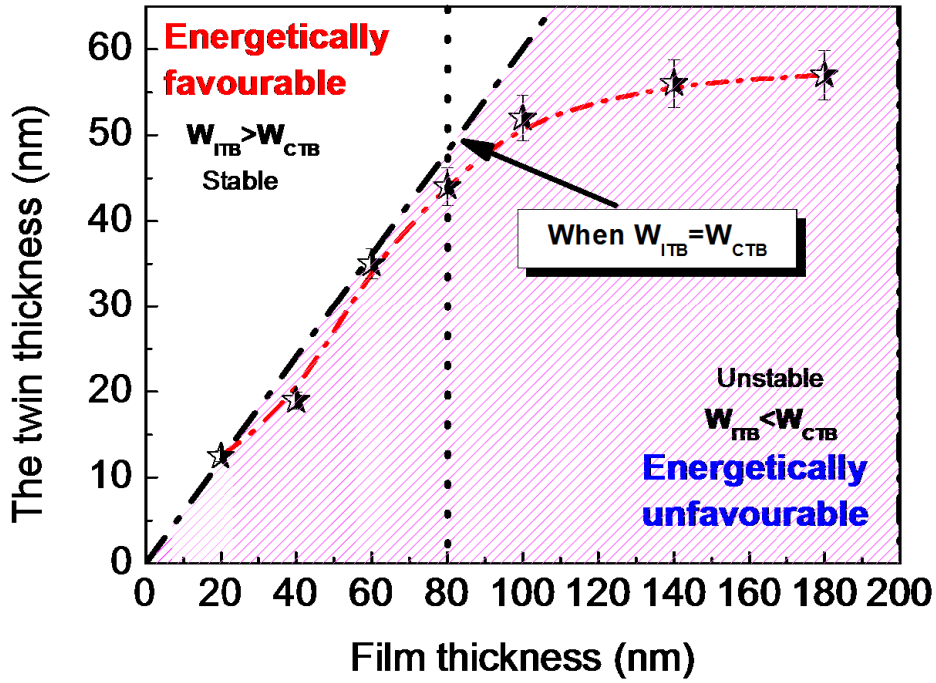

Figure 3.11. Using the energy balance concept illustrated in Fig. 8 a dash-dot line is obtained when the energy of ITB is equal to the energy of CTB ($W_{ITB} = W_{CTB}$). Above this line, $W_{ITB} > W_{CTB}$, implying the growth of twins above certain thickness is stable. In comparison, the shadowed area indicates that the growth of CTBs is costly and it is energetically favorable to terminate the growth of CTBs. The superimposed average twin thickness data align well with the prediction (dash-dot line) when $h \leq 80$ nm. However, in thicker films ($h \geq 100$ nm), the average twin thickness falls below the threshold value, indicating the growth of these twins becomes increasingly difficult.

III.6 Conclusions

Sputter-deposited polycrystalline Al films contain growth twins and the fraction of twinned grain increased with increasing film thickness to a maximum value, ~ 9.5 %, when h = 80 nm, and decreased thereafter in the thicker films. An inclined twin nucleation model has been provided from the thermodynamics perspective to explain the formation mechanism of the growth twins in Al films. The termination mechanism for the growth of

the inclined twins in thicker films may be related to the competition between the energy of CTB and ITB, the elimination of fine nanotwins, and the lack of grain growth via island coalescence. Although the fraction of twinned grains remains low, the twin formation mechanisms presented in this study suggest new perspectives to tailor the formation of grow twins in high SFE metals, such as Al.

CHAPTER IV

HIGH-VELOCITY PROJECTILE IMPACT INDUCED 9R PHASE IN ULTRAFINE GRAINED ALUMINUM

IV.1 Overview

Aluminum (Al) typically deforms via full dislocations due to its high stacking fault energy. Twinning in Al, though difficult, may occur at low temperature and high strain rate. However, the 9R phase rarely occurs in Al simply because of its giant stacking fault energy. Here by using a laser induced projectile impact testing technique, we discover deformation induced giant 9R phase (tens of nm in width) in ultra-fine grained Al for the first time, as confirmed with extensive post-impact microscopy analyses. The stability of 9R phase is related to the existence of sessile Frank loops. Molecular dynamics simulations reveal formation mechanisms of 9R phase in Al. This study sheds lights on a new deformation mechanism in metals with high stacking fault energy.

IV.2 Introduction

Coarse-grained (CG) metals with face-centered-cubic (FCC) structure typically deform by glide of full dislocations [173]. When stacking fault energy (SFE) is low, deformation of FCC metals is often accommodated by abundant partial dislocations [174]. Furthermore, prior studies show that grain size can tailor the nature of dislocations during deformation. For instance, ultra-fine grained (UFG, with grain sizes of 100-1000 nm) and

nanocrystalline (NC with grain sizes of 100 nm or less) FCC metals can deform via slip (partial dislocations) or twinning (consecutive emission of partial dislocations on adjacent {111} planes) [54, 99], since the Frank-Read sources become more difficult to operate when the grain size is less than 1 μm [175, 176]. But in FCC metals with high SFE, deformation twinning is in general difficult to occur [177, 178]. Van Swygenhoven *et al.* show that deformation twinning tends not to occur in NC Al (with a grain size of 12 nm or less) with high SFE, ~ 160 mJ/m^2 [125], because the high ratio of SFE vs. unstable SFE facilitates the nucleation and emission of trailing partials, which eliminate SFs associated with the glide ofleading partials.

Meanwhile, Yamakov *et al.* predict that deformation twinning can occur in NC Al with grain sizes of 45 and 70 nm [8]. Experimental studies show that deformation twins indeed form, but with a very low probability, in NC and CG Al that are deformed at low temperature and high strain rate [166], [96, 107]. When grain size decreases to nanoscale, the GB-mediated deformation mechanisms may take over, reduce the probability of deformation twinning [12, 149].

9R phase has been observed in FCC metals with low SFE, such as Cu (45 mJ/m^2 [111, 179]), Ag [113] and Au [118],. 9R structure is a stacking ribbon and consists of a repeating unit of 9 {111} atomic layers (6 stacking fault {111} planes and 3 normal stacking {111} planes). Thus 9R phase has much high formation energy than a twin (containing only two stacking fault planes). Although deformation twinning has been observed in high SFE metals under extreme deformation conditions, the formation of 9R

phase via plastic deformation has never been reported in pure Al because the 9R phase is difficult to nucleate and is highly unstable even if nucleated.

In this study, we investigate the deformation mechanisms of sputter-deposited UFG Al thin film (containing a certain fraction of growth twins [180]) subjected to high-velocity micro-projectile impacts by using a laser induced projectile impact test (α-LIPIT) technique [181-183].

Extensive post-mortem transmission electron microscopy (TEM) studies reveal several tens of nm wide giant 9R phase in the impacted UFG Al, as well as high-density dislocation networks, and grain rotation and fragmentation. MD simulations provide an in-depth understanding on the deformation mechanisms of UFG Al and the formation of 9R phase under projectile impact.

IV.3 Experimental

To explore the deformation mechanisms of UFG Al at high strain-rates, we used a recently developed LIPIT technique, where high-velocity monodispersed silica microspheres (~3.7 μm in diameter) impact and penetrate the UFG Al film. The Al thin films, 140 nm in thickness, were deposited onto a carbon film (25 nm thick) coated copper TEM grid. Thus, these UFG Al films are "semi" free-standing.

Individual silica microspheres were launched, by using a laser pulse, towards Al films at high velocities (~600 m/s) to generate high-strain-rate (~ 10^8 s^{-1}) deformation in a local region. Approximately a dozen impact experiments using silica micro-projectiles

were performed at different grid areas (i.e. each time the projectile impacts a pristine portion of the UFG Al films).

Free-standing films are used to avoid the complexity of back-stress waves that are typically seen in bulk shock-loaded specimens. After the projectile penetration experiments, the shape of the perforated holes in UFG Al film was examined using an FEI Quanta 600 scanning electron microscope operated at 10 kV. TEM analysis was performed on an FEI Tecnai F20 ST microscope operated at 200 kV to characterize the evolution of microstructure near the impacted zones. To further probe the impact induced microstructure damage in UFG Al films, high-resolution TEM (HRTEM) experiments were performed.

IV.4 Result

Electron backscatter diffraction (EBSD) micrograph and the corresponding orientation mapping analysis (in Fig. 4.1) show that the as-deposited films have ultra-fine grains with high-angle GBs. The grain size of Al films (Fig. 4.3) varies from 60 to 350 nm, with an average of ~140 nm. The red lines in Fig. 4.1a indicate the Σ3 {111} TBs in as-deposited films.

To differentiate Σ3 coherent and incoherent twin boundaries (CTBs and ITBs), we need to examine the boundary rotation axis (BRA). As shown in Fig. 4.1b, the BRA is parallel to the ITB, but perpendicular to the CTB. TEM micrographs (Fig. 4.1c-d) and the inserted selected area diffraction (SAD) pattern confirm the formation of CTBs in the UFG

Al film. A plan-view TEM micrograph (Fig. 4.2a) and the inserted SAD pattern show the polycrystalline nature of the UFG Al film.

A cross-sectional TEM micrograph shows the columnar grains (Fig. 4.2b). As shown schematically in Fig. 4.2c, individual SiO_2 microspheres (3.7 μm in diameter) used in the the α-LIPIT experiment launch to impact the free-standing UFG Al films deposited on TEM washer containing grids shown in a scanning electron microscopy (SEM) micrograph in Fig. 4.2d. Most of the perforated holes have a circular shape with a diameter similar to that of the SiO_2 projectiles (Fig. 4.4). TEM micrograph in Fig. 4.2e shows a representative circular hole after microprojectile penetration. A noteworthy characteristic of the majority of the impacted zones is the limited number of cracks surrounding the holes in the high strain-rate impacted UFG Al films.

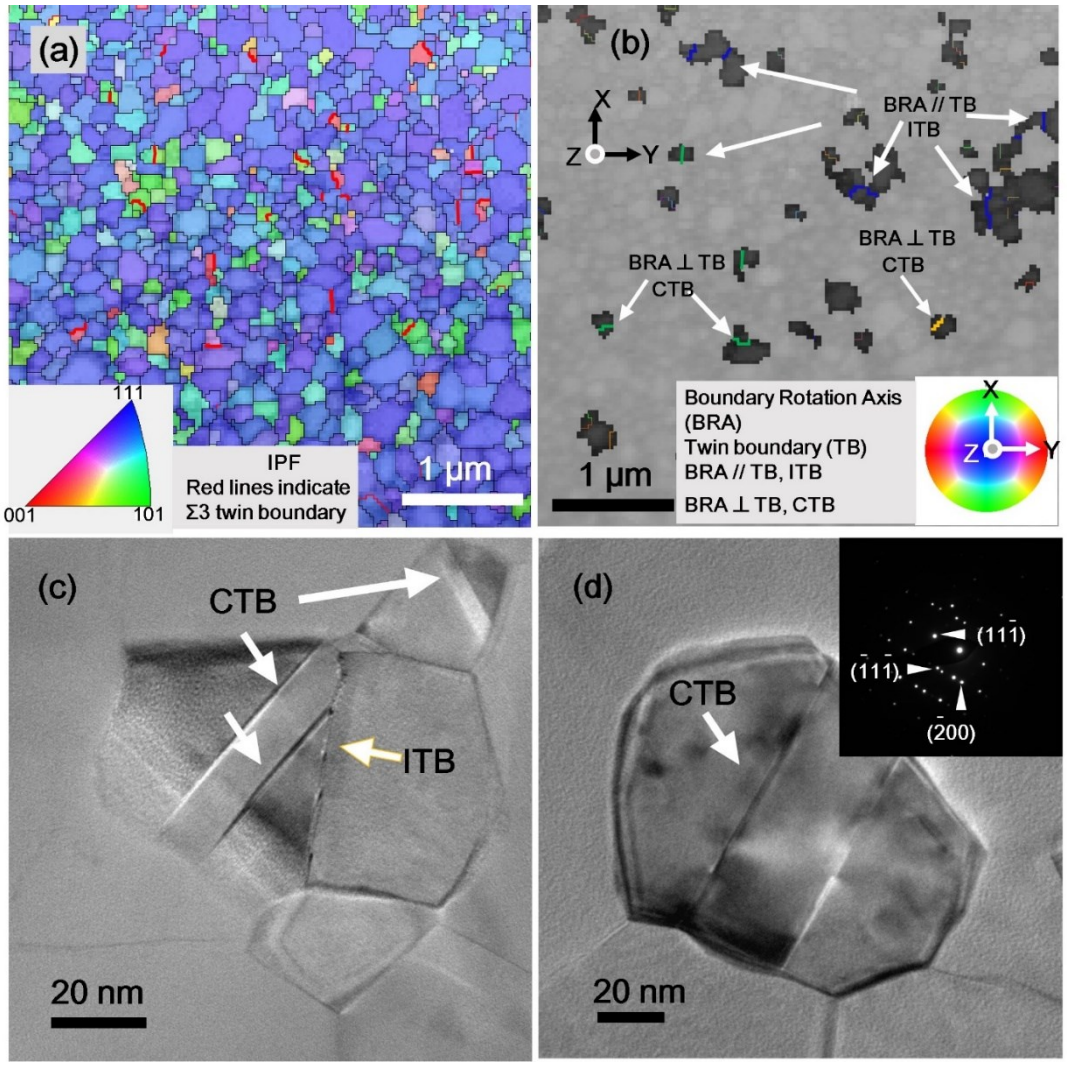

Fig. 4.1 Microstructures of as-deposited UFG Al thin film. (a) EBSD micrograph showing orientation map along the sample surface normal direction; the red lines indicate Σ3 twin boundary. (b) The boundary rotation axis (BRA) map reveals the incoherent twin boundary (ITB) (when BRA // TB) and coherent twin boundary (CTB) (when BRA ⊥ TB). (c-d) Plan-view TEM images showing growth twins in as-deposited UFG Al thin films (insert of (d) shows the selected area diffraction (SAD) pattern of grain containing growth twins).

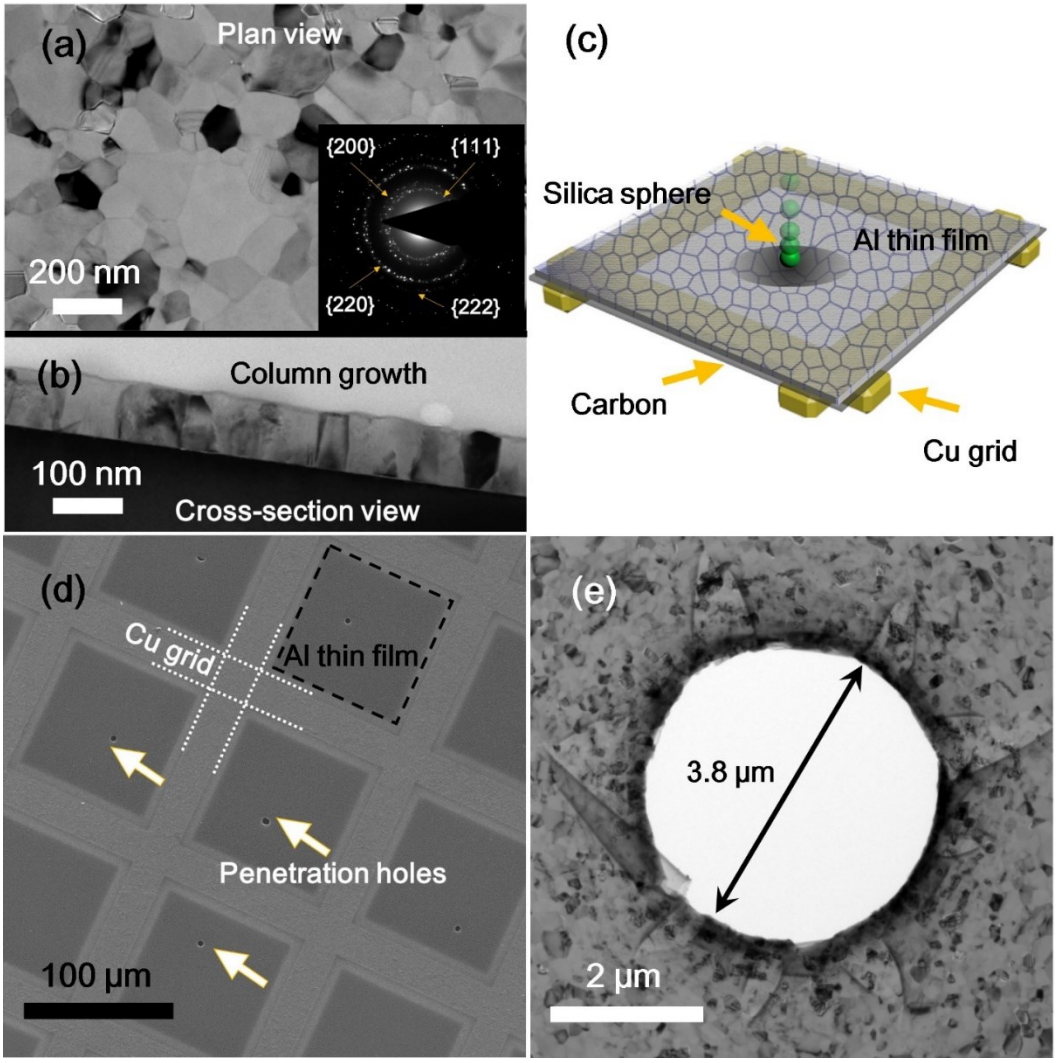

Fig. 4.2 A laser induced projectile impact testing (α-LIPIT) technique for the study of high-strain-rate response of UFG Al films with a thickness of 140 nm. (a) A plan-view TEM micrograph showing the as-deposited UFG Al film. (b) The cross-section view of the as-deposited Al thin film showing columnar grains. (c) A schematic of the α-LIPIT experiment. (d) A low magnification SEM micrograph showing the perforations induced by microprojectiles in UFG Al film supported by Cu TEM grid. (e) A representative TEM image showing the morphology of a circular perforation.

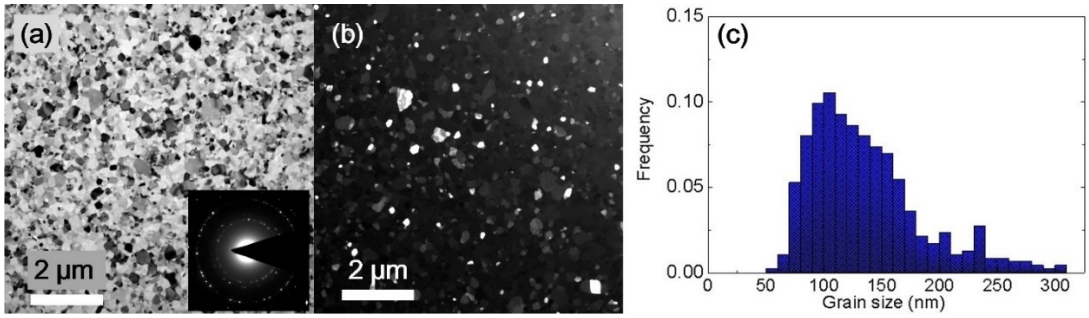

Fig. 4.3 Microstructure of the as-deposited polycrystalline Al thin film. (a) A bright-field TEM image and inserted selected area diffraction (SAD) pattern showing the formation of high angle grain boundaries and ultra-fine grains. (b) A dark-field TEM micrograph showing the formation of UFGs. (c) The grain size statistic distribution showing the average grain size of 140 nm in as-deposited films.

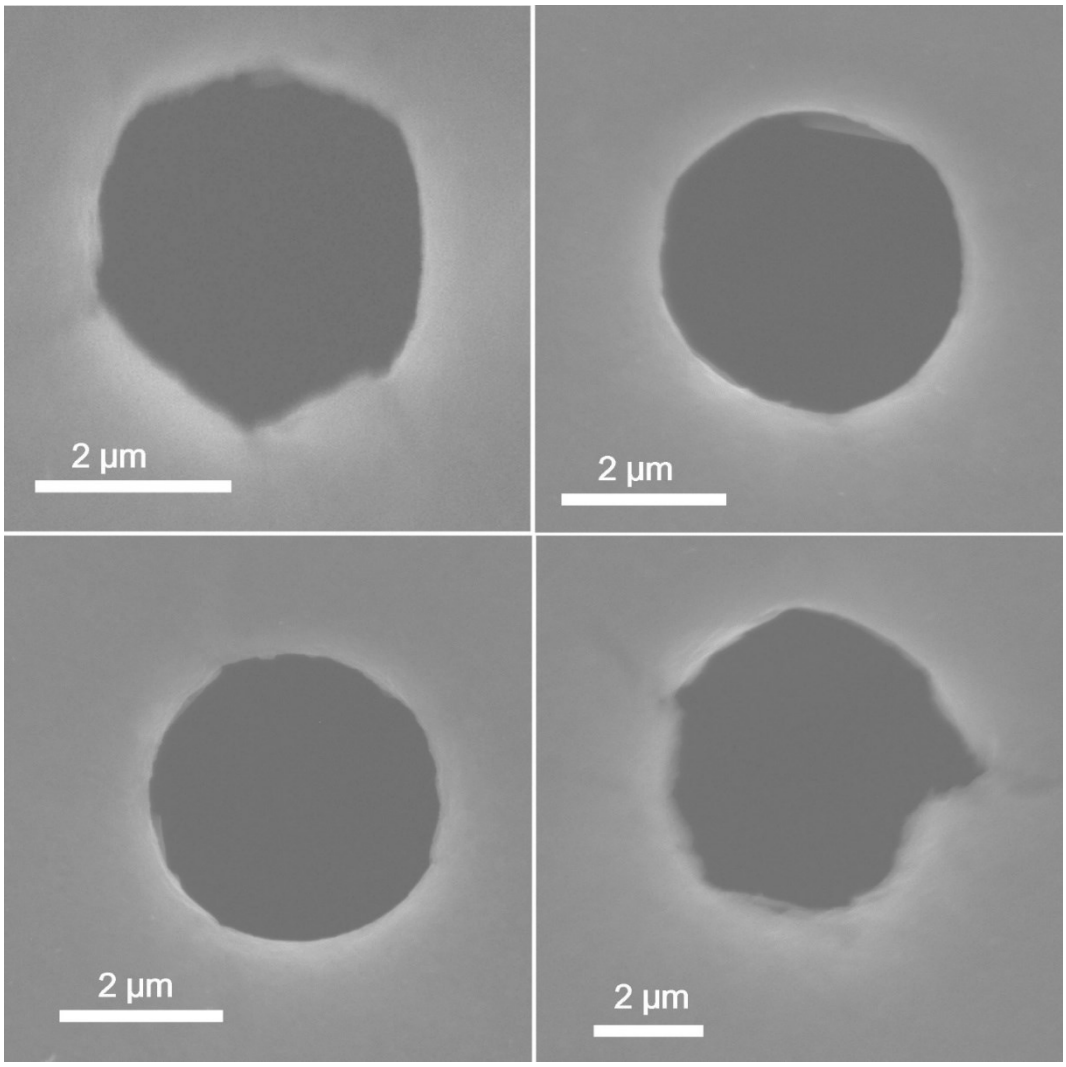

Fig. 4.4 A selected collection of SEM gallery showing analyzed projectile perforations in UFG Al films.

A striking phenomenon is the formation of an 80 nm wide 9R phase in the highly deformed regions near the edge of the perforation. Figure 4.5a shows a typical deformation twin formed near the edge of a hole. Inside the grain, the white dashed line indicates two parallel CTBs. At the end of the two TBs, a dashed orange line marks the boundary of a broad 9R phase bounded by the TBs. The curved phase boundaries separating the 9R phase from matrix are marked by PB1 and PB2, indicating the location of leading (PB1) and trailing (PB2) partials.

One section of the 9R phase near the upper TB is analyzed by HRTEM. As shown in Fig. 4.5b, near the left side of the giant 9R phase, multiple SFs have been observed. Besides SFs, numerous Frank partial dislocations were also identified within the 9R phase. The magnified view of the 9R phase in Fig. 4.5c confirms the three-layer periodic stacking sequence typically observed in the 9R phase. The magnified view of box 2 (in Fig. 4.5d) shows the deformation induced CTB containing abundant Shockley partials. Fig. 4.5e shows the schematics illustrating the formation of 9R phase and CTBs to be discussed later.

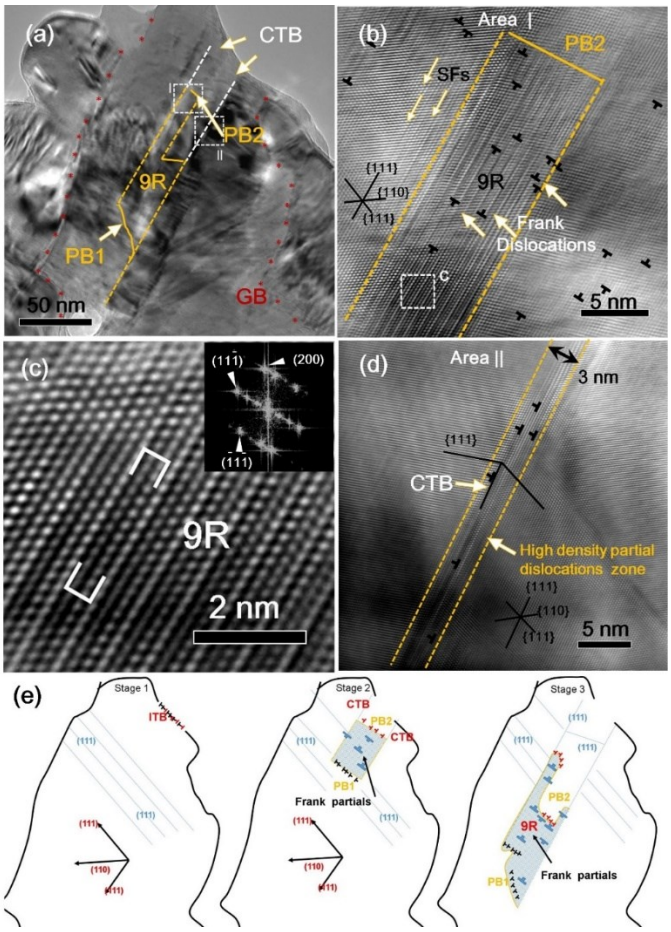

Fig. 4.5 Projectile impact induced 9R phase in UFG Al films. (a) Overview of the microstructures of UFG Al adjacent to the edge of the perforated hole. CTBs bounding a giant 9R phase are identified. The forward and backward phase boundary (PB) separating 9R from matrix are also labeled. Two white boxes outline the defects shown at higher magnification in Fig. 3c, 3d. Red asterisks outline a grain boundary (GB). (b) HRTEM micrograph reveals the formation of the giant 9R phase in UFG Al after impact. Numerous Frank partials are also observed in the 9R phase. (c) The HRTEM micrograph of the CTB from area 2. High-density Shockley partials are identified along the CTB. (d) HRTEM micrograph of the white box in Fig. 3b showing the 9R phase. (e) A schematic shows the deformation induce 9R phase and TBs. A section of the GB has ITB nature with one Shockley partial on each adjacent {111} plane. High strain-rate impact triggers the migration of leading partials, followed by trailing partials. 9R is bounded between the leading and trailing partials. Sessile Frank partials also form within the 9R phase. Frank partials pin the trailing partials, leaving 9R phase intact after high strain-rate impact.

Besides the 9R phase and deformation twins, grain fragmentation is also frequently observed. A dark-field TEM micrograph in Fig. 4.6a shows the microstructure of films can be separated into two different zones: a highly deformed zone 1 adjacent to the edge of a circular perforation, with a width of ~ 1.5 μm, and a less impacted zone 2 outside the deformation zone 1. Most grains in zone 2 have well-defined GBs and relatively uniform interior contrast. While inside the deformation zone 1, especially near the edge of the perforation, much smaller grains with irregular GBs are frequently observed. Comparison of the grain size distributions in the two zones (Fig. 4.6b) shows that the average grain size is reduced in zone 1. Although grain fragmentation dominates the grain morphology evolution inside the highly deformed area, grain coarsening has also been observed occasionally. As shown in Fig. 4.6c, a large elongated grain containing a high-density of dislocations was observed near the edge of a penetration (in a different specimen). The inserted SAD pattern from the area marked by the white dash-dot line shows the single crystal like diffraction pattern captured along the [001] zone axis. The large misorientation angle (greater than 20 degrees) in the stretched {220} diffraction spots indicates subgrain rotation during the formation of the large grain.

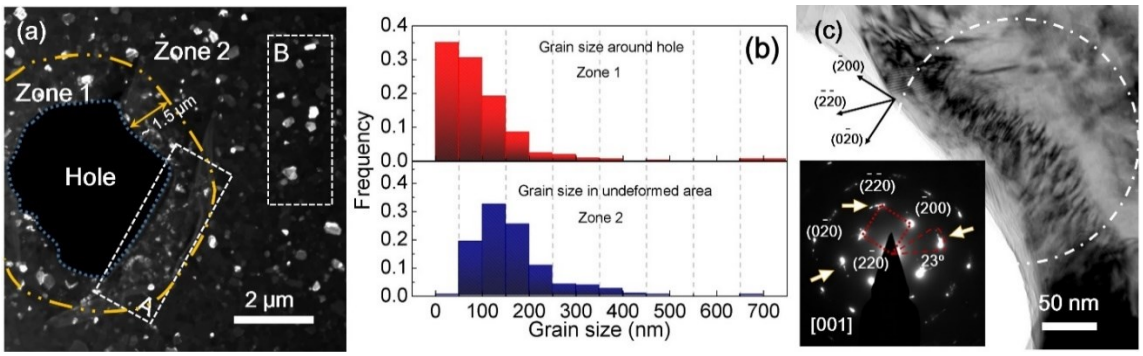

Fig. 4.6 Grain fragmentation and coarsening near the perforations. (a) A dark-field TEM image of the nanograins near a perforation. The grains in area A in zone 1 (within the 1.5 μm wide impact zone) are smaller than those in area B in zone 2 (away from the impact zone), indicating grain fragmentation during projectile impact. The yellow dash-dot line delineates the boundary between zone 1 (highly impacted zone) and zone 2 (less deformed area). (b) The statistical distribution of grain sizes in Fig. 4a in zone 1 and 2. (c) A low magnification bright field TEM micrograph showing the morphology of an elongated grain containing a high density dislocations near a perforated hole. The length of the grain is ~ 300 nm, and its width is ~ 70 nm. The inserted diffraction pattern shows the slightly axisymmetric elongated {220} diffraction spots examined along <100> diffraction zone axis, indicating the subgrain rotation within the grain.

In addition to grain fragmentation, high-density dislocations induced by high strain rate impact are observed in deformed grains, and defect density depends on the relative distance of the grains to the perforated holes. In general, high-density dislocations are frequently observed in grains located within zone 1 as shown in Fig. 4.7a. Furthermore, many grains in zone 1 have irregular shapes and complex stress contours. Fig. 4.7b shows tangled dislocations aligned nearly orthogonal to one another in a large grain in area B of zone 1. Another adjacent large grain in area C of zone1 contains high-density parallel dislocation networks. Extensive TEM tilting experiments were performed to examine dislocations in deformed grains (Fig. 4.8). Grains in zone 2 typically have fewer defects/dislocations and relatively straight GBs. Although grains in zone 2 typically have less internal defects, arrays of high-density dislocations are frequently observed in grains containing CTBs (growth twins). Fig. 4.7d shows the enlarged image of the box D in zone 2, where an array of black dots was observed running straight across the entire grain. The black dots arise from the edge-on view of dislocation cores, and the straight line is a CTB of a growth twin inside the grain. Similar arrays of high-density dislocations have been frequently observed in numerous other grains in zone 2 containing growth twins (Fig. 4.9).

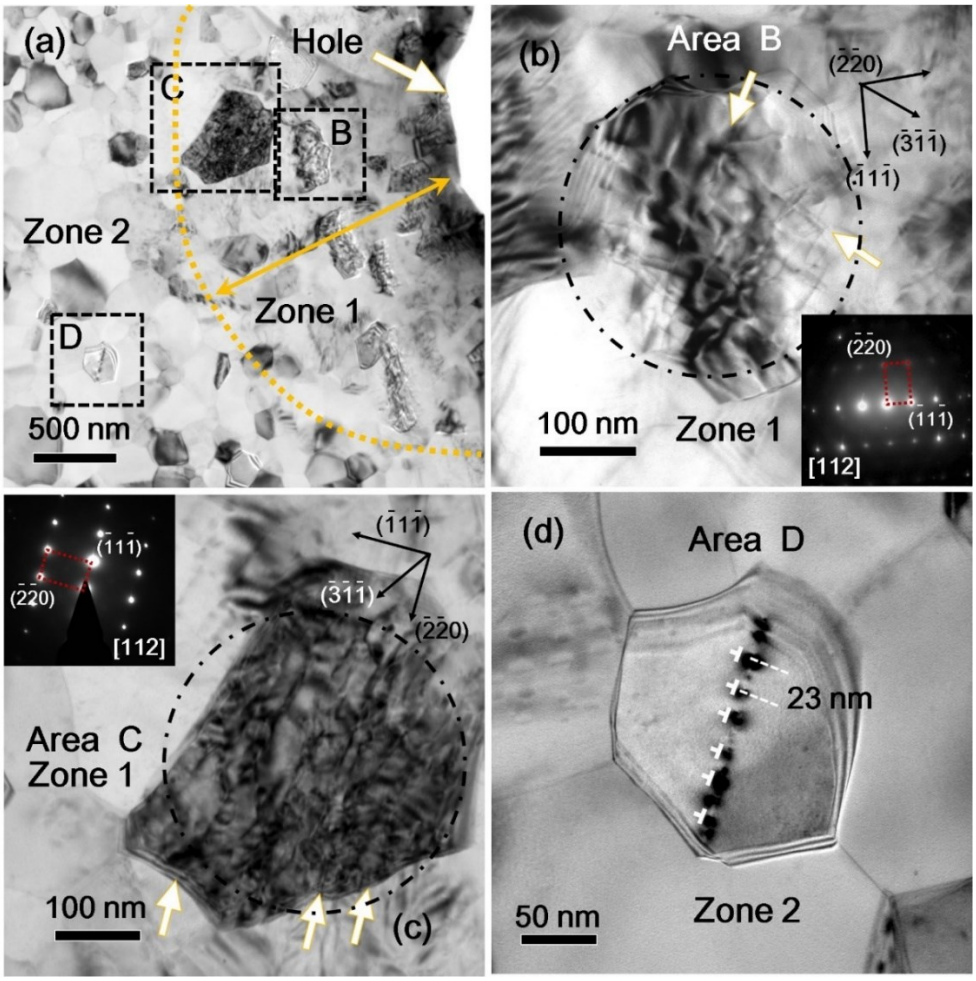

Fig. 4.7 The presence of dislocation networks in the deformed zone after ballistic impact. (a) A low magnification TEM micrograph showing the alteration of the microstructure near a perforated hole in UFG Al. Grains in zone 1 (adjacent to the hole) have greater defect density than those in zone 2 (away from the hole). (b-c) The observation of dislocation networks in areas B and C (in Fig. 5a). The white arrows indicate the traces of dislocations in large grains examined along <112> zone axis. (d) A higher magnification TEM image of the area D in zone 2 showing the edge-on view of an array of dislocations aligned along a CTB. An array of dislocation cores, separated by ~ 20 nm, is identified.

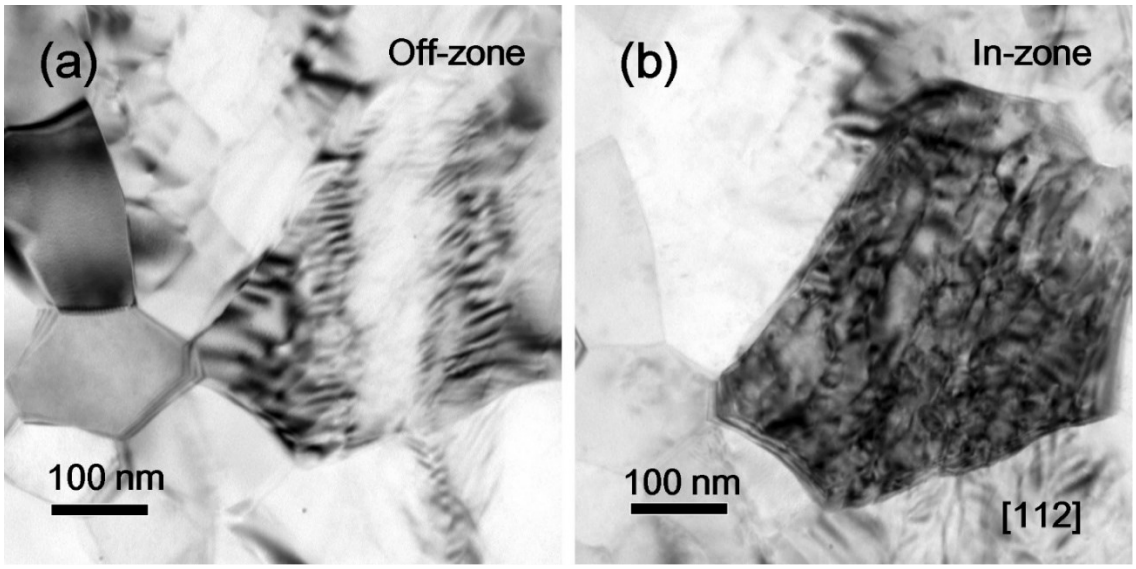

Fig. 4.8 The TEM tilting experiment to examine the morphology of dislocation networks in grains in zone 1 (highly impacted zone near holes). (a) When tilted off the <112> zone axis, the dislocation density in the large grain in the impacted zone appears low. (b) In contrast, when titled to the <112> zone axis, a high-density of dislocations become visible.

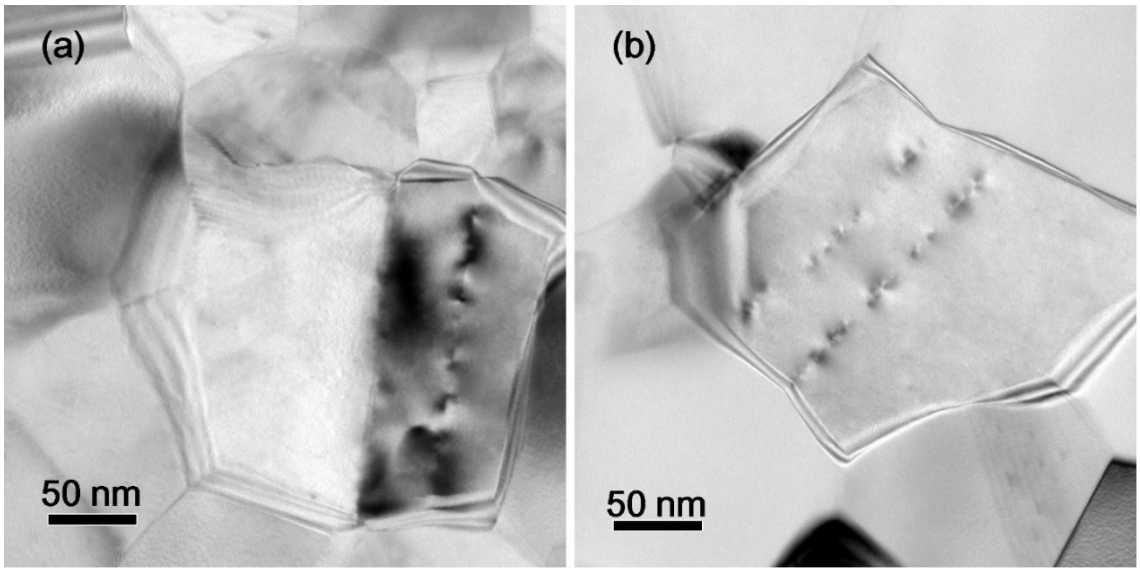

Fig. 4.9 TEM images showing the accumulation of dislocations along the preexisting CTBs in grains in zone 2 (less impacted zone, away from the perforated holes). The CTBs are growth twins introduced during sputtering. The interactions of impact induced dislocations with CTBs lead to the storage of dislocations (manifested by their cores) along the CTBs. Other than dislocations along TBs, the grain interior appears to have few dislocations.

IV.5 Discussion

In FCC metals with low SFE, the core of 1/2 <110> full dislocation can dissociate into two Shockley partial dislocations connected by a SF, which is also referred to as an extended dislocation [173, 184]. Abundant deformation twins or SFs have been observed in deformed FCC metals with low SFE [69, 70, 79, 84, 85, 90, 99]. In contrast, plastic deformation of monolithic CG Al typically does not lead to deformation twins or SFs due to its high SFE [185, 186]. However, there is increasing evidence of deformation twinning in NC Al both experimentally and computationally [53, 93, 95, 96, 107, 166]. MD simulations [95] revealed three types of deformation twinning mechanisms in NC Al,

including 1) the overlapping of two extended dislocations on adjacent slip planes; 2) successive emission of multiple Shockley partials from GBs; and 3) GB splitting and migration induced formation of TBs. Zhu *et al.* [99] reviewed various mechanisms that articulate the influence of small grain size on promoting the formation of deformation twins in NC Al, Ni, and Cu, including monotonic activation of partials (MAP) and random activation of partials (RAP) [104]. Wu *et al.* hypothesize that RAP is more favorable than the MAP twinning mechanism since RAP induces little macroscopic strain, alleviating the strain on neighboring grains [104]. Deformation twining in Al remains a difficult, high energy process as shown by the spontaneous detwinning during *in situ* tensile experiment under TEM [187, 188].

Recently a growth-induced 9R phase has been observed in FCC metals with low SFE. Sputter-deposited Cu and Ag films both contains nanoscale growth twins and 9R phases [58, 60, 146]. Liu et al. [122] observed a deformation induced 9R in Ag. The nucleation and migration of a Σ3{112} ITBs facilitated the formation of 9R with zero net strain in Ag [49]. However a deformation induced 9R phase in Al has never been reported. It is natural to speculate that the lack of 9R phase in deformed Al is due to its ultra-high SFE. Hence the formation of giant, 80 nm wide, 9R phase regions in UFG Al is surprising.

As shown in Fig. 4.1a-b, as-deposited UFG Al has {111} texture and contains both CTBs and ITBs. These twin seeds may assist the formation of the 9R phase under high strain-rate deformation. As shown in Fig. 4.5e, at stage 1, a portion of the GB consists of ITBs. Under high strain rate impact, the leading partials slip along {111} planes. As trailing partials lag behind, the 9R phase is formed between the leading and trailing partials

as shown in stage 2. To minimize the system energy due to the formation of the 9R phase, the trailing partials move towards the leading partials. Finally the leading partials stop when the shock-induced stress is insufficient to drive their further migrations (stage 3). The rapid propagation of ITB seeds under high strain rate deformation by the projectile impact may lead to the formation of 9R phase in UFG Al. Furthermore, in contrast to the sharp straight 9R phase reported in Ag and Cu with low SFE [49, 122], the boundaries of 9R phase in impacted UFG Al are curved and distorted.

Atomistic simulation methods, particularly nonequilibrium molecular dynamics (NEMD), offer a great and largely untapped potential for the investigation of shockwave processes in solids, because large-scale MD simulations can generate steady plastic (or split elastic-plastic) waves with a rich nanostructure. Shock induced phase transformations (either solid-solid or solid-melt), multiple shocks (including ramp wave loading), unloading processes such as rarefaction shocks, spallation, ejection, and shock-induced chemistry are just a few of the phenomena for which MD simulations should be able to provide a great deal of insight. An intensive study has been systematically conducted for perfect single crystals [189, 190] with isolated defects [191, 192], and in polycrystalline materials [189, 193, 194]. The remarkable degree of qualitative and, in many cases, quantitative agreement between MD and experiment (especially laser driven shock compression where both length and time scales are close to commensurate with MD) has given increased confidence in the use of such simulations as both predictive and interpretative tools.

To investigate the microstructural mechanisms for the formation of 9R phase in

Al, we simulate the shock response of nanoscale columnar grains in Al using the plate spallation experiment [189]. Al samples are relaxed by energy minimization using quenching MD method, followed by equilibration using isothermal isobaric (NPT) ensemble at 300K and 0 GPa pressure for 50 ps. The time-step in NEMD simulations is chosen to be 0.2 fs to ensure numerical stability. The velocity-Verlet algorithm is adopted to solve the MD equations. The computational model for the plate impact experiment comprises two parts with the same material. One part is fixed (representing the impactor) and the other part is the target, i.e., the NC Al sample. Two dimensional periodic boundary conditions are used in the perpendicular directions. The target is shocked by ramming it at a speed of 1 km/s against the fixed impactor. The atomic interactions in Al are described by an accurate embedded atom method (EAM) potential developed by Winey et al. [195]. The validity of the EAM potential under strong shock conditions is confirmed by comparing Hugoniot curves (P-V and P-T curves) and the melting curve with experimental data [195].

To examine the influence of GB structures on the formation of 9R phases, we examined the shock response of NC Al with two different types of GBs. In the first case, NC Al contains four grains that have twin orientation and form Σ3 {112} ITBs. The columnar grain size is 15 nm and height is 75 nm. Topological analysis and microscopic characterization show that Σ3 {112} ITBs in FCC metals is consisted of a repeatable pattern involving three Shockley partial dislocations as one unit in three adjacent {111} atomic planes (see Supplementary Figure S6 (a1,a3)) [69, 179]. In comparison, we also shocked the columnar polycrystalline Al that contains Σ11 asymmetrical tilt grain

boundaries. The grain boundary plane is parallel to $(\bar{2}52)$ and $(\bar{4}14)$ in the neighboring grains. The grain boundary contains Shockley partial dislocations every seven {111} atomic planes (see Figure 4.10) [196]. Under shock at a speed of 1km/s, partial dislocations are nucleated at GBs and emitted into grains in two simulations (Fig 4.11). Most importantly, 9R phase is only observed in the columnar NC Al containing Σ3 {112} ITBs [Fig. 4.11(a3)]. The formation of the 9R phase is ascribed to the emission of pre-existing Shockley partial dislocations. Under high shear stresses, it is expected that one set of partial dislocations in Al can glide along one direction away from the compacted Σ3 {112} and the rest of partial dislocations that have screw components with opposite signs may glide towards the opposite direction if gliding force on them exceeds the Peierls force [49]. As a result, the 9R phase can propagate.

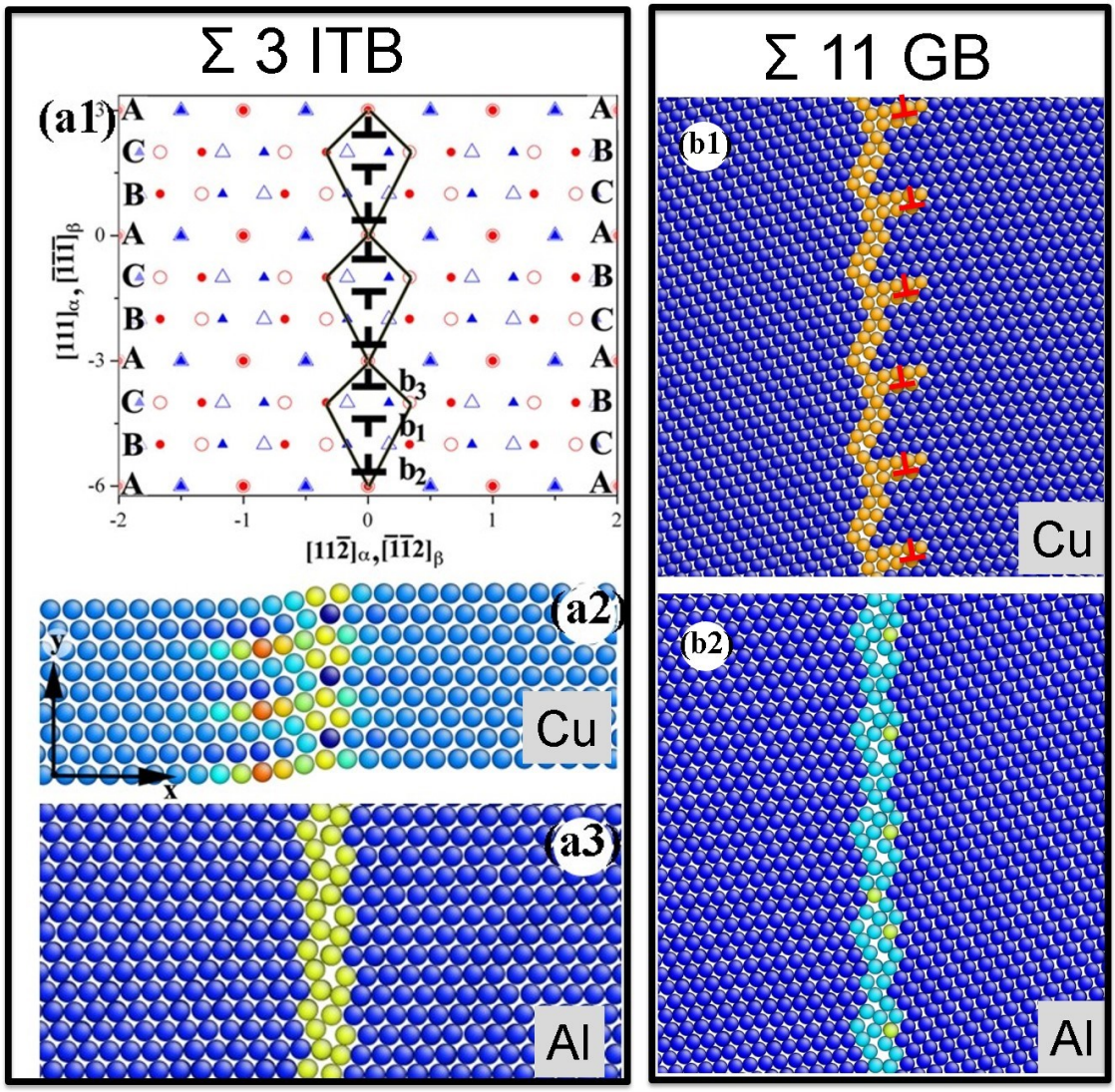

Fig. 4.10 Atomic structure of Σ3 ITB and Σ11 GB in low SFE Cu and high SFE Al. (a1) Dichromatic pattern of a Σ3 ITB, (a2) atomic structure of the Σ3 ITB in Cu, dissociation of one set of partials from ITB due to low SFE, (a3) Atomic structure of compacted Σ3 ITB in Al due to high SFE, and (b1) atomic structure of Σ11 GB in Cu, every seven {111} atomic planes contain one Shockley partial dislocations. All the partial dislocations are dissociated from the GB. (b2) Atomic structure of Σ11 GB in Al. All partial dislocations are constrained inside the GB due to the high SFE of Al.

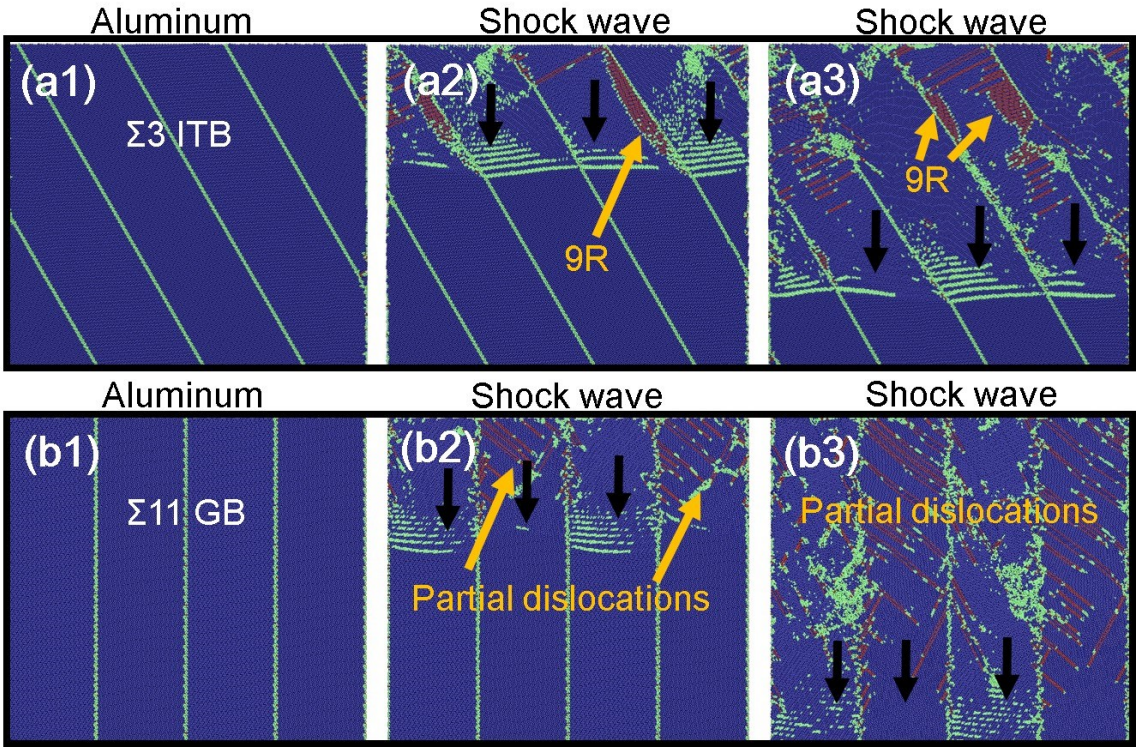

Figure 4.11 Molecular dynamic simulation of the shock induced partials activity in Σ11 GB and Σ3 ITB. (a1-a3) The snapshots of shock induced dissociation of partial dislocations from compacted Σ3 {112} ITB in Al. (a1) the Σ3 ITB with 15 nm domain size in Al film. (a2-a3) When the shock wave passes through the ITBs, the 9R phase forms due to the dissociation of ITBs by the emitting of partial dislocations from the ITBs. The red area bounded by the green lines is the 9R phase. (b1-b3) The snapshots of shock induced micro-twin and partials (nucleation and emission of partial dislocations from Σ11 GB). (b1) the Σ11 GB with 15 nm domain size in Al film. The GB contains Shockley partial dislocations every seven {111} atomic planes. (b2-b3) Partial dislocations are emitted from the GBs due to the shock wave.

Several factors may contribute to the stabilization of the 9R phase induced by the high-strain-rate deformation. Microscopy study (Fig. 4.5b) shows the formation of numerous Frank partials inside the 9R phase. The 9R phase regions may arise from the interactions among high-density Shockley partials activated on different slip systems

during projectile impact. These sessile Frank partials may act as barriers to block trailing partials and thus enhance the stability of the 9R phase.

Besides the pinning effect from sessile dislocations, the attraction between the leading and trailing partials decays with increasing separation distance. After the emission of leading partials, the impact induced stress wave dissipates quickly. Also, the trailing partials are less mobile than the leading partials, increasing the separation distance between leading and trailing partials. The attractive force between the leading and trailing partials may decrease rapidly to become insufficient to go over the barrier stress resulting from Peierls friction stress or Frank partials, leading to the pinning of the 9R phase in impacted UFG Al.

Although deformation twins and the 9R phase are frequently observed near the perforations, dislocation slips and the formation of dislocation networks during projectile impact are ubiquitous during plastic deformation of UFG Al [96]. Grains in the highly deformed region can reach dislocation density on the order of $10^{12}/cm^2$, similar to that in heavily cold worked metals. The high-density dislocation networks manifested by complex stress contours can effectively accommodate plastic deformation and facilitate energy dissipation during projectile impact. Our recent study also shows that the as-deposited UFG Al films contain a certain fraction of growth twins [180]. These growth twins interact with impact induced dislocations and act as pinning centers to store dislocations. The impact induced grain fragmentation could be related to the formation of dislocation cell walls in the grains or significant shear induced grain rotation and refinement.

IV.6 Conclusion

We report the first evidence for the formation of 9R phase in UFG Al subjected to high-strain-rate deformation. 9R phase arises from shock-induced rapid migration of leading partials from ITB seeds in as-deposited Al. The stability of the giant 9R phase is due to the pinning of trailing partials by abundant sessile dislocations in 9R phase. This study provides evidence for new deformation mechanisms of metals with high stacking fault energy under high strain rate. The methodology of using a novel microprojectile impact technique to impact TEM specimens opens a new avenue for high-throughput examination of high strain-rate impact induced damage and plasticity in a broad range of metallic materials.

CHAPTER V

THE MICROSTRUCTURE AND MECHANICAL STRENGTH OF NANOTWINNED ALUMINUM WITH DIFFERENT TEXTURES

V.1 Overview

Twin boundaries can enhance the strength and ductility of a variety of metallic materials with face centered cubic structures. However, twin boundaries are rare in Aluminum due to its high stacking fault energy (SFE). Deformation twins can form in Al via partials slip under high stress or at low temperatures. Previous studies show that the introduction of Ag seed layer is necessary to promote the formation of nanotwins in Al films. Here, we show that high-density twin boundaries can be introduced in Al films by tailoring the texture of films without any seed layer. Transmission Kikuchi diffraction and transmission electron microscopy studies on (111), (110) and (112) textured Al films show Al (112) films has the highest twin density. Furthermore, twin boundaries in Al appear to be stronger barriers to dislocations than conventional high angle grain boundaries.

V.2 Introduction

Twin boundaries (TBs) are low-Σ grain boundaries (GBs) with lower boundary energy compared to normal high-angle GBs [121]. TBs have been identified in a variety of materials, including TWIP (twinning induced plasticity) steel [197-200], shape memory

alloys [201-203], monolithic metals [52, 53, 58, 60, 166], ceramics [204-206], and certain biological materials[207]. The mechanical behavior of nanotwinned (nt) metals with high density growth twins have been intensively investigated [46, 53, 75, 146, 149, 154, 162]. High-density TBs not only provide high strength by blocking the propagation of dislocations [19, 54, 67, 124, 208-210], but also enable greater ductility [51, 53, 54, 211, 212]. Most prior studies focused on face-centered-cubic (fcc) metals with low-to-intermediate stacking fault energy (SFE) (less than 100 mJ/m^2) [19, 53, 58, 60, 109, 145, 156, 171]. In contrast, TBs are often prohibited in fcc metals with high SFE, such as Al (SFE of Al is ~ 160 mJ/m^2) [125, 213]. Although deformation twins have been observed in Al via molecular dynamics (MD) simulations [8, 93-95, 169, 214] and deformation at high stress or low temperatures [96, 107, 166], the formation of high-density growth twins in Al remains difficult.

Bufford et al. fabricated the twinned Al thin films by using a template method. A seed layer of {111} Ag was used as Ag with low SFE contains high-density nanotwin seeds [22, 120, 170, 215]. The subsequent deposition of Al on Ag promotes the propagation of twin seeds into Al because Al and Ag have identical lattice parameters. Using this technique, high-density incoherent twin boundaries (ITBs) can be introduced into Al films that have 1-2 μm in thickness. A similar strategy has been used to promote the propagation of growth twins into Ni in Ag/Ni multilayer system [216]. Two criteria are identified for the formation of growth twins using the template method: a template (or seed layer) containing twin seeds and, a coherent interface between the template and deposited layers [72]. A recent study shows that growth twins can be introduced in thin

polycrystalline Al films without any seed layer [180]. The fraction of twinned grains increases with increasing film thickness, and reaches a maximum (~ 8-9%) when film thickness is ~ 80 nm, beyond which the twin fraction rapidly diminishes. The film thickness dependent formation of growth twins in Al films is related to the nucleation and growth of twins, which are controlled by thermodynamics [180].

Prior studies also suggest that crystal orientation may play a role in the formation of growth twins. For instance, twin density is greater in epitaxial nt (111) Ag than that in (110) Ag [60].Narayanan et al. observed different twin morphology and stacking faults GaP with different texture deposited by chemical beam epitaxy [158]. Also high-density growth twins formed in highly textured (111) Cu/Ni multilayers, but not in (100) Cu/Ni multilayers [21].

However, it remains unknown if the texture of Al films can impact the formation of growth twins. In this study, we investigate the formation of growth twins in Al films with different textures, (111), (110) and (112). Extensive transmission Kikuchi diffraction - electron backscatter diffraction (TKD-EBSD) and transmission electron microscopy (TEM) studies have been performed systematically to investigate the formation of growth twins in Al. To our surprise, (112) Al has the greatest twin density and hardness. Comparison of hardness of UFG Al (films and bulk) shows that TBs (CTBs and ITBs) are stronger barriers to dislocations than conventional HAGBs. This study sheds light on the design of high-strength nt metals by tailoring the texture of crystals.

V.3 Experimental

Al thin films with different texture were deposited at room temperature using direct current magnetron sputtering technique under 2×10^{-3} torr Ar pressure. The base pressure of the vacuum chamber before depositions is ~ 5×10^{-8} torr. The purity of the Al target is 99.999%. Single crystal (111), (110), and (112) Si substrates were etched by HF to remove the oxide layers before the deposition. The deposition rate was kept at 0.5 nm/s and the Al film thicknesses (~ 600 nm) were measured by a Dektak 150 Veeco profilometer. X-ray diffraction (XRD) experiments were performed on a PANalytical X'Pert PRO Materials Research Diffractometer using Cu Kα radiation. For Al films grown on Si (111) and Si (110) substrates, the out-of-plane θ-2θ scans were performed. For the Al films deposited on Si (112) substrate, both the conventional out-of-plane θ-2θ scan and tilted scan (tilting chi to 19°) were performed.

The TKD-EBSD technique was used to characterize the crystal orientation of grains in the Al films [142-144]. The TKD experiments were performed on a Tescan FERA-3 with Schottky field emission electron source operated at 28 kV. The TKD data were processed by Oxford CHANNEL software. The typical scan area in this experiment using TKD-EBSD is 5 × 3 μm. Plan-view and cross-section TEM (XTEM) samples were prepared by mechanical grinding, dimpling, and low-energy ion milling. TEM specimens were examined by using an FEI Tecnai F20 ST transmission electron microscope operated at 200 kV. Mechanical properties were measured by nanoindentation technique using a Hysitron TI950 Trioindenter with a Berkovich diamond tip. The hardness was calculated

by using the Oliver-Pharr method [217] and a minimum of 35 indentations were performed on each specimen.

V.4 Result

V.4.1 Texture of Al films and twin density

XRD studies show that Al films deposited on Si (111) substrate exhibit (111) texture, whereas a weak (110) diffraction peak appears for the Al films grown on Si (110) substrate (shown in Fig. 5.1). Interestingly for Al films grown on Si (112) substrate, a regular θ-2θ scan up to 140^o yields no diffraction peak. After the chi angle was tilted to 15° prior to θ-2θ scan (shown schematically in the insert) strong Al (111) and Si (111) peaks emerged, indicating that the film on Si(112) possesses strong (112) texture. The texture of three Al films is examined in detail via EBSD pole figure analyses. The pole figures of {111}, {110}, {100}, and {112} poles for Al films with 3 different textures are compared in Fig. 5.2. The projection plane is the sample surface plane. The {111} pole figures for Al (111) film (Fig. 5.2a) confirm the formation of strong {111} texture. Moreover, the three strong spots (arising from matrix) and three alternating weak spots from twins are observed. The twins have a 60° in-plane (<111>) rotation compared with the orientation of the matrix. The {111} single crystal type of texture is also revealed in all other pole figures, including {110}, {100} and {112}. The pole figures of Al (112) (shown in Fig. 5.2c) resemble the pole figures of Al (111), indicating the epitaxial growth of films, except two major differences.

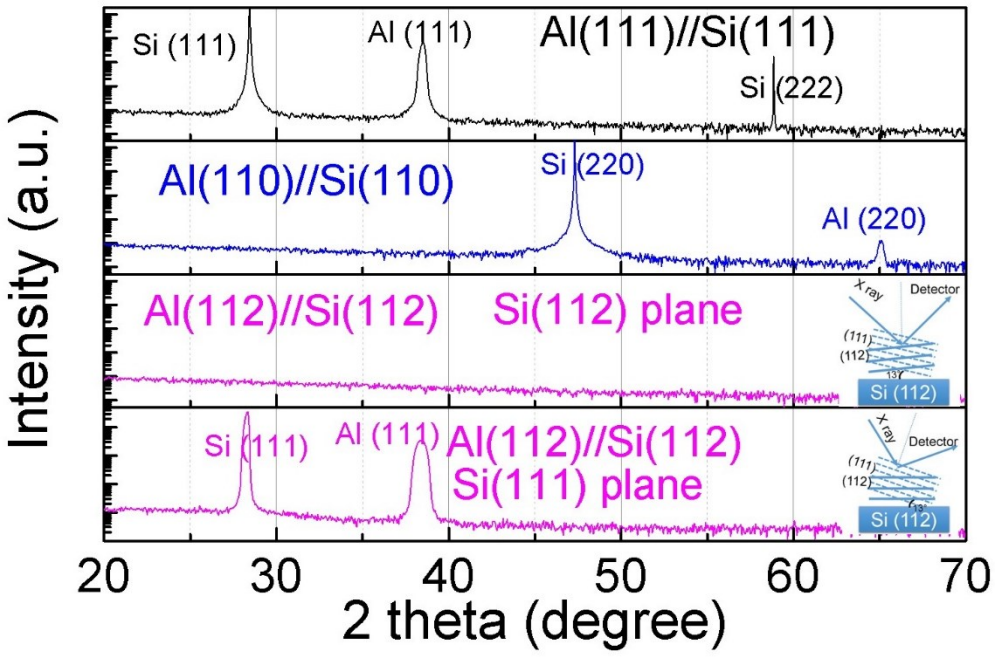

Figure 5.1 XRD profiles of Al thin films deposited on different single crystal Si substrates. Basically Al (111) grows epitaxially on Si (111) substrate, (110) textured Al forms on Si (110), and Al (112) grows epitaxially on Si (112) substrates. One of the XRD profiles for Al (112) shows no peak as the 2θ for the Al (422) is 137 degree, out of the range for the XRD diffractometer. The XRD profile for a slightly tilted Al (112) films (out-of-plane tilt by 19 degree) shows the single Al (111) peak, indicating the single crystal like nature of the films.

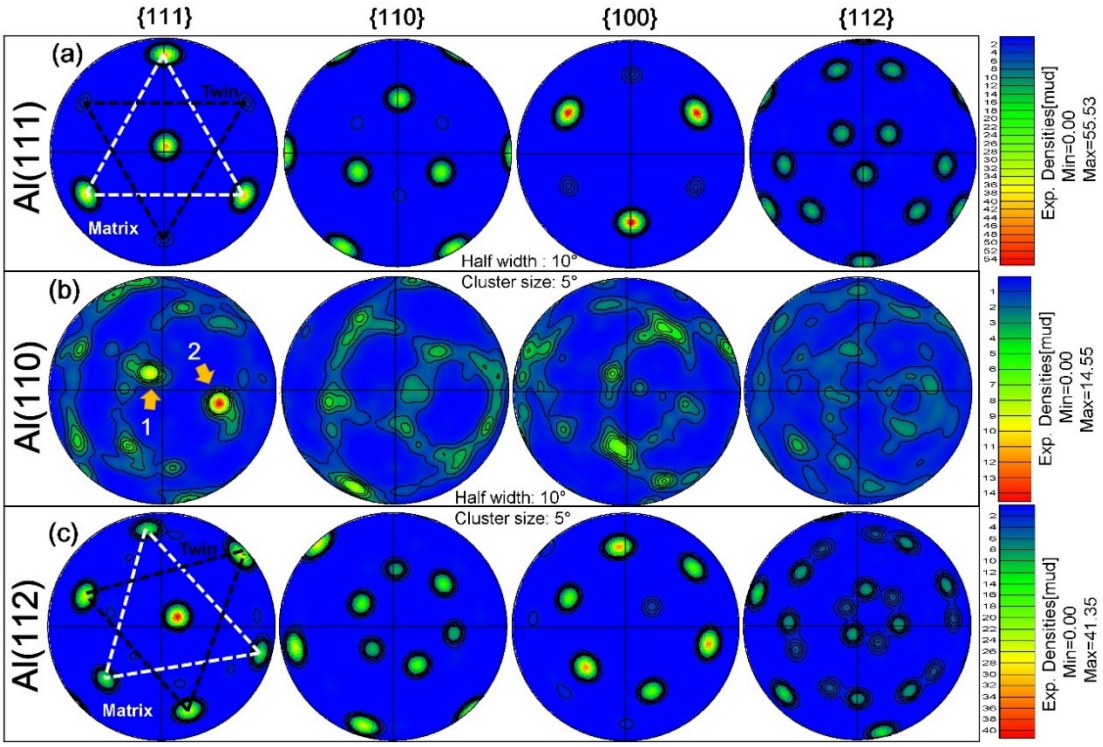

Figure 5.2 The pole figure of Al film deposited on three different Si substrates. The projected plane is the sample surface. (a) The pole figures of (111) epitaxial Al film deposited on Si (111) substrate along four different directions. The {111} pole figure shows a three fold symmetry with a weak set of extra 3 spots arising from the low density twin boundaries. (b) The pole figures of (110) textured Al thin film on Si (110) substrate. The film is textured, but not epitaxial. (c) The pole figures of (112) Al thin film on Si (112) substrate showing the formation of epitaxial Al (112) films. The six-fold symmetry of {111} pole figure suggests the formation of high-density growth twins.

First, the twin and matrix spots in Al (112) have nearly identical intensity, indicative of a large twin fraction in the Al (112) film. In addition, the center (111) plane is not perpendicular to the film surface in Al (112). Instead, one of the {112} planes (as revealed in the {112} pole figure) is close to the center of the pole figure, consistent with the (112) film growth direction. Compared with Al (111) and Al (112), the Al (110) film has a weak texture. The strong spot 1 in {111} pole figure comes from the [112] crystals (blue color in Fig. 5.3b1, and spot 2 arises from the [110] crystals (green color in Fig. 5.3b1), suggesting that [112] and [110] are the preferred crystal growth directions in Al (110) film. To acquire detailed crystallographic and microstructural information of these Al films, TKD-EBSD experiments were systematically performed. The orientation map (OM) of Al film on Si (111) from Z and Y directions are shown in Fig. 5.3a1 and Fig. 5.3a2. The Z direction is parallel to the surface normal direction, and the Y direction is an arbitrary direction perpendicular to Z and X directions in the films. The map color key follows the inverse pole figure convention as shown in Fig. 5.3d. All grains in the (111) Al film (on Si (111) substrate) have the [111] orientation along the Z direction and Σ3 [111] TBs are marked by yellow lines in Fig. 5.3a1. The TBs are clearly surrounding small twinned islands embedded in the matrix. The Y orientation map (OM Y) in Fig. 5.3a2 also confirms the existence of small islands in the matrix. Furthermore, the misorientation angle of grain boundary is predominantly 60°, consistent with the prevalence of TBs. As Σ3(111) CTBs and Σ3(112) ITBs are both affiliated with Σ3 [111] TBs. Therefore, CTBs and ITBs in Fig. 5.3a2 cannot be differentiated. According to the crystallographic orientation of ITBs and CTBs illustrated in Fig. 5.4, the [111] rotation axis of CTBs is

perpendicular to the CTBs, but parallel to ITBs. Using this strategy it is now straightforward to distinguish CTBs and ITBs by calculating the angle between boundary and boundary rotation axis. For instance, nearly all the boundaries in Fig. 5.3a3 display blue colors. Based on the color map key listed in Fig 5.3f, the rotation axis of boundaries (RAB) is parallel to the Z direction, and thus these TBs are mostly ITBs. In the Al film grown on Si (110) substrate, {110} texture is predominant although grains with other orientations are also visible as shown in Fig. 5.3b1. Interestingly TBs in the Al (110) film labeled by red lines typically exist between [110] grains (green color) and [221] grains (in blue). Although ~ 30% of grains has TBs as shown Fig. 5.3b2, high angle grain boundaries (HAGBs) prevail in the Al (110) film. Fig. 3b3 shows that more than 70% of the TBs are CTBs.

EBSD pattern of Al (112) films is quite different from those in Al (111) and Al (110). A noteworthy characteristic is the long curved TBs (labeled in red) formed primarily between <112> (purple color) and <212> (blue) crystals as shown in Fig. 5.3c1. In addition to these two major orientations, small clusters of <102> crystals in yellow color were discovered in the film and the <102> grains are comprised of multiple subgrains separated by low angle GBs (Fig. 5.3c2). Although these <102> crystals do not directly contribute to the formation of TBs, they effectively divide the islands of <112> and <212> islands, so that their grain sizes are not as large as <111> crystals observed in Al (111) (Fig. 5.3a1). Furthermore Fig. 5.3c3 shows that ITBs exists between <112> and <212> islands, whereas CTBs primarily form within the <112> grains.

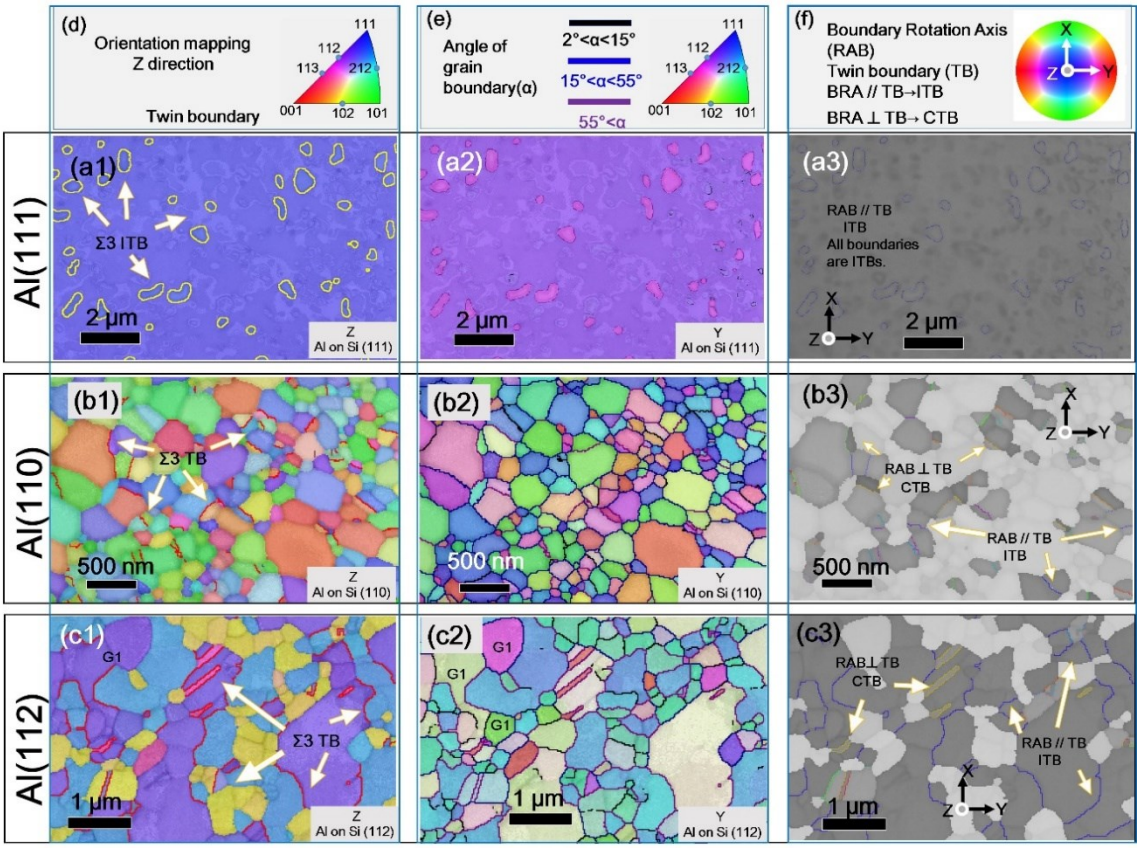

Figure 5.3 Electron backscattered diffraction (EBSD) micrograph of the as-deposited (111) Al thin film on Si (111) substrate. (a1) The crystal orientation map (OM) along the sample surface normal (Z) direction. The yellow lines indicate the Σ3 incoherent twin boundaries (ITBs). The small twin islands are embedded in the matrix. (b1) The red lines in OM Y indicate the misorientation angle of GBs in Al (111). (c1) The boundary rotation axis map reveals the method to differentiate ITBs from coherent twin boundaries (CTBs). For ITBs, the boundary rotation axis (RAB) // TB, and for CTBs, RAB ⊥ TBs. (a2) The Al (110) film OM along the Z direction shows red lines arising from the Σ3 twin boundary. (b2) The lines in OM along Y direction indicate the misorientation angle of GBs. (c2) The boundary rotation axis map reveals the co-existance of ITBs and CTBs. (a3) The as-deposited (112) Al OM Z shows abundant red lines, due to the formation of Σ3 twin boundary. (b3) The lines in OM Y outline the misorientation angle of GBs. (c3) The boundary rotation axis map reveals the dominating existance of the ITBs and a small population of CTBs. (d-e) The orientaiton information can be deciphered using the inserted inverse pole figure (IPF) in the top row. (f) The color key to visualize the boundary rotation axis for differentiation of ITBs from CTBs.

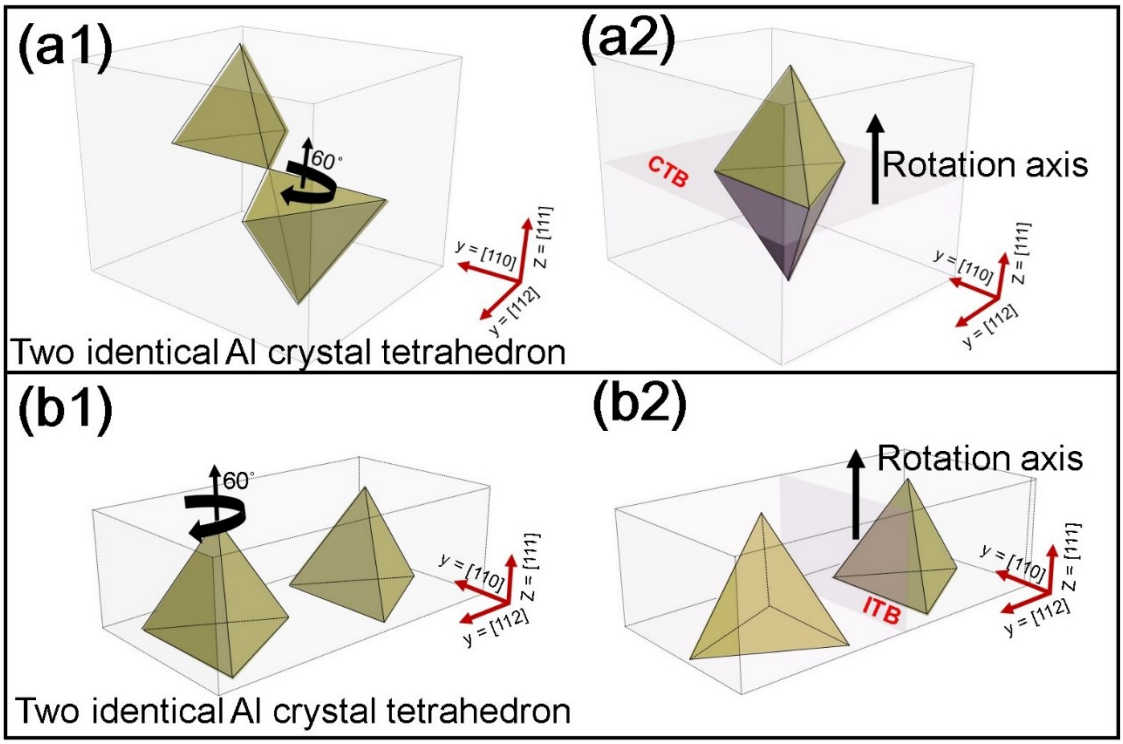

Fig. 5.4 The schematic of orientation relationship between the twin boundary and crystal rotation axis. (a1) Two identical Al crystal tetrahedron. (a2) To form a coherent twin boundary (CTB) in fcc metals, the lower crystal rotates 60° along <111> direction. The twin boundary (CTB) is perpendicular to the rotation axis. (b1) Two identical Al crystal tetrahedron. (b2) same rotation for the crystal can form the incoherent twin boundary (ITB), and the rotation axis is parallel to the ITB.

To characterize the twin density in Al films with three different textures, boundary density (defined as the length of boundaries per unit area) is used. As ITBs and CTBs can be differentiated, the density of CTBs, ITBs, and overall boundary are compared for all 3 orientations in Table 1. Al (111) appears to have primarily ITBs, and TBs exceeds 90% of the overall boundary density. However, it is worth mentioning the epitaxial Al (111) films have small isolated twin islands and the boundary density is much lower than that of other orientations In contrast, Al (110) has much lower twin density (only 10%) with the highest

boundary density among three orientations, and a majority of boundaries are conventional HAGBs. Al (112) has nearly 30% TBs, and the density of ITBs is twice that of CTBs.

Crystal orientation	Average Grain size (nm)	Boundary density (total) (μm^{-1})	Twin boundary density(μm^{-1})		Twin boundary /total boundary ratio (%)	Hardness (GPa)
			CTB	ITB		
Al(111)	400	0.61	0	0.57	93	0.74±0.1
Al(110)	160	8.97	0.71	0.22	10	0.88±0.1
Al(112)	340	3.49	0.35	0.69	30	1.03±0.1

Table 1. The boundary density of Al film on different silicon substrate. The boundary density is defined as the total length of the boundary divided by the area. All the boundary lengths are calculated from the EBSD data.

V.4.2 Microstructure characterization of thin films by TEM

The plan-view TEM micrographs of Al (111) film in Fig. 4a show excessive Moiré fringes along GBs. The inserted selected area diffraction (SAD) pattern confirms the formation of epitaxial (111) film. The mosaic structure inside the film suggests the existence of dislocation arrays formed during the island coalescing process, commonly observed in epitaxial films[218, 219]. Figure 4b shows the polycrystalline Al film grown on Si (110). The Al film deposited on Si (112) has (112) epitaxial structure (Fig. 5.5c). The grain size distributions of three Al films are shown in Fig. 5.5. The average grain size,

d_{ave}, of Al (111) is 400 nm, followed by 350 nm in Al (112), and 160 nm in Al(110) film. Cross-section TEM (XTEM) experiments were also performed for all three Al films. In general, the Al (111) film on Si(111) substrate has giant grain sizes, and black strips (Fig. 5.6a1) arise from either high-density threading dislocations (as revealed by SADs from location 1) or occasionally ITBs as shown by SAD of a stripe in region 2 marked by the white circles. HRTEM (Fig. 5.6a2) of box a2 (in Fig. 5.6a1) shows classical ITBs, with one Shockley partial on each {111} plane in the three layer periodically stacking. Al (110) film has polycrystalline nature and TBs are occasionally identified as confirmed by the SAD in Fig. 5.6b1. Two parallel CTBs are observed: one of the CTBs stems from the interface between Si/Al interface, and the other one appears to nucleate from column grain boundary. HRTEM micrograph in Fig. 5.6b2 shows CTB nucleated from the grain boundary.

For the Al (112) film grown on Si (112), CTBs and ITBs are observed in adjacent column as shown in Fig. 5.6c1. The narrow long inclined CTB labelled by an white arrow stems from the Si/Al interface and reaches the film surface. An ITB is identified at location 3, as confirmed by SAD. Another inclined CTB is shown in Fig. 5.6c2. XTEM studies show that most CTBs are located inside the domains while the ITBs are at domain boundaries, which correlates well with the EBSD data. Another noticeable feature of the Al (112) film is the 4° tilt between Al(112) and Si(112), as shown by HRTEM micrograph in Fig. 5.6c3. This observation is consistent with the {112} pole figure analysis of the Al (112) film (Fig. 5.2c). The nanoindentation studies on the all three films (listed in Table 1) show that Al (112) film has the highest hardness.

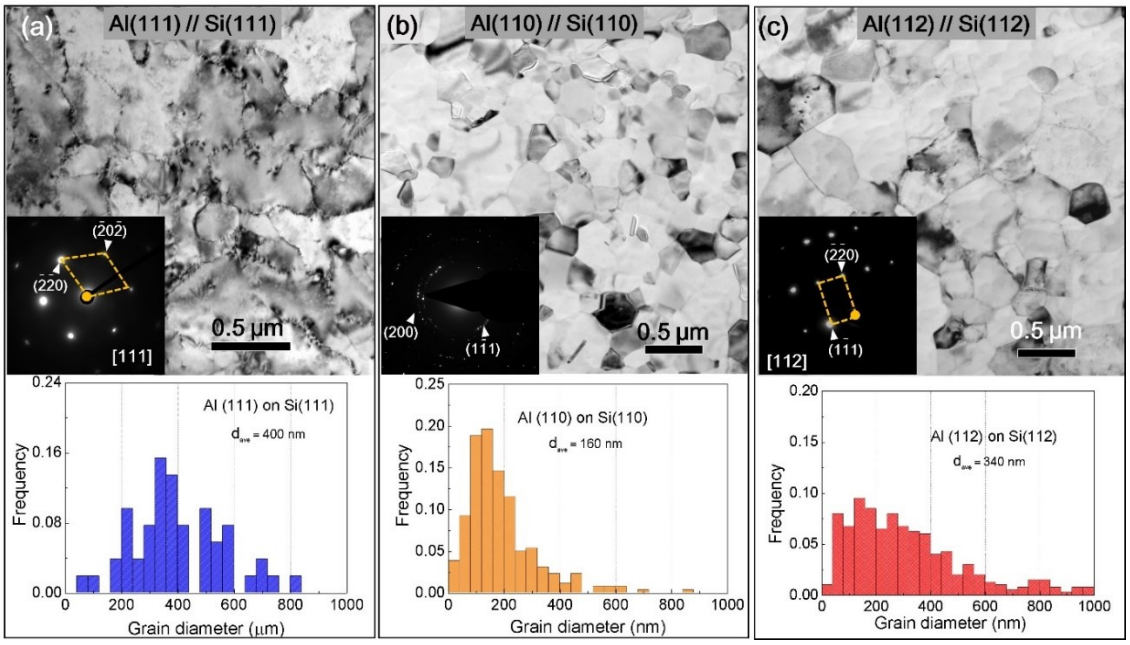

Figure 5.5 The plan-view transmission electron microscopy (TEM) micrographs of Al thin films with different orientations and grain size distribution. (a) The Al films deposited on Si (111) substrate appear to have large grains and the inseted selected area diffraction (SAD) pattern shows the formation of (111) epitaxial Al films. (b) Polycrystalline (110) textured Al films form on Si (110) substrates. (c) Epitaxial Al (112) films are deposited on Si (112) substrates.

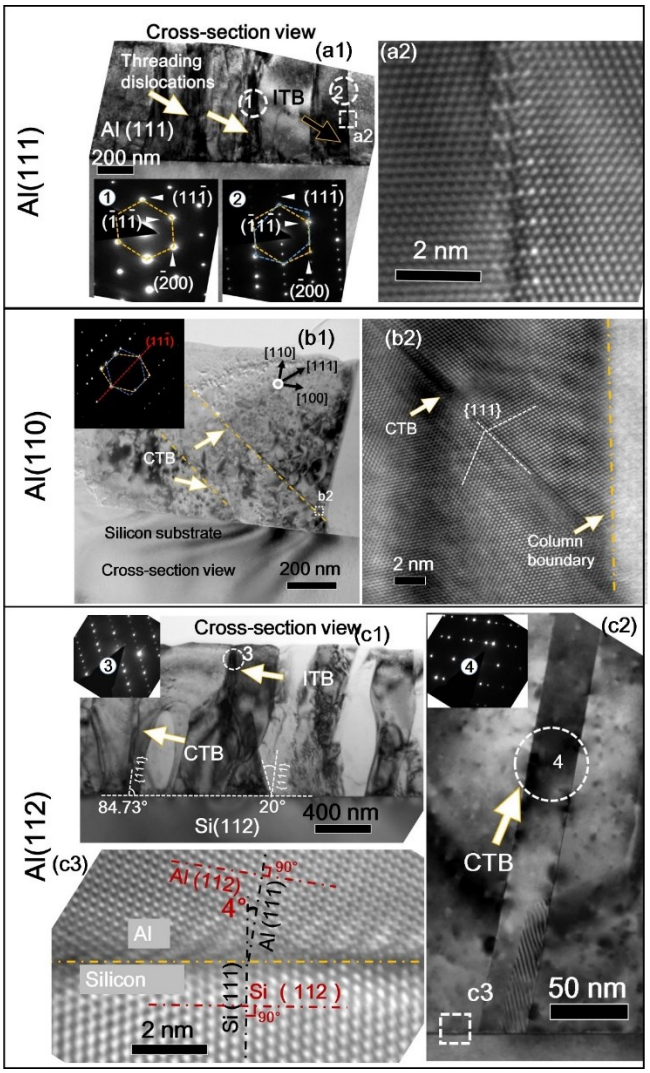

Figure 5.6 The cross-section TEM (XTEM) micrographs of Al thin film deposited on Si substrate. (a) Al (111) thin film deposited on Si (111) substrate examined along Al <110> zone axis. (a1) Two SAD patterns were taken at location 1 and 2 marked by white circles. The inserted SAD patterns show the formation of (111) single crystal at location 1, and the formation of epitaxial twins at location 2. (a2) A high-resolution TEM (HRTEM) micrograph showing a sharp ITB located in the white box c in Fig. 6a1. (b) Al (110) thin film deposited on Si (110) substrate. (b1) The yellow dash-dot lines delineate two inclined CTBs as confirmed by the inserted SAD pattern. (b2) An HRTEM micrograph shows the formation of a CTB from the white box b2 in Fig. 6b1. (c) (112) Al thin film deposited on Si (112) substrate. (c1) The XTEM image shows the evdience of CTB and ITB. The diffraction pattern taken at location 3 confirms the formation of an ITB. (c2) The TEM image shows the inclined CTB inside one column. (c3) The HRTEM micrograph shows the interface between Al and Si substrate. The 4° misorientation angle exists between the Si [112] and Al [112] orientation.

V.5 Discussion

V.5.1 Growth twin formation mechanisms

Growth twins are in general prohibited in metals with high SFE due to the high-energy barrier for twin formation. However, there are scattered evidence showing formation of growth twins in Al with high SFE by physical vapor deposition [180, 220, 221]. Prior studies show [180] that the probability of forming parallel and incline growth twins is different in Al. As a starting point of the discussion, it is necessary to revisit the formation mechanisms of growth twin in metal film. Generally speaking, there are two major twin formation mechanisms during the vapor to solid phase transformation. One is the consecutive fault stacking during the growth [72, 222]. It has been shown [71] that a high deposition rate may increase the density of growth twins in sputtered (111) Cu. And this phenomenon has been explained using a thermodynamic model [19]. The other formation mechanism is the impingement of two islands with twin orientation during the crystal growth [218, 223]. During the islands' coalescence in film growth process, low energy TBs may form instead of the HAGB to minimize the system energy. Additionally Ino et al. [224] have observed particles with multiple TBs using thermal evaporation. Similarity among these mechanisms is that the crystal growth orientation may affect the twin formation ability. For example, the multi-twin particle formation model [225] works well for [111] or [100] orientation. Bufford et al. [60] observed the low twin density in Ag (110) compared to epitaxial nt Al (111). In the following section, the influence of crystal orientation on twin formation mechanisms will be discussed.

We first examine the formation of growth twins in Al (111) film with low density ITBs along the domain boundaries shown schematically in Fig. 5.7a1. Similar structures in Al have also been revealed in literatures [120, 149]. Based on the pole figure analysis, the twin domains have a 60° in-plane rotation along the [111] direction in comparison to matrix. Since the <111> axis contains a three-fold axis of symmetry, 120° in-plane rotation will result in the same crystal arrangement. In epitaxial Al (111), nuclei have only two different crystal orientations, the matrix and twin orientation (with 60 in-plane rotation). Due to its high SFE and the similarity between twin and matrix orientation, the growth of twinned islands in Al (111) is very difficult. For instance, although TBs account for more than 90% of the grain boundaries in Al (111), the overall boundary density is much lower than that in Al (110) and Al (112) (Table 1). Also, the average grain size in Al (111) is rather large, ~ 400 nm. Conversely, in low SFE Ag films, nearly 50% of twin domains can form in Ag (111) thin film. It is worth mentioning that smaller domain size and high density ITBs can form in Al by using Ag (111) seed layer [120]. Furthermore, the ITB Al columns grown on Ag have smaller domain size, ~ 200 nm, similar to the dimension of columnar grains in the Ag seed layer.

Next, the Al (110) film deposited on Si (110) has fine grain size (~160 nm) with weak [110] texture. Although the boundary density is 8.97/μm, much greater than that in Al (111), TBs account for merely 10% of the boundaries. Also based on the EBSD analyses, more than 70% of TBs are CTBs. Among the CTBs, half of them are in [110] matrix and the rest are in [212] matrix. Fig. 5.7b1 shows the crystal orientation of two type of twin structures in Al (110) films. The CTB tilting angle can be calculated based on the

pole figure in Fig. 5.7b3, where spot one is the TB for type one and the spot two is the TB for type two twin. As revealed by XTEM studies, TBs may form either at the Al/Si interface, due to the impingement of two twin nuclei, or nucleated from the domain boundary. Similar twin formation mechanisms have been identified in ultra-thin polycrystalline Al film [180].

Finally, we evaluate the formation of high-density growth twins in Al (112) films. Al (112) has the highest twin density among three orientations investigated here. Nearly all ITBs form between the [112] and [212] crystals and CTBs form within [112] grains shown in Fig. 5.2a3. Figure 5.7c1 shows the schematic of the ITB in the Al (112) film which has nearly identical configuration comparing to ITBs in Al (111). A major difference between the two schematics (Fig. 5.7c1 and Fig. 5.7a1 examined along Al <110> zone axis) is that the entire crystal of Al (112) appears to have a 15° rotation comparing to that of Al (111), consistent with the {111} pole figure analysis (comparing Fig. 5.2a and Fig. 5.2c). The forgoing analogy is a bit simplified. In reality, the formation of growth twins in Al (112) is more complicated. Based on the crystallography, the atomic planes parallel to the Si (112) plane are either Al (335) or Al (535). Note that these two orientation are very similar to the EBSD analyses, showing the formation of TBs between (112) and (212) islands (Fig. 3a3). The (335) / (535) orientations are unique as two types of boundaries can form between these two crystals, namely (112) ITBs with orientation nearly parallel to the film normal direction (rotated by 4° from substrate normal direction), and (111) CTBs that is rotated by 19° from the Si (112) surface (as shown in Fig. 5.7c1).

Although both Al (111) and Al (112) form growth twins, the TB density in Al (112) is much greater. As shown schematically in Fig. 5.7a2, only isolated twin islands exist in Al. This is a natural consequence of high SFE in Al. The matrix would prefer to "wipe out" twin seeds to minimize system energy during the island coalescence regime in film growth process. In contrast, as illustrated in the schematic in Fig. 5.7c2, high-density ITBs can form between (335) and (535) islands. None of the two orientations can take the predominant role, because of the existence of a third crystal orientation, Al (102). The cluster of these crystals form a natural barrier to stall the ITB annihilation process during island coalescence regime, prohibiting the excessive growth of either (335) or (535) variants. When the film enters steady column growth regime, the ITB annihilation process through island rotation triggered by the partial dislocation slip is terminated due to the constraint from the adjacent (102) columnar grains. Thus, (102) crystals, though not directly contribute to the formation of twins, can curtail abnormal grain growth of either variants, thus promote indirectly the formation of high-density growth twins.

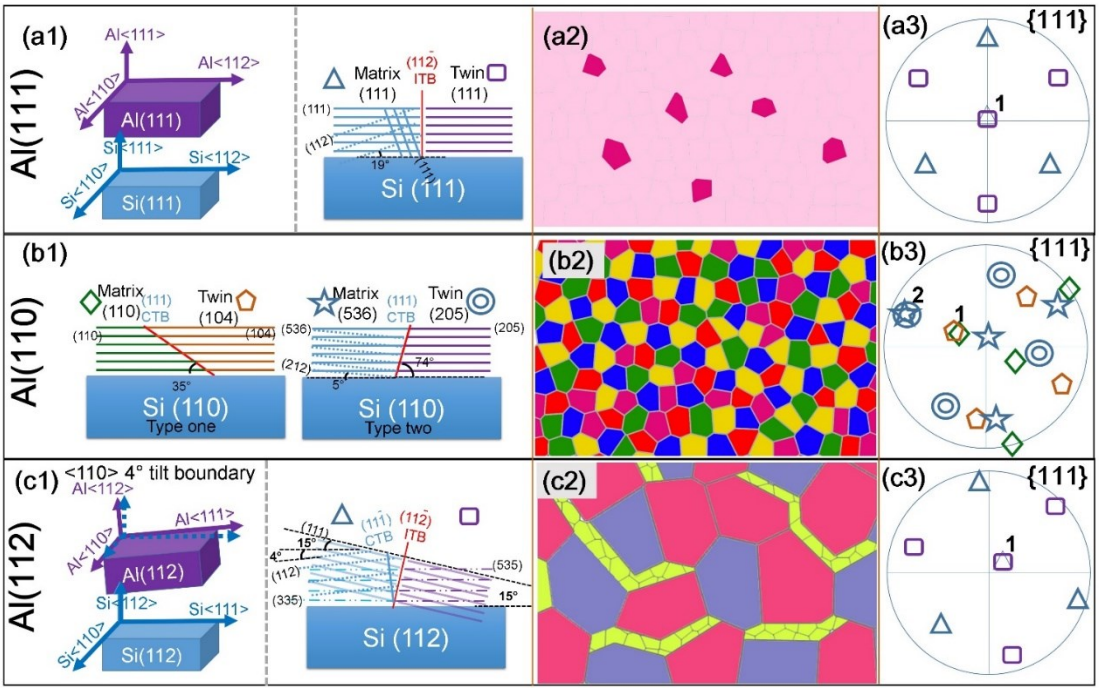

Figure 5.7 Orientation relationship of twin structures in Al films. (a1) The schematic of crystal orientation of twinned columns for (111) Al on Si (111). The vertical ITB has been marked as red line and the angle between (112) and (111) planes is 19°. (a2) The schematic of the grain distribution in Al(111) film. The twin columns are isloated islands in the matrix. (a3) The pole figure of twinned crystals, the triangular shape represent the {111} planes of matrix, whereas the square symbols arise from the {111} planes of twins. (b1) The schematic of crystal orientations of major twinned columns in Al (110). Type one: a CTB forms between two crystals with normal directions of [110] and [104]. The angle between CTB and substrate surface is 35°. Type two: a CTB forms between the two crystals with [536] and [205] orientation. The (536) palne is nearly parallel to (212) plane (with a small 5° tilt). (b2)The schematic of grain distribution. (b3) The pole figure for two sets of twins. For the type one twin, the CTB is at spot 1, where twin and matrix share the same (111) plane, and CTB of type two is at spot 2. (c1) The schematic of crystal orientation of twinned columns in Al(112) on Si (112), the normal direction of matrix crystal is [335] and the normal direciton of the twin crystal is [535]. The crystal orientation of twin in Al(112) is similar to that of Al(111) shown in Fig. 6a1, except that the entire crystal has been tilted 15° compared with the crystal strucutre ofAl(111) in Fig. 6a1. (c2) The schematic of the grain distribution, all the twinned grains were marked by blue and red color. The dominant twinned crystals are surrounded by small grains (yellow) with [102] orientation. (c3) The pole figure of {111} planes for twin and matrix.

The formation of growth twins in bicrystals have been observed before in Ag[60], Au[226], Al [227, 228]and $NiSi_2$ [229]. The concept developed here may be generally applicable for the formation of growth twins in fcc metals, especially those with high SFE. Basically, two major crystal variants with twin orientation are necessary; and furthermore small cluster of grains with different orientation is beneficial to impede the abnormal growth of one variant of twin structures.

V.5.2 The influence of TBs on strengthening

A 3D plot is shown in Fig. 5.8a to visualize the influence of grain size and TB fraction on strengthening. Besides the three pure Al films deposited in this study, the nt Al film with Ag seed layer [120, 149] is also added for comparison. Although Al (111) on Ag seed layer and Al (111) on Si have similar high TB fraction, Al (111) on Si (111) has low hardness, because the grain size of the film is very large ~ 400 nm, comparing to 200 nm of Al (111) on Ag seed layer. It is worth mentioning that the Al (110) has the smallest grain size, ~ 160 nm, among all films, but its hardness is lower than Al (111) on Ag seed layer and Al (112), as the TB fraction is the lowest in the Al (110) films with randomly oriented HAGBs. Al (112) has larger grain size than Al (110), but has a higher TB density, leading to its higher hardness, exceeding 1 GPa. These comparisons, though somewhat scattered, suggest that ITBs are stronger barriers for the dislocation slip in Al film than conventional HAGBs.

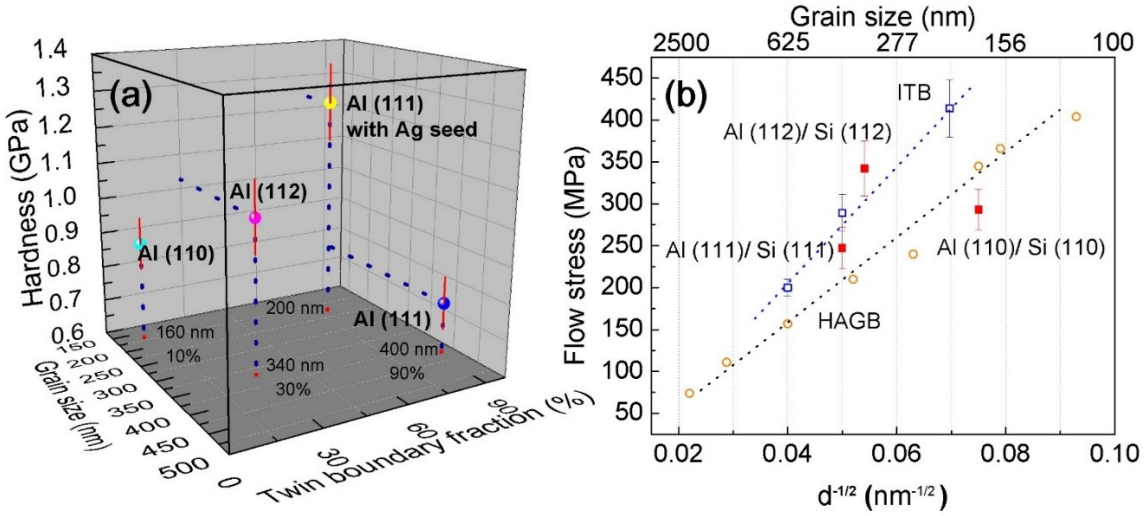

Figure 5.8 (a) The evolution of film hardness with grain size or twin boundary fraction. Twin boundary fraction are defined as the ratio betweentwin boundary length and total boundary length. (b) The Hall-Petch plot for several Al films [74,75] showing the influence of GB and TB on flow stress (H/2.7) of Al films. The red squres are from the Al film with high-density ITBs (this study), whereas the orange open circles show the Al with conventional high angle GBs (HAGBs). The flow stress of twinned Al on Si (112) and Si(111) are located along the same red dotted line. The flow stress of the (110) Al films with little twins (deposited on Si (110)) follows the Hall-petch slope of Al with conventinal HAGBs. The Hall-Petch slope for twinned Al is greater than that of Al with conventional HAGBs.

A Hall-Petch plot of flow stress (hardness/2.7) vs. average grain size is shown in Fig. 5.8b The blue data indicates the high density ITBs in Al films deposited on Ag seed layer, dark green data are obtained from polycrystalline Al with different grain size processed by equal channel angular pressing [230, 231]. Red data are from this study. Two slopes are obtained by fitting these data. The Hall-Petch slope of Al with a significant fraction of CTBs or ITBs is greater than that of HAGBs, indicating that ITBs may be

stronger barriers to the transmission of dislocations than conventional HAGBs in the Al. In-situ TEM nanoindentation experiment coupled with MD simulations also suggest that ITBs are strong barriers to the transmission of dislocations, as ITBs can not dissociate during deformation, whereas ITBs dissociate in Cu with low SFE [149]. The peak strength of Al with two types of boundaries can be estimated by using the following formula [19].

$$K_{HP} = \sqrt{\tau^* \mu b / [\pi(1-v)]} \qquad \text{Equation 27}$$

where τ^* is the interface barrier strength, $\boldsymbol{b}$ is the magnitude of Burgers vector, μ is the shear modulus, and v is the Poisson ratio. The K_{HP} of ITB and HAGB of Al is ~2.5 GPa•$\sqrt{nm}$ and 1.6 GPa•$\sqrt{nm}$ based on the fitting of data from Fig. 5.8b. For AL, given b = 0.286 nm, μ = 26 GPa, ν = 0.33, τ^*_{ITB} is estimated to be 1.76 GPa and τ^*_{HAGB} = 0.73 GPa. The maximum flow stress for Al with of ITB and HAGB are 5.3 GPa and 2.2 GPa by applying the Taylor factor of 3. Thus the maximum strength of Al with ITBs could be twice as strong as that of Al with conventional HAGBs. This analysis may serve as an upper bound estimation of peak strength for nanocrystalline and nanotwinned Al, which requires further experimental validation.

V.6 Conclusion

The influence of film texture on the formation of TBs is investigated in Al (111), (110) and (112) textured films. Epitaxial Al (111) has only two {111} twin variants, matrix

and twins, resulting in small isolated twin islands due to abnormal grain growth. Epitaxial Al (112) film has the highest density of ITBs, because the twin variants (335) and (535) are separated by Al (102) islands, promoting the formation of ITBs. The smaller domain size can thus be achieved by introducing HAGBs into the twinned bicrystal structure to inhibit the abnormal growth of single variant. These in-depth microstructure analyses supported by extensive TKD and TEM analysis provide an alternative way to promote the formation of highly twinned Al in addition to the recently reported template technique to refine the domain size,. Nanoindentation studies show that TBs are stronger barriers to block the transmission of dislocations, and hold the promise to deliver high strength nanotwinned Al.

CHAPTER VI

MECHANICAL BEHAVIOR AND STRENGTHENING MECHANISMS OF NANOTWINNED ALUMINUM ALLOY

VI.1 Introduction

Light-weight high-strength structural materials have been intensively studied due to the increasing requirement to improve fuel efficiency especially for automotive and transportation industry. Aluminum (ρ=2.7 g/cm^{-3}) and magnesium (ρ=1.7 g/cm^{-3}) are among the lightest monolithic metals and inevitably attract significant interest in research community. However, both Al and Mg have low modulus and melting point, and are known to have very low yield strength. Various solutes have been doped into the Al and Mg matrix to enhance their strength, formability and ductility. Numerous class of Aluminum and Mg alloys have been developed extensively and advanced Al and Mg alloys enable a board range of industrial applications [232, 233]. But higher strength and better ductility remain necessary for these alloys for more challenging requirement for various applications.

Various strategies have been developed to strengthen Al alloys, including grain boundary and solid solution strengthening, work hardening, and precipitate strengthening. A conventional way to strengthen 7××× series Al alloys is precipitation hardening, which has been widely used for aerospace industry [234]. The extremely fine and homogeneous precipitates can block the slip of the dislocations and strengthen the materials [235]. To achieve the optimum precipitate strengthening condition, various heat treatment

procedures have been developed [236-238]. Another conventional strengthening mechanism for Al alloy is to use solid solution, which increases the friction stress for dislocation slip. Solid solution can also stabilize small grains and change stacking fault energy [126, 239-244]. Thus, solid solution strengthening is often tied to grain boundary strengthening.

High strength nanocrystalline (nc) metals have been widely explored in the past decades and nanostructures can be achived by using ball milling, equal channel angular pressing (ECAP), and other severe plastic deformation (SPD) techniques [240, 245-247]. Combined with precipitation hardening, Zhao et al. reported an ultra-high tensile strength of 720 MPa in ultra-fine grained (UFG) 7075 Al alloys after ECAP, whereas the tensile strength of commercial 7075 Al is 570 MPa. Moreover, Koch et al. [240] also successfully synthesized 26 nm Al-5%Mg alloy with 740 MPa tensile strength by in situ consolidation. Even higher tensile strength (1 GPa) has been reported by Liddicoat et al. [246] for 7075 alloys. Besides these SPD techniques, electrodeposition and physical vapor deposition techniques can also fabricate nc alloys [14, 248]. Although nanograins can lead to high strength, they also degrade the ductility [249-251]. To achieve high strength and good ductility, twin boundary (TB) has been identified to be a good candidate [46, 53, 162]. However, the high stacking fault energy (SFE) of Al makes it difficult to introduce high-density twins.

Recently Al with high-density growth twins has been fabricated by introducing nt Ag buffer layers [22, 120, 170] by the magnetron sputtering technique. The epitaxial growth Al on Ag seed layer permits the extension of vertical twin structure (mostly

incoherent twin boundaries-ITBs) into Al. A systematic study on different metallic multilayer systems results in two criteria to allow the formation of twins in high SFE metals by using the seed layers [72]. First, the low SFE metals with high-density twins act as buffer layers to provide twinned seeds; and the second criterion is the coherency at the interface between the low SFE seed layer and high SFE metals to make sure that the twin structure can be introduced through layer interfaces successfully.

In this article, we use a simple method to introduce twins into AlMg films by DC magnetron sputtering with a low SFE metallic seed layer. By adding more Mg solute, the strength of the nt AlMg films raisess significantly due to the solid-solution and grain boundary strengthening. *In-situ* micropillar compression technique is also employed to obtain stress-strain behaviors, and the flow stress correlates well with the nanoindentation hardness measurement. Furthermore compression studies show nt AlMg has excellent strain hardening capability. Post-compression TEM analysis on the deformed pillars reveal distinct deformation morphology. The twin formation mechanisms, including nucleation and formation of broad 9R phase, are discussed.

VI.2 Experimental

The AlMg thin films were fabricated using DC magnetron sputtering at room temperature on Si substrates. The substrates were etched using HF to remove the oxidized layer on the surface. High purity (99.99%) Al and Mg targets were used as the deposition sources. The base pressure before the deposition was ~ 6×10^{-8} torr, and ultra-high purity Ar gas was injected into the chamber to generate the plasma under 2×10^{-3} torr. The AlMg alloy with different Mg composition (1, 5, and 10 at.%) were deposited by tuning the

deposition power. To stimulate the growth of twin structure, an 80 nm thick Ag seed layer was deposited [120, 149]. The normal out-of-plane θ-2θ scan and pole figure studies were performed on all samples using PANalytical X'pert Pro material research diffractometer with Cu-K_α source. The chemical analysis was measured by energy dispersive spectroscopy (EDS) in a Tescan LYRA-3 model SEM with schottky field emission electron source. The TEM sample was prepared by mechanical grinding and fine polishing to ~ 40 μm in thickness, followed by dimpling and low-energy ion milling to get a thin area for plan-view and cross section TEM specimens. The microstructure of specimens were characterized by an FEI Tecnai F20 ST operated at 200 kV. The hardness was tested by instrumented nanoindentation using an FIscherscope HM200XYp nanoindenter with a Vickers indenter tip. A minimum of 20 indentations were employed for one sample at each indentation depth. Pillars were fabricated using the focus ion beam technique in FEI Quanta 3D dual-beam SEM. The diameter of the pillars is 500 nm, and the height of the pillars is 1000 nm. The taping angle is less than 2 degree to ensure reliable data analyses for the uniaxial compression tests. The *in-situ* pillar compression test has been performed by using a Hysitron PI 87XR Picoindenter inside the FEI Quanta 3D FEG SEM microscope. The force-displacement data were captured by a piezoelectric actuator on the high-load capacitive transducer. The average drift rate is 0.3 nm/s during the in-situ test. The noise of the force and displacement is less than 8 μN and 1 nm. The in-situ compression test has been done in 20 s to minimize the thermal drift.

VI.3 Results

VI.3.1 Texture of AlMg films

XRD profiles in Figure 6.1 show that $Al_{99}Mg_1$, $Al_{95}Mg_5$, and $Al_{90}Mg_{10}$ films have the same Al (111) texture. To explore the crystal orientation of the films in detail, x-ray pole figure analyses have been performed on all the films. As shown in figure 6.2, the (111) pole figures indicate the epitaxial structure for all the films together with high-density twins as evidenced by six symmetrical peripheral spots, three weaker spots from twin and three strong spots from matrix. The central dot is the (111) plane shared by both twin and matrix along the out-of-plane direction. The pole figure of $Al_{99}Mg_1$ shows the (111) in-plane rotation, resulting in the decrease of twin density.

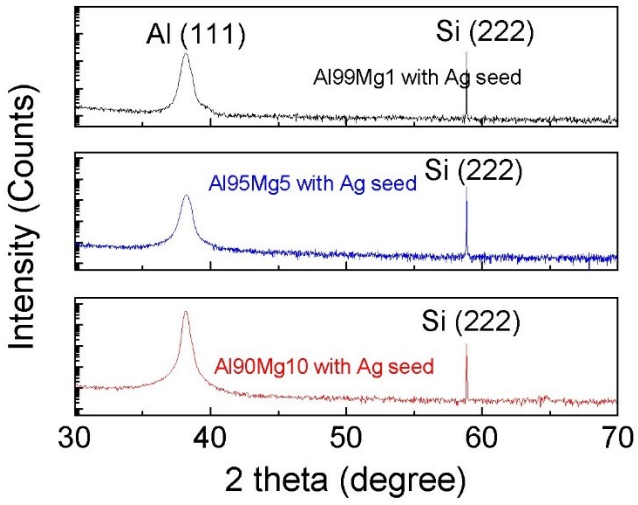

Figure 6.1 XRD profiles of AlMg thin films deposited on single-crystal Si (111) substrates. All films have (111) texture.

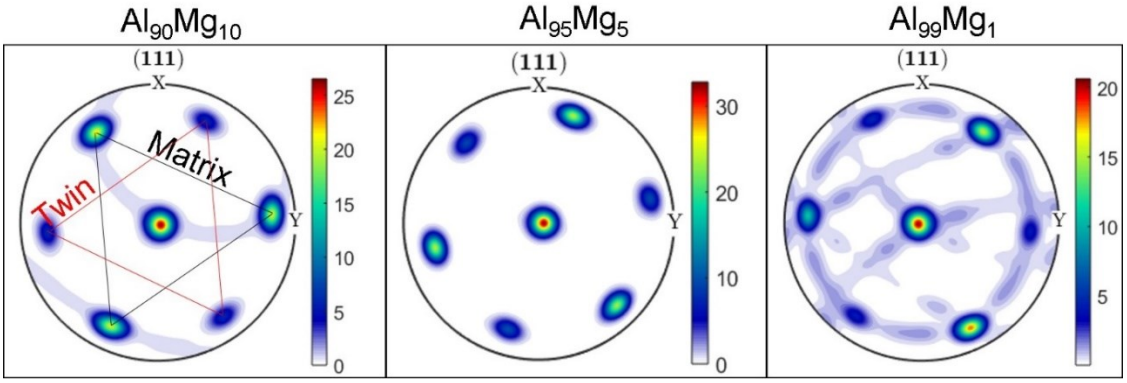

Figure 6.2 The {111} plane pole figures of AlMg films. The projected plane is the sample surface. The six-fold symmetry of {111} pole figure suggests the formation of high-density growth twins.

VI.3.2 The microstructure of as-deposited AlMg thin films

Figure 6.3 shows the microstructure of $Al_{90}Mg_{10}$ thin film via TEM studies. Homogenously distributed small domains can be observed from the plan-view TEM image (Figure 6.3 (a)) and the inserted selected area diffraction (SAD) pattern indicates the epitaxial growth of the film (examined along Al (111) zone axis). XTEM micrograph in Fig. 6.3(b) shows nanoscale columnar grains separated by high-density incoherent twin boundary (ITB), which is confirmed by the SAD pattern in Fig. 6.3(c). The dark layer underneath the AlMg film is the Ag seed layer.

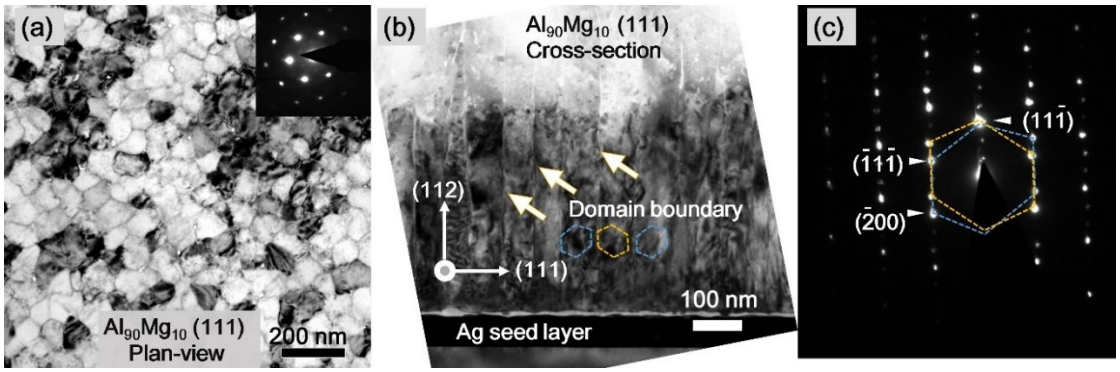

Figure 6.3 TEM images of $Al_{90}Mg_{10}$ thin film. (a) the plan-view TEM micrograph. (b) the cross-section TEM micrograph. (c) The diffraction pattern of cross-section specimen with large aperture.

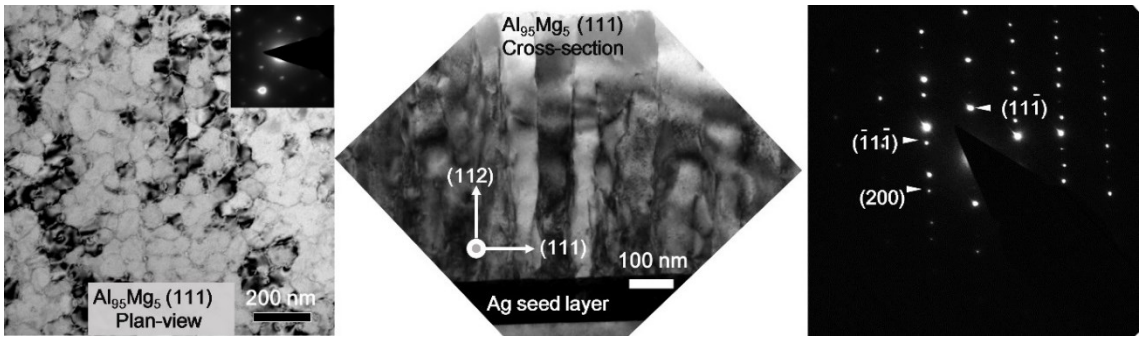

Figure 6.4 TEM images of $Al_{95}Mg_5$ thin film. (a) the plan-view TEM micrograph. (b) the cross-section TEM micrograph. (c) The diffraction pattern of cross-section specimen with large aperture shows the formation of incoherent twin boundaries.

Plan-view and XTEM micrographs (shown in figure 6.4) show a similar microstructure (ITB separated epitaxial nanocolumns) in the $Al_{95}Mg_5$ film. Cross-sectional HRTEM micrograph in Fig. 6.5a captures an entire domain boundary. Three locations (I-III) were selected along a typical ITB. The width of ITB evidently changes through the film thickness. At the film surface (region I in Fig. 6.5 b), a broad ITB labeled

as 9R phase is identified. And the 9R shrinks gradually and becomes a straight narrow ITB as it is getting closer to the film surface. The white dash lines mark two phase boundary (PB) for the 9R phase, a straight PB1 and curved PB2. In region II in the middle of the film, a 67 nm wide 9R phase is identified in Fig 6.5(c). Figure 6.5(d) shows the 9R phase near the bottom of the film in region III is ~ 50 nm wide. A magnified image of the white box in Fig. 6.5(b) is shown in Fig. 6.5(e). It is clear to see the three-layer periodic stacking on {111} plane. Dislocations associated with the 9R phase were measured by constructing Burgers circuits around the faulted regions. The closure failure for the circuit for AB is a/6[211], consistent with the pure edge partial dislocation. The Burgers vector for the BC and CA is a/12 <211>. Based on the model of 9R phase [49, 111], they correlate well with the projection of a 30° or 60° mixed partial dislocations examined along the [011] zone axis. These analyses confirm that the 9R phase contains two mixed partial dislocations and one pure edge dislocation on 3 adjacent {111} planes. Statistical distributions in Fig. 6.6. (based on the TEM micrographs) show that the average grain sizes for the $Al_{99}Mg_1$, $Al_{95}Mg_5$, and $Al_{99}Mg_1$ films are 73, 82 and 93 nm, respectively.

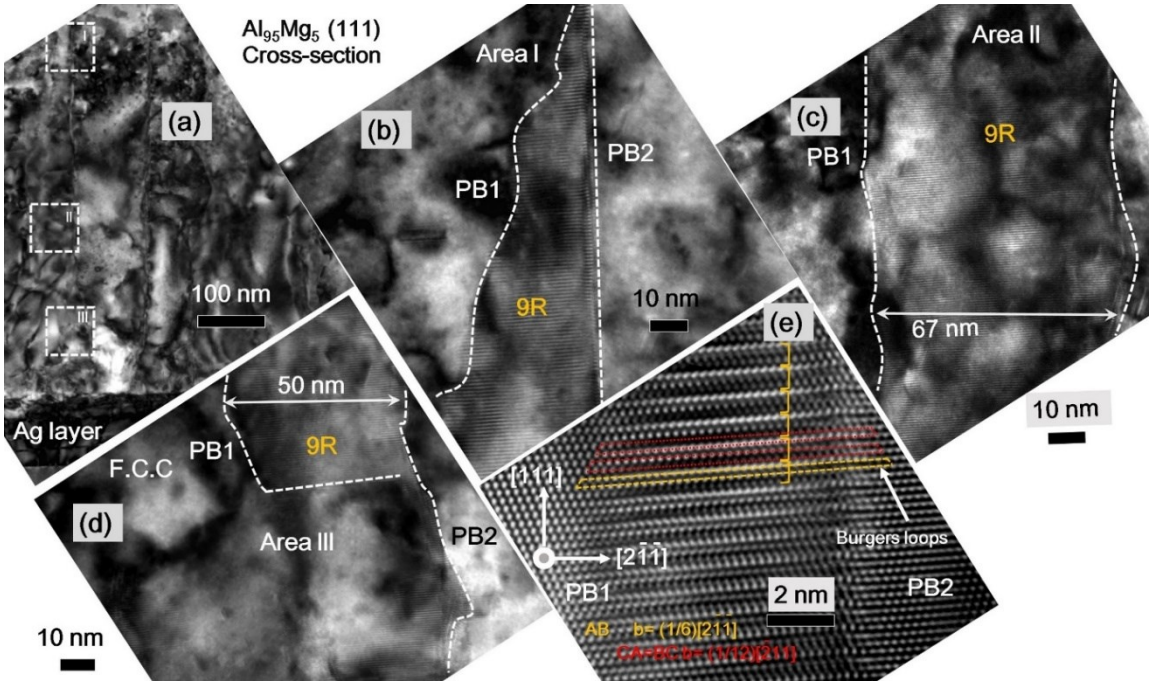

Figure 6.5 Cross-section TEM micrograph of $Al_{95}Mg_5$ thin film showing the board 9R phase. (a) At low magnification, incoherent twin boundary grows from the interface of Ag and $Al_{95}Mg_5$. (b) A higher magnification view shows the shrinkage of 9R phase at the sample surface. (c) A higher magnification view shows the board 9R phase in the middle of the film. (d) A higher magnification view shows the termination of 9R phase at the bottom of the film. (e) A high magnification TEM shows the Burgers loops to identify the nature of the 9R phase.

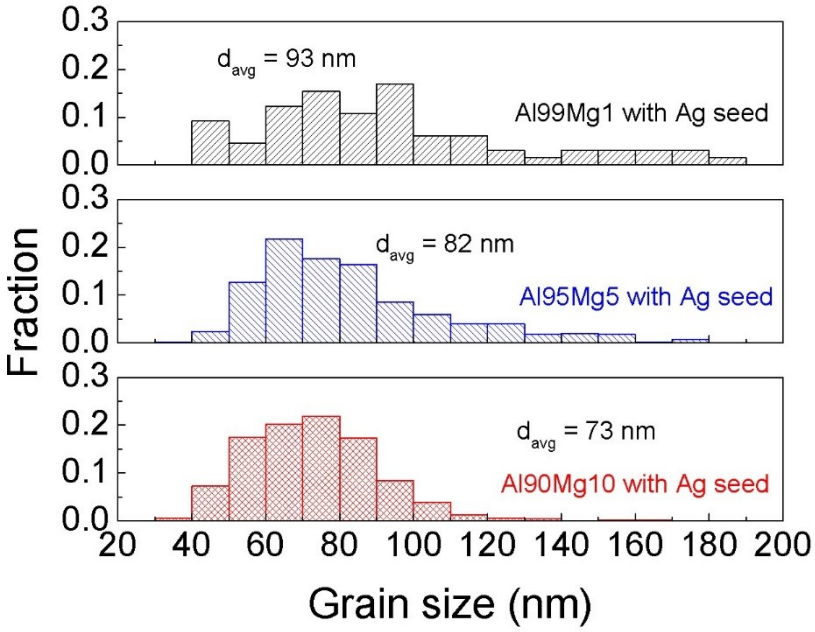

Figure 6.6. Grain size distribution of AlMg thin films.

VI.3.3 Mechanical properties of AlMg thin films

The mechanical behavior of the AlMg thin films with different Mg composition was tested by using nanoindentation. When adding 1 at.% Mg into Al matrix, the film hardness increases to 1.6 GPa, which doubles the hardness of pure Al, ~ 0.8 GPa. Adding more Mg leads to higher hardness, ~ 2 GPa for $Al_{95}Mg_5$, and 2.3 GPa for $Al_{90}Mg_{10}$ (Fig. 6.7).

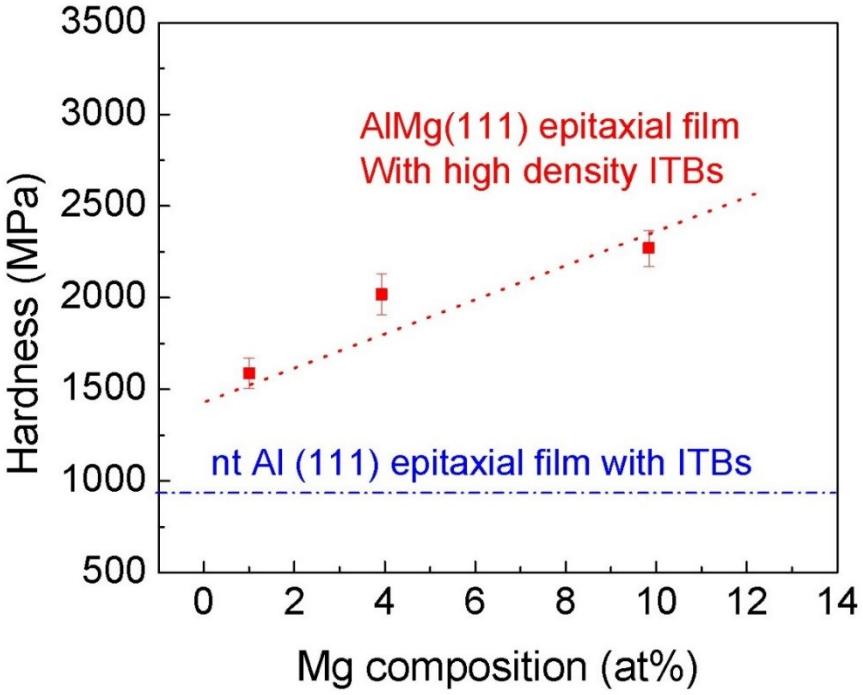

Figure 6.7 Hardness as a function of Mg composition.

In situ uniaxial compression tests have also been carried out on $Al_{90}Mg_{10}$ pillar with ~ 500 nm in diameter in SEM to reveal the real-time deformation processes. Figure 6.8a-b show pillars before and after compressive loading. Compared with the pillar before the compression test, the deformed pillar experienced an obvious barreling on the top without any crack or shear offset up to ~ 20% strain.. The true stress-strain stress curve shows a high flow stress up to 750 MPa, which correlates well with the hardness test according to the Tabor relation [252].

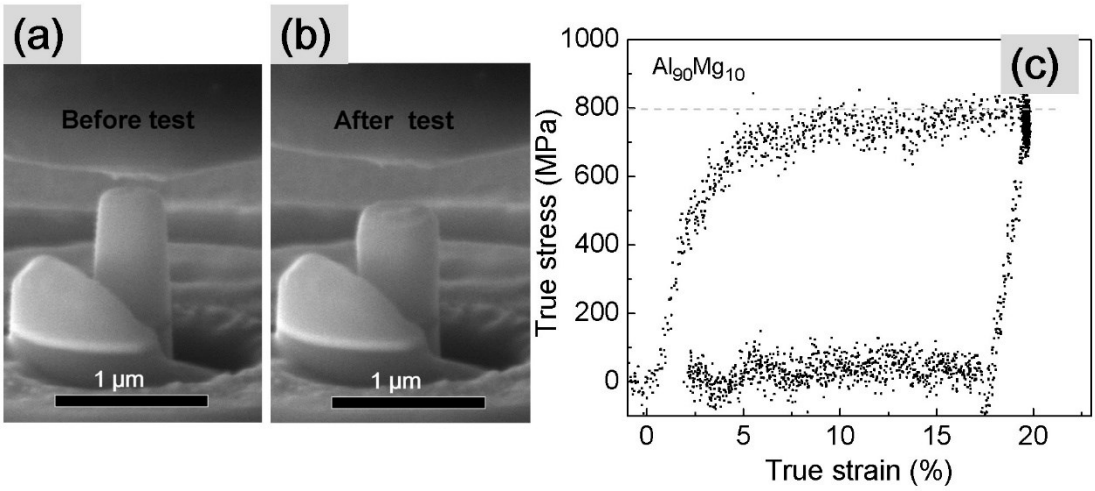

Figure 6.8 In-situ pillar compression test result for $Al_{90}Mg_{10}$ thin film. (a-b) SEM image of the pillar before and after the compression test. (c) The true stress-strain curve for an in-situ compression test showing a flow stress of ~ 800 MPa for the film.

TEM analysis has been performed on the deformed pillar. Pt was deposited to fill in the trench to protect the pillar. TEM-specimen was then prepared by using FIB, followed by the ion milling at low energy to perform ion polishing. Figure 6.9(a) shows the micrographs of the deformed $Al_{90}Mg_{10}$ pillar, where the yellow dash lines indicate the TBs. After the deformation, the ITB boundaries close to the surface detwinned, leaving a single crystal like area near the top. The depth of the top single crystal area, marked by red dash line, is ~ 160 nm, which is similar to the total displacement for the compression test.

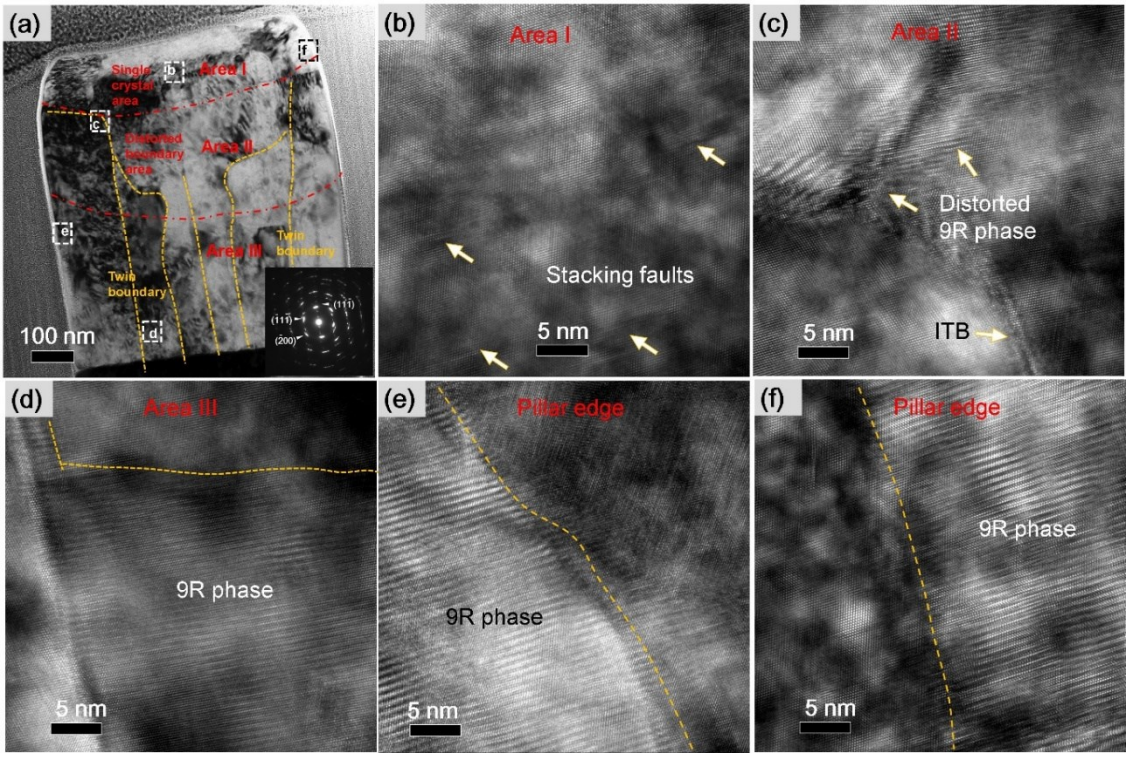

Figure 6.9. TEM micrographs of the deformed $Al_{90}Mg_{10}$ pillar. (a) Cross-section of $Al_{90}Mg_{10}$ pillar after the compression test. (b) A high magnification micrograph shows the single crystal structure of area one. (c) The distorted 9R phase in area two. (d) A high magnification micrograph shows the board 9R phase in area three. (e, f) high magnification micrographs show the board 9R phase at the edge of the pillar.

Figure 6.9(b) shows the enlarged HRTEM of single crystal structure, which is marked as white box b in figure 6.9(a). Although it is mostly a single crystal structure, high-density SFs are observed and marked. We also examined all single crystal area labeled by red dash line, and no boundary can be detected. Below the single crystal area, severely distorted TBs are observed as marked by the yellow lines. The distorted boundaries in area two are curved and bent to the lateral direction. As shown in figure 6.9(c), the distorted boundary contains a triple junction, which is consisted of 9R phase

segments (black circles), an ITB, and a low angle grain boundary. Near the base of the pillars, a broad 9R phase is observed at location d in figure 6.9(a) as shown in figure 6.9(d). So in area three which is near the base of deformed pillar, the crystal structure is similar to the as-deposited films, with high density 9R phase along the domain boundary. An interesting observation is that the broad 9R phase also exists near the outer edge of the pillar as shown in figure 6.9(e). In general free surface is a nature defect sink, which can absorb dislocations and defects, especially under the high shear stress. However, the broad 9R phases are observed on both sides of the pillar after plastic deformation to a true strain of ~ 20%. Even in the single crystal area I, the 9R phase is still stable after the deformation as shown in figure 6.9(f), whereas all the 9R phase and ITBs are eliminated inside the single crystal area.

VI.4 Discussion

VI.4.1 The formation mechanism of high-density ITBs and 9R phase

As mentioned in the previous chapter, monolithic Al forms giant domains with low-density ITBs on Si (111) substrate without any seed layers. However, the Cu and Ag can form high-density ITBs if they have [111] growth orientation [58, 60]. From the crystallographic point of view, for fcc metals grow along [111] direction, adatoms have two possible landing sites, which have the twin orientation relationship. When small twinned orientation nucleuses impinge together, an ITB will form, instead of the normal high-angle grain boundary, to minimize the system energy. But for high SFE metals, small

nucleus can rotate by the partial slip to eliminate the ITB to minimize the system energy. This may explain why monolithic Al (without Ag seed layer) ends up with giant domains with less ITBs. By adding the Ag seed layer, however, the Al domain size can be curtailed to 200 nm [149]. The current study shows that the domain size of Al matrix decreases to 90 nm by adding 1at.% Mg. With the increase of Mg composition, even smaller domain size can be achieved.

Several factors may play roles in the grain size reduction. First, the doping of substitutional elements to the matrix can cause the lattice distortion and the variation in bonding energy landscape. Impurity atoms can act as pinning centers to stall the movement of the matrix atoms, resulting in the decrease of their diffusivity. Rupert et al. [248] reported the nanocrystalline-to-amorphous transition when adding more W into Ni matrix using magnetron sputtering. Using electrodeposition, Hu et al. [14] fabricated as small as 3 nm grain size NiMo ally by adding 21.5% Mo into Ni-base. Using the confined channel die pressing, Zhao et al. [245] found the decrease of grain size by adding more Mg solute. For pure Al, the smallest average grain size after the processing is 10 μm, whereas the Al-5wt.%Mg can be refined to 100 nm. In our case, during the deposition, especially at an early stage, the diffusion of Al bas been pinned by the Mg solute, the lateral growth of the nucleus is impeded by the low diffusion rate which results in a smaller domain size.

Another factor of grain refinement may be relate to the influence of SFE. SFE can be altered by changing test temperature and alloying [253]. Many researchers focus on the influence of alloying on SFE since low SFE metals can trigger more SFs or twin structure to strengthen the materials. Zhao et al. [126] reported that bronze (Cu-10wt.% Zn) with

an SFE of 35 mJ/m^2 could form higher density of twins and wide SFs to achieve higher strength and ductility than that of the Cu with an SFE of 78 mJ/m^2. Similarly, adding Al into Cu can decrease the SFE of CuAl alloys dramatically from 78 to 12 mJ/m^2 when Al concentration is 4.5 wt.% [254, 255]. A linear relationship between the twin thickness and SFE was observed by Zhang et al. [256]. However, adding solutes into matrix not only changes the SFE but also leads to significant solid solution hardening. Thus, it is difficult to isolate the influence of the SFE on strengthening from solid solution strengthening in CuZn system [126]. To avoid the influence of solid solution hardening, the NiCo system has been used to study the influence of solute concentration on the SFE due to the similar atomic size, electronic configuration, and magnetism [239]. Sun et al. [127] observed a similar trend that adding more Co can increase the twin density after the high-pressure torsion. But, they didn't provide a relation between the concentration of Co and SFE. Based on the results from both MD simulation and experiments, the SFE of NiCo alloy will increase and reach a peak at 3 wt.% Co and decrease gradually with more Co doping [239, 253, 257]. This nonlinear relationship has also been predicated in the Al-based alloy. Schulehess et al. [258] calculated the SFE of Al alloy with Cu, Ag, and Mg doping individually. Adding Ag and Cu has similar phenomenon that the SFE will increase and then decrease until the solute concentration exceeds 30 at.% . But, there is a continuous decrease of SFE of AlMg alloy with the increase of the Mg concentration. This continuous SFE decrease in AlMg alloy can help to stabilize the ITB at the island coalescence region and preserve more ITBs, resulting in the smaller domain size. However, the formation mechanism of broad 9R phase is still unclear. 9R phase is a consequence of the

dissociation of ITB. Most of the 9R phase has been observed after the plastic deformation in low SFE metals [49, 111, 122, 259, 260]. So, the Formation of 9R phase may be related to the stress state inside the film during the deposition.

VI.4.2 Strengthening mechanisms for AlMg thin films

In AlMg films, Mg atoms are homogenously distributed in Al matrix due to the non-equilibrium vapor to solid solidification process. Thus, the solid solution and boundary strengthening mechanisms play dominant roles to achieve the high flow stress in AlMg thin films. For the solid-solution strengthening, the Fleischer equation is used to estimate the solute induced increase of friction stress for dislocation slip [261, 262].

$$\Delta\sigma_{ss} = MGb\varepsilon_{ss}^{\frac{3}{2}}\sqrt{c} \qquad \text{Equation 28}$$

$$\varepsilon_{ss} = \left| \frac{\frac{1}{G_{solvent}}\cdot\frac{\partial G}{\partial c}}{1+\frac{1}{2}\left|\frac{1}{G_{solvent}}\cdot\frac{\partial G}{\partial c}\right|} - 3\cdot\frac{1}{b_{solvent}}\cdot\frac{\partial b}{\partial c} \right| \qquad \text{Equation 29}$$

$\Delta\sigma_{ss}$ represents the solute atoms induced increase in yield strength of the alloy, M is the mean orientation factor, which is 3.06 for fcc polycrystalline matrix, G is the shear modulus of the matrix, b is the Burgers vector, and c is the solute concentration. ε_{ss} is called the interaction parameter which accounts for the resistance for the dislocation slip in local region. The ε_{ss} relates to the lattice parameter and shear modulus change for the matrix element and can be calculated by using equation 28 [262].

This is a classic theory for the solid-solution strengthening in coarse grains. The discrepancy has been found in the nanocrystalline material when the grain size is less than

30 nm due to the dislocation pinning effect at grain boundaries [248]. However, the minimum grain size in AlMg film is 70 nm, which is much larger than 30 nm. So, regarding the grain size effect, the classic theory is still applicable for our AlMg thin film system. Based on the equation 28 and 29, $\Delta\sigma_{ss}$ is 17 MPa for $Al_{99}Mg_1$ thin film, and the stress contribution of solid-solution strengthening in $Al_{95}Mg_5$ is ~ 80 MPa. The $Al_{90}Mg_{10}$ film has the highest increase of yield stress due to the solute atoms, 170MPa. For the grain boundary strengthening, we will focus on the ITB strengthening because of the high-density ITBs in all AlMg thin films. Figure 6.10 compares the GB strengthening of normal high-angle grain boundary and ITB for pure Al by using a classical Hall-Petch plot. Based on the slope, ITB seems to be a stronger barrier for the dislocation transmission than the conventional high angle grain boundaries. Based on the Hall-Petch slope of the ITB, the strength of grain boundary strengthening effect can be calculated as a function of grain size. Thus, the ITB strengthening contribution for $Al_{99}Mg_1$, $Al_{95}Mg_5$, and $Al_{90}Mg_{10}$ are around 600MPa, 620MPa, and 670MPa separately. So, the flow stress of AlMg films based on the grain boundary and solid-solution strengthening are 617MPa, 700 MPa, 840 MPa for $Al_{99}Mg_1$, $Al_{95}Mg_5$, and $Al_{90}Mg_{10}$, which correlate well with our experiment results derived from nanoindentation measurements.

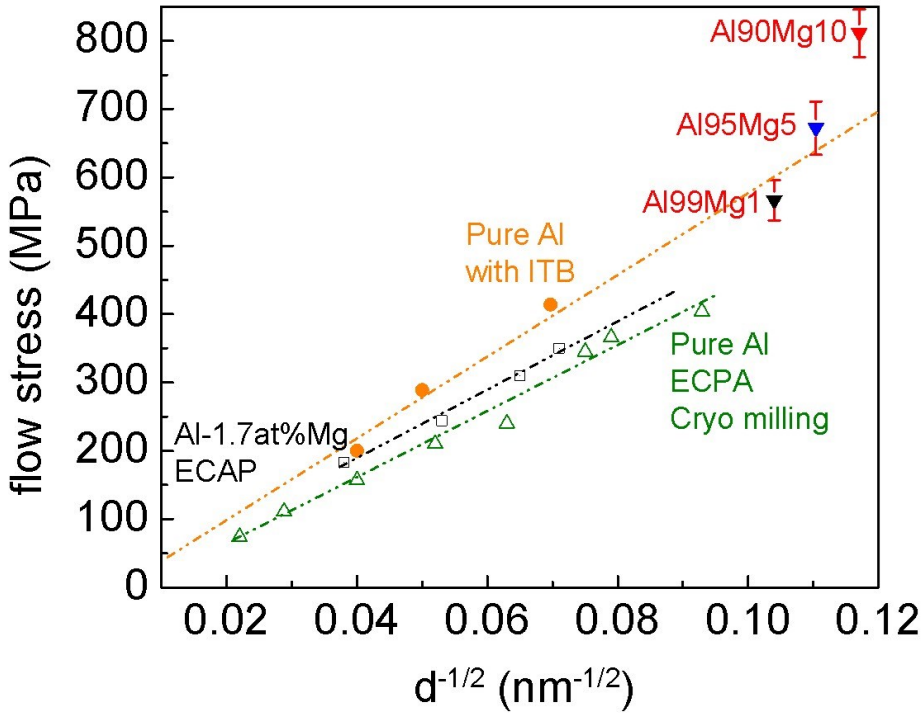

Figure 6.10. Flow stress as a function of $d^{-1/2}$ for Al and AlMg with different grain boundaries.

VI.5 Conclusion

Epitaxial AlMg thin films with various Mg concentration have been fabricated using magnetron sputtering technique. Using the Ag seed layer, domains with an average dimension less than 100 nm have been synthesized. Furthermore these domains are separately primarily by ITBs. The nanoindentation and in-situ pillar compression tests were employed to test AlMg films with high-density ITB. A high flow stress (820 MPa) in certain AlMg thin films has been measured, and the strengthening mechanisms are also investigated. The strong ITB barriers play an important role to strengthen the film.

Combined with the solid-solution strengthening, the calculated flow stress correlated well with the experimental data.

CHAPTER VII

SUMMARY

In conclusion, several important results stand out. First, growth twins have been observed in sputter-deposited polycrystalline Al films and the fraction of twinned grain increased with increasing film thickness and decreased thereafter in the thicker films. A thermodynamic twin nucleation model has been postulated to explain the formation mechanism of inclined growth twin in Al films. Although the thin film has low twinned grain fraction, the twin formation mechanisms presented in this study suggest new perspectives tailor the formation of growth twins in high SFE metals, such as Al.

Most excitingly, the influence of film texture on the formation of TBs has investigated in Al textured films. Epitaxial Al (112) film has the highest density of ITBs due to the existence of HAGB introducing by the Al (102). The smaller domain size can thus be achieved by introducing HAGBs into the twinned bicrystal structure to inhibit the abnormal growth of single variant. Nanoindentation studies show that TBs are stronger barriers to block the transmission of dislocations and hold the promise to deliver high strength nanotwinned Al.

Besides the orientation dependence of twin formation, the high density ITBs with board 9R phase AlMg alloy has been fabricated using magnetron sputtering technique. By adding the Ag seed layer, epitaxial (111) thin film with fine domains is achieved. Furthermore, the nanoindentation and in-situ pillar compression tests were employed to test AlMg films with high-density ITB. A high flow stress (820 MPa) in certain AlMg thin

films has been measured, and the strengthening mechanisms are also investigated. Based on the work presented in this dissertation, more following questions have been developed. By explaining these questions, I hope to pursue a better understanding of the twin deformation mechanisms.

REFERENCES

[1] E. Hall, The deformation and ageing of mild steel: III discussion of results, Proceedings of the Physical Society. Section B 64(9) (1951) 747-753.

[2] N. Petch, The cleavage strength of polycrystals, J. Iron Steel Inst. 174 (1953) 25-28.

[3] R. Peierls, The size of a dislocation, Proceedings of the Physical Society 52(1) (1940) 34-37.

[4] F. Nabarro, Dislocations in a simple cubic lattice, Proceedings of the Physical Society 59(2) (1947) 256-272.

[5] A. Misra, J. Hirth, R. Hoagland, Length-scale-dependent deformation mechanisms in incoherent metallic multilayered composites, Acta Materialia 53(18) (2005) 4817-4824.

[6] M.A. Meyers, A. Mishra, D.J. Benson, Mechanical properties of nanocrystalline materials, Progress in Materials Science 51(4) (2006) 427-556.

[7] J. Weertman, D. Farkas, K. Hemker, H. Kung, M. Mayo, R. Mitra, H. Van Swygenhoven, Structure and mechanical behavior of bulk nanocrystalline materials, MRS Bull 24(2) (1999) 44-50.

[8] V. Yamakov, D. Wolf, S. Phillpot, A. Mukherjee, H. Gleiter, Deformation-mechanism map for nanocrystalline metals by molecular-dynamics simulation, Nature Materials 3(1) (2004) 43-47.

[9] S. Yip, Nanocrystals: the strongest size, Nature 391(6667) (1998) 532-533.

[10] J. Schiøtz, K.W. Jacobsen, A maximum in the strength of nanocrystalline copper, Science 301(5638) (2003) 1357-1359.

[11] J. Schiøtz, F.D. Di Tolla, K.W. Jacobsen, Softening of nanocrystalline metals at very small grain sizes, Nature 391(6667) (1998) 561-563.

[12] Z. Shan, E. Stach, J. Wiezorek, J. Knapp, D. Follstaedt, S. Mao, Grain boundary-mediated plasticity in nanocrystalline nickel, Science 305(5684) (2004) 654-657.

[13] L. Wang, J. Teng, P. Liu, A. Hirata, E. Ma, Z. Zhang, M. Chen, X. Han, Grain rotation mediated by grain boundary dislocations in nanocrystalline platinum, Nature Communications 5 (2014).

[14] J. Hu, Y. Shi, X. Sauvage, G. Sha, K. Lu, Grain boundary stability governs hardening and softening in extremely fine nanograined metals, Science 355(6331) (2017) 1292-1296.

[15] C. Koch, Optimization of strength and ductility in nanocrystalline and ultrafine grained metals, Scripta Materialia 49(7) (2003) 657-662.

[16] B. Clemens, H. Kung, S. Barnett, Structure and strength of multilayers, MRS Bulletin 24(02) (1999) 20-26.

[17] A. Misra, H. Kung, J.D. Embury, Preface to the viewpoint set on: deformation and stability of nanoscale metallic multilayers, Scripta Materialia 50(6) (2004) 707-710.

[18] S.I. Rao, P.M. Hazzledine, Atomistic simulations of dislocation–interface interactions in the Cu-Ni multilayer system, Philosophical Magazine A 80(9) (2000) 2011-2040.

[19] X. Zhang, A. Misra, H. Wang, T. Shen, M. Nastasi, T. Mitchell, J. Hirth, R. Hoagland, J. Embury, Enhanced hardening in Cu/330 stainless steel multilayers by nanoscale twinning, Acta Materialia 52(4) (2004) 995-1002.

[20] P. Anderson, J. Carpenter, Estimates of interfacial properties in Cu/Ni multilayer thin films using hardness data, Scripta Materialia 62(6) (2010) 325-328.

[21] Y. Liu, D. Bufford, H. Wang, C. Sun, X. Zhang, Mechanical properties of highly textured Cu/Ni multilayers, Acta Materialia 59(5) (2011) 1924-1933.

[22] D. Bufford, Z. Bi, Q. Jia, H. Wang, X. Zhang, Nanotwins and stacking faults in high-strength epitaxial Ag/Al multilayer films, Applied Physics Letters 101(22) (2012) 223112.

[23] M. Phillips, B. Clemens, W. Nix, Microstructure and nanoindentation hardness of Al/Al 3 Sc multilayers, Acta Materialia 51(11) (2003) 3171-3184.

[24] I. Bakonyi, L. Péter, Electrodeposited multilayer films with giant magnetoresistance (GMR): Progress and problems, Progress in Materials Science 55(3) (2010) 107-245.

[25] W. Egelhoff Jr, M. Kief, Antiferromagnetic coupling in Fe/Cu/Fe and Co/Cu/Co multilayers on Cu (111), Physical Review B 45(14) (1992) 7795.

[26] A. Misra, H. Krug, Deformation behavior of nanostructured metallic multilayers, Advanced Engineering Materials 3(4) (2001) 217-222.

[27] A. Misra, J. Hirth, R. Hoagland, J. Embury, H. Kung, Dislocation mechanisms and symmetric slip in rolled nano-scale metallic multilayers, Acta Materialia 52(8) (2004) 2387-2394.

[28] M. Demkowicz, R. Hoagland, J. Hirth, Interface structure and radiation damage resistance in Cu-Nb multilayer nanocomposites, Physical Review Letters 100(13) (2008) 136102.

[29] N. Li, M. Nastasi, A. Misra, Defect structures and hardening mechanisms in high dose helium ion implanted Cu and Cu/Nb multilayer thin films, International Journal of Plasticity 32 (2012) 1-16.

[30] J. Koehler, Attempt to design a strong solid, Physical Review B 2(2) (1970) 547.

[31] D. Bacon, D. Babnett, R. Scattebgood, On the anisotropic elastic field of a dislocation segment in three dimensions, Philosophical Magazine A 39(2) (1979) 231-235.

[32] B. Wang, H. Idrissi, M. Galceran, M.-S. Colla, S. Turner, S. Hui, J.-P. Raskin, T. Pardoen, S. Godet, D. Schryvers, Advanced TEM investigation of the plasticity mechanisms in nanocrystalline freestanding palladium films with nanoscale twins, International Journal of Plasticity 37 (2012) 140-156.

[33] I.J. Beyerlein, N.A. Mara, D. Bhattacharyya, D.J. Alexander, C.T. Necker, Texture evolution via combined slip and deformation twinning in rolled silver–copper cast eutectic nanocomposite, International Journal of Plasticity 27(1) (2011) 121-146.

[34] R. Hoagland, T. Mitchell, J. Hirth, H. Kung, On the strengthening effects of interfaces in multilayer fee metallic composites, Philosophical Magazine A 82(4) (2002) 643-664.

[35] B. Shoykhet, M. Grinfeld, P. Hazzledine, Internal stresses and strains in coherent multilayers, Acta Materialia 46(11) (1998) 3761-3766.

[36] J. McKeown, A. Misra, H. Kung, R. Hoagland, M. Nastasi, Microstructures and strength of nanoscale Cu–Ag multilayers, Scripta Materialia 46(8) (2002) 593-598.

[37] R. Hull, J.C. Bean, Misfit dislocations in lattice-mismatched epitaxial films, Critical Reviews in Solid State and Material Sciences 17(6) (1992) 507-546.

[38] Q. Li, P.M. Anderson, Dislocation-based modeling of the mechanical behavior of epitaxial metallic multilayer thin films, Acta Materialia 53(4) (2005) 1121-1134.

[39] J. Wang, A. Misra, R. Hoagland, J. Hirth, Slip transmission across fcc/bcc interfaces with varying interface shear strengths, Acta Materialia 60(4) (2012) 1503-1513.

[40] N. Li, N. Mara, J. Wang, P. Dickerson, J. Huang, A. Misra, Ex situ and in situ measurements of the shear strength of interfaces in metallic multilayers, Scripta Materialia 67(5) (2012) 479-482.

[41] J. Matthews, A. Blakeslee, Exact determination of electrical properties of wurtzite Al1-xInxN/(AlN)/GaN heterostructures (0.07⩽ x⩽ 0.21) by means of a detailed charge balance equation, J. Cryst. Growth 27 (1974) 118.

[42] M.J. Demkowicz, J. Wang, R.G. Hoagland, Interfaces between dissimilar crystalline solids, Dislocations in solids 14 (2008) 141-207.

[43] J. Wang, R. Hoagland, J. Hirth, A. Misra, Atomistic simulations of the shear strength and sliding mechanisms of copper–niobium interfaces, Acta Materialia 56(13) (2008) 3109-3119.

[44] Y. Liu, Y. Chen, K.Y. Yu, H. Wang, J. Chen, X. Zhang, Stacking fault and partial dislocation dominated strengthening mechanisms in highly textured Cu/Co multilayers, International Journal of Plasticity 49 (2013) 152-163.

[45] M.D. Sangid, T. Ezaz, H. Sehitoglu, I.M. Robertson, Energy of slip transmission and nucleation at grain boundaries, Acta Materialia 59(1) (2011) 283-296.

[46] K. Lu, L. Lu, S. Suresh, Strengthening materials by engineering coherent internal boundaries at the nanoscale, Science 324(5925) (2009) 349-352.

[47] L.E. Murr, Interfacial phenomena in metals and alloys, 1st edition, Pearson Education: Addison-Wesely Educational Publishers Inc, New Jersey, (1975).

[48] D.L. Medlin, M.J. Mills, W.M. Stobbs, M.S. Daw, F. Cosandey, Hrtem Observations Of A Σ=3 {112} Bicrystal Boundary In Aluminum, MRS Online Proceedings Library Archive 295 (1992) 91 (6 pages).

[49] J. Wang, A. Misra, J. Hirth, Shear response of Σ 3 {112} twin boundaries in face-centered-cubic metals, Physical Review B 83(6) (2011) 064106.

[50] D.L. Olmsted, S.M. Foiles, E.A. Holm, Survey of computed grain boundary properties in face-centered cubic metals: I. Grain boundary energy, Acta Materialia 57(13) (2009) 3694-3703.

[51] T. Zhu, J. Li, A. Samanta, H.G. Kim, S. Suresh, Interfacial plasticity governs strain rate sensitivity and ductility in nanostructured metals, Proceedings of the National Academy of Sciences 104(9) (2007) 3031-3036.

[52] L. Lu, Y. Shen, X. Chen, L. Qian, K. Lu, Ultrahigh Strength and High Electrical Conductivity in Copper, Science 304(5669) (2004) 422-426.

[53] L. Lu, X. Chen, X. Huang, K. Lu, Revealing the maximum strength in nanotwinned copper, Science 323(5914) (2009) 607-610.

[54] X. Li, Y. Wei, L. Lu, K. Lu, H. Gao, Dislocation nucleation governed softening and maximum strength in nano-twinned metals, Nature 464(7290) (2010) 877-880.

[55] K. Lu, Making strong nanomaterials ductile with gradients, Science 345(6203) (2014) 1455-1456.

[56] X. Wu, P. Jiang, L. Chen, F. Yuan, Y.T. Zhu, Extraordinary strain hardening by gradient structure, Proceedings of the National Academy of Sciences 111(20) (2014) 7197-7201.

[57] M. Ashby, The deformation of plastically non-homogeneous materials, Philosophical Magazine 21(170) (1970) 399-424.

[58] O. Anderoglu, A. Misra, H. Wang, F. Ronning, M.F. Hundley, X. Zhang, Epitaxial nanotwinned Cu films with high strength and high conductivity, Applied Physics Letters 93(8) (2008) 083108.

[59] X. Zhang, A. Misra, Superior thermal stability of coherent twin boundaries in nanotwinned metals, Scripta Materialia 66(11) (2012) 860-865.

[60] D. Bufford, H. Wang, X. Zhang, High strength, epitaxial nanotwinned Ag films, Acta Materialia 59(1) (2011) 93-101.

[61] Y. Zhao, T.A. Furnish, M.E. Kassner, A.M. Hodge, Thermal stability of highly nanotwinned copper: The role of grain boundaries and texture, Journal of Materials Research 27(24) (2012) 3049-3057.

[62] T. LaGrange, B.W. Reed, M. Wall, J. Mason, T. Barbee, M. Kumar, Topological view of the thermal stability of nanotwinned copper, Applied Physics Letters 102(1) (2013) 011905.

[63] O. Anderoglu, A. Misra, H. Wang, X. Zhang, Thermal stability of sputtered Cu films with nanoscale growth twins, Journal of Applied Physics 103(9) (2008) 094322.

[64] J. Brown, N. Ghoniem, Structure and motion of junctions between coherent and incoherent twin boundaries in copper, Acta Materialia 57(15) (2009) 4454-4462.

[65] D. Bufford, H. Wang, X. Zhang, Thermal stability of twins and strengthening mechanisms in differently oriented epitaxial nanotwinned Ag films, Journal of Materials Research 28(13) (2013) 1729-1739.

[66] X. Zhang, H. Wang, X. Chen, L. Lu, K. Lu, R. Hoagland, A. Misra, High-strength sputter-deposited Cu foils with preferred orientation of nanoscale growth twins, Applied Physics Letters 88(17) (2006) 173116.

[67] Z.-H. Jin, P. Gumbsch, E. Ma, K. Albe, K. Lu, H. Hahn, H. Gleiter, The interaction mechanism of screw dislocations with coherent twin boundaries in different face-centred cubic metals, Scripta Materialia 54(6) (2006) 1163-1168.

[68] C. Deng, F. Sansoz, Enabling ultrahigh plastic flow and work hardening in twinned gold nanowires, Nano Letters 9(4) (2009) 1517-1522.

[69] J. Wang, N. Li, O. Anderoglu, X. Zhang, A. Misra, J. Huang, J. Hirth, Detwinning mechanisms for growth twins in face-centered cubic metals, Acta Materialia 58(6) (2010) 2262-2270.

[70] Z. Wu, Y. Zhang, D. Srolovitz, Deformation mechanisms, length scales and optimizing the mechanical properties of nanotwinned metals, Acta Materialia 59(18) (2011) 6890-6900.

[71] O. Anderoglu, A. Misra, F. Ronning, H. Wang, X. Zhang, Significant enhancement of the strength-to-resistivity ratio by nanotwins in epitaxial Cu films, Journal of Applied Physics 106(2) (2009) 24313.

[72] K. Yu, D. Bufford, Y. Chen, Y. Liu, H. Wang, X. Zhang, Basic criteria for formation of growth twins in high stacking fault energy metals, Applied Physics Letters 103(18) (2013) 181903.

[73] Y. Liu, D. Bufford, S. Rios, H. Wang, J. Chen, J. Zhang, X. Zhang, A formation mechanism for ultra-thin nanotwins in highly textured Cu/Ni multilayers, Journal of Applied Physics 111(7) (2012) 073526.

[74] L.B. Freund, S. Suresh, Thin film materials: stress, defect formation and surface evolution, Cambridge University Press2004.

[75] Y. Zhang, J. Wang, H. Shan, K. Zhao, Strengthening high-stacking-fault-energy metals via parallelogram nanotwins, Scripta Materialia 108 (2015) 35-39.

[76] G.T. Gray III, High-strain-rate deformation: mechanical behavior and deformation substructures induced, Annual Review of Materials Research 42 (2012) 285-303.

[77] F. Cao, I.J. Beyerlein, F.L. Addessio, B.H. Sencer, C.P. Trujillo, E.K. Cerreta, G.T. Gray III, Orientation dependence of shock-induced twinning and substructures in a copper bicrystal, Acta Materialia 58(2) (2010) 549-559.

[78] G. Gray, Deformation twinning in Al-4.8 wt% Mg, Acta Metallurgica 36(7) (1988) 1745-1754.

[79] W. Zhao, N. Tao, J. Guo, Q. Lu, K. Lu, High density nano-scale twins in Cu induced by dynamic plastic deformation, Scripta Materialia 53(6) (2005) 745-749.

[80] T. Blewitt, R. Coltman, J. Redman, Low‐Temperature Deformation of Copper Single Crystals, Journal of Applied Physics 28(6) (1957) 651-660.

[81] M. Yoo, J. Lee, Deformation twinning in hcp metals and alloys, Philosophical Magazine A 63(5) (1991) 987-1000.

[82] J. Lee, M. Yoo, Theory of shape bifurcation during nucleation in solids, Metallurgical and Materials Transactions A 23(7) (1992) 1891-1900.

[83] J. Venables, Deformation twinning in face-centred cubic metals, Philosophical Magazine 6(63) (1961) 379-396.

[84] J.W. Christian, S. Mahajan, Deformation twinning, Progress in Materials Science 39(1–2) (1995) 1-157.

[85] S. Mahajan, G. Chin, Formation of deformation twins in fcc crystals, Acta Metallurgica 21(10) (1973) 1353-1363.

[86] S. Kibey, J. Liu, D.D. Johnson, H. Sehitoglu, Generalized planar fault energies and twinning in Cu–Al alloys, Applied Physics Letters 89(19) (2006) 191911.

[87] J.P. Hirth, Theory of dislocations, 1 st edition, New York : McGraw-Hill, 1968, p 475.

[88] J.R. Rice, Dislocation nucleation from a crack tip: an analysis based on the Peierls concept, Journal of the Mechanics and Physics of Solids 40(2) (1992) 239-271.

[89] S. Hai, E. Tadmor, Deformation twinning at aluminum crack tips, Acta Materialia 51(1) (2003) 117-131.

[90] I.J. Beyerlein, X. Zhang, A. Misra, Growth twins and deformation twins in metals, Annual Review of Materials Research 44 (2014) 329-363.

[91] E. Tadmor, S. Hai, A Peierls criterion for the onset of deformation twinning at a crack tip, Journal of the Mechanics and Physics of Solids 51(5) (2003) 765-793.

[92] D. Warner, W. Curtin, S. Qu, Rate dependence of crack-tip processes predicts twinning trends in fcc metals, Nature Materials 6(11) (2007) 876-881.

[93] S. Kibey, J. Liu, D. Johnson, H. Sehitoglu, Predicting twinning stress in fcc metals: linking twin-energy pathways to twin nucleation, Acta Materialia 55(20) (2007) 6843-6851.

[94] V. Yamakov, D. Wolf, M. Salazar, S. Phillpot, H. Gleiter, Length-scale effects in the nucleation of extended dislocations in nanocrystalline Al by molecular-dynamics simulation, Acta Materialia 49(14) (2001) 2713-2722.

[95] V. Yamakov, D. Wolf, S.R. Phillpot, A.K. Mukherjee, H. Gleiter, Dislocation processes in the deformation of nanocrystalline aluminium by molecular-dynamics simulation, Nature Materials 1(1) (2002) 45-49.

[96] F. Zhao, L. Wang, D. Fan, B. Bie, X. Zhou, T. Suo, Y. Li, M. Chen, C. Liu, M. Qi, Macrodeformation Twins in Single-Crystal Aluminum, Physical Review Letters 116(7) (2016) 075501.

[97] X. Liao, F. Zhou, E. Lavernia, S. Srinivasan, M. Baskes, D. He, Y. Zhu, Deformation mechanism in nanocrystalline Al: Partial dislocation slip, Applied Physics Letters 83(4) (2003) 632-634.

[98] W. Han, G. Cheng, S. Li, S. Wu, Z. Zhang, Deformation induced microtwins and stacking faults in aluminum single crystal, Physical Review Letters 101(11) (2008) 115505.

[99] Y. Zhu, X. Liao, X. Wu, Deformation twinning in nanocrystalline materials, Progress in Materials Science 57(1) (2012) 1-62.

[100] Y. Zhu, X. Wu, X. Liao, J. Narayan, S. Mathaudhu, L. Kecskes, Twinning partial multiplication at grain boundary in nanocrystalline fcc metals, Applied Physics Letters 95(3) (2009) 031909.

[101] Y. Zhu, X. Liao, X. Wu, Deformation twinning in bulk nanocrystalline metals: experimental observations, JOM Journal of the Minerals, Metals and Materials Society 60(9) (2008) 60-64.

[102] X. Liao, Y. Zhao, Y. Zhu, R. Valiev, D. Gunderov, Grain-size effect on the deformation mechanisms of nanostructured copper processed by high-pressure torsion, Journal of Applied Physics 96(1) (2004) 636-640.

[103] J. Huang, Y. Zhu, H. Jiang, T. Lowe, Microstructures and dislocation configurations in nanostructured Cu processed by repetitive corrugation and straightening, Acta Materialia 49(9) (2001) 1497-1505.

[104] X. Wu, X. Liao, S. Srinivasan, F. Zhou, E. Lavernia, R. Valiev, Y. Zhu, New deformation twinning mechanism generates zero macroscopic strain in nanocrystalline metals, Physical Review Letters 100(9) (2008) 095701.

[105] Y. Wang, J. Ho, X. Liao, H. Li, S. Ringer, Y. Zhu, Mechanism of grain growth during severe plastic deformation of a nanocrystalline Ni–Fe alloy, Applied Physics Letters 94(1) (2009) 011908.

[106] M. Ashby, E. Harper, Harvard report September, Cambridge (MA): Harvard University (1967).

[107] X. Liao, F. Zhou, E. Lavernia, D. He, Y. Zhu, Deformation twins in nanocrystalline Al, Applied Physics Letters 83(24) (2003) 5062-5064.

[108] X. Liao, J. Huang, Y. Zhu, F. Zhou, E. Lavernia, Nanostructures and deformation mechanisms in a cryogenically ball-milled Al-Mg alloy, Philosophical Magazine 83(26) (2003) 3065-3075.

[109] X.Z. Liao, Y.H. Zhao, S.G. Srinivasan, Y.T. Zhu, R.Z. Valiev, D.V. Gunderov, Deformation twinning in nanocrystalline copper at room temperature and low strain rate, Applied Physics Letters 84(4) (2004) 592-594.

[110] Y. Zhu, X. Liao, R. Valiev, Formation mechanism of fivefold deformation twins in nanocrystalline face-centered-cubic metals, Applied Physics Letters 86(10) (2005) 103112.

[111] D. Medlin, G. Campbell, C.B. Carter, Stacking defects in the 9R phase at an incoherent twin boundary in copper, Acta Materialia 46(14) (1998) 5135-5142.

[112] U. Wolf, P. Gumbsch, H. Ichinose, H. Fischmeister, Incoherent Σ3 grain boundaries in FCC metals: The influence of inclination on the boundary structure and energy, Le Journal de Physique Colloques 51(C1) (1990) C1-359-C1-366.

[113] F. Ernst, M.W. Finnis, D. Hofmann, T. Muschik, U. Schönberger, U. Wolf, M. Methfessel, Theoretical prediction and direct observation of the 9R structure in Ag, Physical Review Letters 69(4) (1992) 620-623.

[114] D. Hofmann, M. Finnis, Theoretical and experimental analysis of near Σ3 (211) boundaries in silver, Acta Metallurgica et Materialia 42(10) (1994) 3555-3567.

[115] T. Muschik, W. Laub, U. Wolf, M. Finnis, W. Gust, Energetic and kinetic aspects of the faceting transformation of a Σ3 grain boundary in Cu, Acta Metallurgica et Materialia 41(7) (1993) 2163-2171.

[116] G.H. Campbell, D.K. Chan, D.L. Medlin, J.E. Angelo, C.B. Carter, Dynamic observation of the fcc to 9r shear transformation in a copper $\Sigma = 3$ incoherent twin boundary, Scripta Materialia 35(7) (1996) 837-842.

[117] J. Rittner, D. Seidman, < 110> symmetric tilt grain-boundary structures in fcc metals with low stacking-fault energies, Physical Review B 54(10) (1996) 6999.

[118] J. Rittner, D. Seidman, K. Merkle, Grain-boundary dissociation by the emission of stacking faults, Physical Review B 53(8) (1996) R4241.

[119] H. Ichinose, Y. Ishida, N. Baba, K. Kanaya, Lattice imaging analysis of Σ3 coincidence-site-lattice boundaries in gold, Philosophical Magazine A 52(1) (1985) 51-59.

[120] D. Bufford, Y. Liu, Y. Zhu, Z. Bi, Q. Jia, H. Wang, X. Zhang, Formation mechanisms of high-density growth twins in aluminum with high stacking-fault energy, Materials Research Letters 1(1) (2013) 51-60.

[121] D. Wolf, Structure-energy correlation for grain boundaries in F.C.C. metals—III. Symmetrical tilt boundaries, Acta Metallurgica et Materialia 38(5) (1990) 781-790.

[122] L. Liu, J. Wang, S. Gong, S. Mao, High resolution transmission electron microscope observation of zero-strain deformation twinning mechanisms in Ag, Physical review letters 106(17) (2011) 175504.

[123] X.L. Ma, H. Zhou, J. Narayan, Y.T. Zhu, Stacking-fault energy effect on zero-strain deformation twinning in nanocrystalline Cu–Zn alloys, Scripta Materialia 109 (2015) 89-93.

[124] Z.-H. Jin, P. Gumbsch, K. Albe, E. Ma, K. Lu, H. Gleiter, H. Hahn, Interactions between non-screw lattice dislocations and coherent twin boundaries in face-centered cubic metals, Acta Materialia 56(5) (2008) 1126-1135.

[125] H. Van Swygenhoven, P. Derlet, A. Frøseth, Stacking fault energies and slip in nanocrystalline metals, Nature Materials 3(6) (2004) 399-403.

[126] Y. Zhao, Y. Zhu, X. Liao, Z. Horita, T. Langdon, Tailoring stacking fault energy for high ductility and high strength in ultrafine grained Cu and its alloy, Applied Physics Letters 89(12) (2006) 121906.

[127] P.-L. Sun, Y. Zhao, J. Cooley, M. Kassner, Z. Horita, T. Langdon, E. Lavernia, Y. Zhu, Effect of stacking fault energy on strength and ductility of nanostructured alloys: An evaluation with minimum solution hardening, Materials Science and Engineering: A 525(1) (2009) 83-86.

[128] P. Barna, M. Adamik, Fundamental structure forming phenomena of polycrystalline films and the structure zone models, Thin solid films 317(1) (1998) 27-33.

[129] F. Baumann, D. Chopp, T.D. de la Rubia, G. Gilmer, J. Greene, H. Huang, S. Kodambaka, P. O'sullivan, I. Petrov, Multiscale modeling of thin-film deposition: applications to Si device processing, MRS Bulletin 26(03) (2001) 182-189.

[130] H. Wang, A. Tiwari, A. Kvit, X. Zhang, J. Narayan, Epitaxial growth of TaN thin films on Si (100) and Si (111) using a TiN buffer layer, Applied Physics Letters 80(13) (2002) 2323-2325.

[131] J. Matthews, A. Blakeslee, Defects in epitaxial multilayers: I. Misfit dislocations, Journal of Crystal Growth 27 (1974) 118-125.

[132] K.-N. Tu, J.W. Mayer, L.C. Feldman, Electronic thin film science, Macmillan, New York, 1992.

[133] W. Wegscheider, K. Eberl, G. Abstreiter, H. Cerva, H. Oppolzer, Novel relaxation process in strained Si/Ge superlattices grown on Ge (001), Applied Physics Letters 57(15) (1990) 1496-1498.

[134] J. Neethling, V. Alberts, Multiple twinning in GaAs epitaxial layers grown on Si (001) and Si (111), Journal of Applied Physics 75(7) (1994) 3435-3440.

[135] L. Liu, Y. Zhang, T.-Y. Zhang, Strain relaxation in heteroepitaxial films by misfit twinning. I. Critical thickness, Journal of Applied Physics 101(6) (2007) 063501.

[136] W.C. Oliver, G.M. Pharr, An improved technique for determining hardness and elastic modulus using load and displacement sensing indentation experiments, Journal of Materials Research 7(06) (1992) 1564-1583.

[137] J. Pethica, W. Oliver, Mechanical properties of nanometre volumes of material: use of the elastic response of small area indentations, MRS Proceedings, Cambridge Univ Press, 1988, p. 13.

[138] G. Pharr, W. Oliver, F. Brotzen, On the generality of the relationship among contact stiffness, contact area, and elastic modulus during indentation, Journal of Materials Research 7(03) (1992) 613-617.

[139] Y. Chen, S.R. Bakshi, A. Agarwal, Correlation between nanoindentation and nanoscratch properties of carbon nanotube reinforced aluminum composite coatings, Surface and Coatings Technology 204(16) (2010) 2709-2715.

[140] S. Nishikawa, S. Kikuchi, The diffraction of cathode rays by calcite, Proceedings of the Imperial Academy 4(8) (1928) 475-477.

[141] D. Chen, J.-C. Kuo, W.-T. Wu, Effect of microscopic parameters on EBSD spatial resolution, Ultramicroscopy 111(9) (2011) 1488-1494.

[142] S. Suzuki, Features of transmission EBSD and its application, JOM 65(9) (2013) 1254-1263.

[143] P.W. Trimby, Orientation mapping of nanostructured materials using transmission Kikuchi diffraction in the scanning electron microscope, Ultramicroscopy 120 (2012) 16-24.

[144] P.W. Trimby, Y. Cao, Z. Chen, S. Han, K.J. Hemker, J. Lian, X. Liao, P. Rottmann, S. Samudrala, J. Sun, Characterizing deformed ultrafine-grained and nanocrystalline materials using transmission Kikuchi diffraction in a scanning electron microscope, Acta Materialia 62 (2014) 69-80.

[145] A. Hodge, T. Furnish, C. Shute, Y. Liao, X. Huang, C. Hong, Y. Zhu, T. Barbee Jr, J. Weertman, Twin stability in highly nanotwinned Cu under compression, torsion and tension, Scripta Materialia 66(11) (2012) 872-877.

[146] Y.M. Wang, F. Sansoz, T. LaGrange, R.T. Ott, J. Marian, T.W. Barbee Jr, A.V. Hamza, Defective twin boundaries in nanotwinned metals, Nature Materials 12(8) (2013) 697-702.

[147] N. Li, J. Wang, X. Zhang, A. Misra, In-situ TEM study of dislocation-twin boundaries interaction in nanotwinned Cu films, JOM 63(9) (2011) 62-66.

[148] N. Li, J. Wang, J. Huang, A. Misra, X. Zhang, Influence of slip transmission on the migration of incoherent twin boundaries in epitaxial nanotwinned Cu, Scripta Materialia 64(2) (2011) 149-152.

[149] D. Bufford, Y. Liu, J. Wang, H. Wang, X. Zhang, In situ nanoindentation study on plasticity and work hardening in aluminium with incoherent twin boundaries, Nat Commun 5 (2014).

[150] X. Zhang, A. Misra, H. Wang, M. Nastasi, J. Embury, T. Mitchell, R. Hoagland, J. Hirth, Nanoscale-twinning-induced strengthening in austenitic stainless steel thin films, Applied Physics Letters 84(7) (2004) 1096-1098.

[151] X. Zhang, A. Misra, H. Wang, A. Lima, M. Hundley, R. Hoagland, Effects of deposition parameters on residual stresses, hardness and electrical resistivity of nanoscale twinned 330 stainless steel thin films, Journal of Applied Physics 97(9) (2005) 094302.

[152] Y. Liu, J. Jian, Y. Chen, H. Wang, X. Zhang, Plasticity and ultra-low stress induced twin boundary migration in nanotwinned Cu by in situ nanoindentation studies, Applied Physics Letters 104(23) (2014) 231910.

[153] X. Chen, L. Lu, Work hardening of ultrafine-grained copper with nanoscale twins, Scripta Materialia 57(2) (2007) 133-136.

[154] O. Anderoglu, A. Misra, J. Wang, R. Hoagland, J. Hirth, X. Zhang, Plastic flow stability of nanotwinned Cu foils, International Journal of Plasticity 26(6) (2010) 875-886.

[155] C. Shute, B. Myers, S. Xie, T. Barbee, A. Hodge, J. Weertman, Microstructural stability during cyclic loading of multilayer copper/copper samples with nanoscale twinning, Scripta Materialia 60(12) (2009) 1073-1077.

[156] C. Shute, B. Myers, S. Xie, S.-Y. Li, T. Barbee, A. Hodge, J. Weertman, Detwinning, damage and crack initiation during cyclic loading of Cu samples containing aligned nanotwins, Acta Materialia 59(11) (2011) 4569-4577.

[157] A. Hodge, T. Furnish, A. Navid, T. Barbee, Shear band formation and ductility in nanotwinned Cu, Scripta Materialia 65(11) (2011) 1006-1009.

[158] V. Narayanan, S. Mahajan, K. Bachmann, V. Woods, N. Dietz, Stacking faults and twins in gallium phosphide layers grown on silicon, Philosophical Magazine A 82(4) (2002) 685-698.

[159] Q. Xue, X. Liao, Y. Zhu, G. Gray, Formation mechanisms of nanostructures in stainless steel during high-strain-rate severe plastic deformation, Materials Science and Engineering: A 410 (2005) 252-256.

[160] K.-C. Chen, W.-W. Wu, C.-N. Liao, L.-J. Chen, K. Tu, Observation of atomic diffusion at twin-modified grain boundaries in copper, Science 321(5892) (2008) 1066-1069.

[161] D. Jang, C. Cai, J.R. Greer, Influence of homogeneous interfaces on the strength of 500 nm diameter Cu nanopillars, Nano Letters 11(4) (2011) 1743-1746.

[162] K. Lu, F. Yan, H. Wang, N. Tao, Strengthening austenitic steels by using nanotwinned austenitic grains, Scripta Materialia 66(11) (2012) 878-883.

[163] H.-Y. Hsiao, C.-M. Liu, H.-w. Lin, T.-C. Liu, C.-L. Lu, Y.-S. Huang, C. Chen, K. Tu, Unidirectional growth of microbumps on (111)-oriented and nanotwinned copper, Science 336(6084) (2012) 1007-1010.

[164] R. Ott, J. Geng, M. Besser, M. Kramer, Y. Wang, E. Park, R. LeSar, A. King, Optimization of strength and ductility in nanotwinned ultra-fine grained Ag: Twin density and grain orientations, Acta Materialia 96 (2015) 378-389.

[165] S. Mahajan, C.S. Pande, M.A. Imam, B.B. Rath, Formation of annealing twins in f.c.c. crystals, Acta Materialia 45(6) (1997) 2633-2638.

[166] M. Chen, E. Ma, K.J. Hemker, H. Sheng, Y. Wang, X. Cheng, Deformation twinning in nanocrystalline aluminum, Science 300(5623) (2003) 1275-1277.

[167] Z. Budrovic, H. Van Swygenhoven, P.M. Derlet, S. Van Petegem, B. Schmitt, Plastic deformation with reversible peak broadening in nanocrystalline nickel, Science 304(5668) (2004) 273-276.

[168] X. Liao, Y. Zhao, S. Srinivasan, Y. Zhu, R. Valiev, D. Gunderov, Deformation twinning in nanocrystalline copper at room temperature and low strain rate, Applied Physics Letters 84(4) (2004) 592-594.

[169] B. Li, B. Cao, K. Ramesh, E. Ma, A nucleation mechanism of deformation twins in pure aluminum, Acta Materialia 57(15) (2009) 4500-4507.

[170] X. Zhang, D. BUFFORD, H. Wang, Y. Liu, Method for producing high stacking fault energy (sfe) metal films, foils, and coatings with high-density nanoscale twin boundaries, Google Patents, 2014.

[171] X. Zhang, O. Anderoglu, A. Misra, H. Wang, Influence of deposition rate on the formation of growth twins in sputter-deposited 330 austenitic stainless steel films, Applied Physics Letters 90(15) (2007) 153101.

[172] I. Petrov, P. Barna, L. Hultman, J. Greene, Microstructural evolution during film growth, Journal of Vacuum Science & Technology A 21(5) (2003) S117-S128.

[173] A.H. Cottrell, Dislocations and plastic flow in crystals, Oxford : Clarendon Press, 1953.1953.

[174] S. Lee, J. Im, Y. Yoo, E. Bitzek, D. Kiener, G. Richter, B. Kim, S.H. Oh, Reversible cyclic deformation mechanism of gold nanowires by twinning–detwinning transition evidenced from in situ TEM, Nature Communications 5 (2014).

[175] F. Frank, W. Read Jr, Multiplication processes for slow moving dislocations, Physical Review 79(4) (1950) 722.

[176] J.P. Hirth, The influence of grain boundaries on mechanical properties, Metallurgical Transactions 3(12) (1972) 3047-3067.

[177] A.M. Minor, S.S. Asif, Z. Shan, E.A. Stach, E. Cyrankowski, T.J. Wyrobek, O.L. Warren, A new view of the onset of plasticity during the nanoindentation of aluminium, Nature Materials 5(9) (2006) 697-702.

[178] S.H. Oh, M. Legros, D. Kiener, G. Dehm, In situ observation of dislocation nucleation and escape in a submicrometre aluminium single crystal, Nature Materials 8(2) (2009) 95-100.

[179] J. Wang, O. Anderoglu, J.P. Hirth, A. Misra, X. Zhang, Dislocation structures of Σ3 {112} twin boundaries in face centered cubic metals, Applied Physics Letters 95(2) (2009) 021908.

[180] S. Xue, Z. Fan, Y. Chen, J. Li, H. Wang, X. Zhang, The formation mechanisms of growth twins in polycrystalline Al with high stacking fault energy, Acta Materialia 101 (2015) 62-70.

[181] J.-H. Lee, P.E. Loya, J. Lou, E.L. Thomas, Dynamic mechanical behavior of multilayer graphene via supersonic projectile penetration, Science 346(6213) (2014) 1092-1096.

[182] J.-H. Lee, D. Veysset, J.P. Singer, M. Retsch, G. Saini, T. Pezeril, K.A. Nelson, E.L. Thomas, High strain rate deformation of layered nanocomposites, Nature Communications 3 (2012) 1164.

[183] R. Thevamaran, O. Lawal, S. Yazdi, S.-J. Jeon, J.-H. Lee, E.L. Thomas, Dynamic creation and evolution of gradient nanostructure in single-crystal metallic microcubes, Science 354(6310) (2016) 312-316.

[184] D. Hull, D.J. Bacon, Introduction to dislocations. 5th ed. by Derek Hull and D.J. Bacon, Oxford : Butterworth-Heinemann, 2011.

[185] F.A. Mohamed, T.G. Langdon, Deformation mechanism maps based on grain size, Metallurgical Transactions 5(11) (1974) 2339-2345.

[186] H. Hu, L. Zhen, L. Yang, W. Shao, B. Zhang, Deformation behavior and microstructure evolution of 7050 aluminum alloy during high temperature deformation, Materials Science and Engineering: A 488(1) (2008) 64-71.

[187] B. Li, M. Sui, B. Li, E. Ma, S. Mao, Reversible twinning in pure aluminum, Physical Review Letters 102(20) (2009) 205504.

[188] F. Mompiou, D. Caillard, M. Legros, H. Mughrabi, In situ TEM observations of reverse dislocation motion upon unloading in tensile-deformed UFG aluminium, Acta Materialia 60(8) (2012) 3402-3414.

[189] T.C. Germann, B.L. Holian, P.S. Lomdahl, R. Ravelo, Orientation dependence in molecular dynamics simulations of shocked single crystals, Physical review letters 84(23) (2000) 5351-5354.

[190] R. Chau, J. Stölken, P. Asoka-Kumar, M. Kumar, N. Holmes, Shock Hugoniot of single crystal copper, Journal of Applied Physics 107(2) (2010) 023506.

[191] C. Ruestes, E. Bringa, A. Stukowski, J.R. Nieva, Y. Tang, M. Meyers, Plastic deformation of a porous bcc metal containing nanometer sized voids, Computational Materials Science 88 (2014) 92-102.

[192] N. Gunkelmann, Y. Rosandi, C.J. Ruestes, E.M. Bringa, H.M. Urbassek, Compaction and plasticity in nanofoams induced by shock waves: A molecular dynamics study, Computational Materials Science 119 (2016) 27-32.

[193] C.-H. Lu, B. Remington, B. Maddox, B. Kad, H.-S. Park, M. Kawasaki, T. Langdon, M. Meyers, Laser compression of nanocrystalline tantalum, Acta Materialia 61(20) (2013) 7767-7780.

[194] K. Kadau, T.C. Germann, P.S. Lomdahl, R.C. Albers, J.S. Wark, A. Higginbotham, B.L. Holian, Shock waves in polycrystalline iron, Physical Review Letters 98(13) (2007) 135701.

[195] J. Winey, A. Kubota, Y. Gupta, A thermodynamic approach to determine accurate potentials for molecular dynamics simulations: thermoelastic response of aluminum, Modelling and Simulation in Materials Science and Engineering 17(5) (2009) 055004.

[196] J. Wang, Atomistic simulations of dislocation pileup: grain boundaries interaction, JOM 67(7) (2015) 1515-1525.

[197] S. Vercammen, B. Blanpain, B. De Cooman, P. Wollants, Cold rolling behaviour of an austenitic Fe–30Mn–3Al–3Si TWIP-steel: the importance of deformation twinning, Acta Materialia 52(7) (2004) 2005-2012.

[198] I. Gutierrez-Urrutia, D. Raabe, Dislocation and twin substructure evolution during strain hardening of an Fe–22wt.% Mn–0.6 wt.% C TWIP steel observed by electron channeling contrast imaging, Acta Materialia 59(16) (2011) 6449-6462.

[199] H. Idrissi, K. Renard, L. Ryelandt, D. Schryvers, P. Jacques, On the mechanism of twin formation in Fe–Mn–C TWIP steels, Acta Materialia 58(7) (2010) 2464-2476.

[200] O. Grässel, L. Krüger, G. Frommeyer, L. Meyer, High strength Fe–Mn–(Al, Si) TRIP/TWIP steels development—properties—application, International Journal of Plasticity 16(10) (2000) 1391-1409.

[201] J. Pons, V. Chernenko, R. Santamarta, E. Cesari, Crystal structure of martensitic phases in Ni–Mn–Ga shape memory alloys, Acta Materialia 48(12) (2000) 3027-3038.

[202] K. Oikawa, T. Ota, T. Ohmori, Y. Tanaka, H. Morito, A. Fujita, R. Kainuma, K. Fukamichi, K. Ishida, Magnetic and martensitic phase transitions in ferromagnetic Ni–Ga–Fe shape memory alloys, Applied Physics Letters 81(27) (2002) 5201-5203.

[203] Y. Liu, I. Karaman, H. Wang, X. Zhang, Two Types of Martensitic Phase Transformations in Magnetic Shape Memory Alloys by In ‐ Situ Nanoindentation Studies, Advanced Materials 26(23) (2014) 3893-3898.

[204] G. Arlt, Twinning in ferroelectric and ferroelastic ceramics: stress relief, Journal of Materials Science 25(6) (1990) 2655-2666.

[205] B. Wang, E. Shi, W. Zhong, Twinning morphologies and mechanisms of ZnO crystallites under hydrothermal conditions, Crystal Research and Technology 33(6) (1998) 937-941.

[206] X. Li, S. Yin, S.H. Oh, H. Gao, Hardening and toughening mechanisms in nanotwinned ceramics, Scripta Materialia 133 (2017) 105-112.

[207] Y.A. Shin, S. Yin, X. Li, S. Lee, S. Moon, J. Jeong, M. Kwon, S.J. Yoo, Y.-M. Kim, T. Zhang, Nanotwin-governed toughening mechanism in hierarchically structured biological materials, Nature Communications 7 (2016).

[208] J. Wang, X. Zhang, Twinning effects on strength and plasticity of metallic materials, MRS Bulletin 41(04) (2016) 274-281.

[209] J.H. Lee, T.B. Holland, A.K. Mukherjee, X. Zhang, H. Wang, Direct observation of Lomer-Cottrell Locks during strain hardening in nanocrystalline nickel by in situ TEM, Scientific Reports 3 (2013) 1061.

[210] T. Zhu, H. Gao, Plastic deformation mechanism in nanotwinned metals: an insight from molecular dynamics and mechanistic modeling, Scripta Materialia 66(11) (2012) 843-848.

[211] Y. Wei, Y. Li, L. Zhu, Y. Liu, X. Lei, G. Wang, Y. Wu, Z. Mi, J. Liu, H. Wang, Evading the strength–ductility trade-off dilemma in steel through gradient hierarchical nanotwins, Nature Communications 5 (2014).

[212] L. Zhu, H. Ruan, X. Li, M. Dao, H. Gao, J. Lu, Modeling grain size dependent optimal twin spacing for achieving ultimate high strength and related high ductility in nanotwinned metals, Acta Materialia 59(14) (2011) 5544-5557.

[213] G. Gray, J. Huang, Influence of repeated shock loading on the substructure evolution of 99.99 wt.% aluminum, Materials Science and Engineering: A 145(1) (1991) 21-35.

[214] Y. Shao, S. Wang, Quasicontinuum study on formation of fivefold deformation twin in nanocrystalline aluminum, Scripta Materialia 62(6) (2010) 419-422.

[215] D.C. Bufford, Y.M. Wang, Y. Liu, L. Lu, Synthesis and microstructure of electrodeposited and sputtered nanotwinned face-centered-cubic metals, MRS Bulletin 41(04) (2016) 286-291.

[216] K. Yu, Y. Liu, S. Rios, H. Wang, X. Zhang, Strengthening mechanisms of Ag/Ni immiscible multilayers with fcc/fcc interface, Surface and Coatings Technology 237 (2013) 269-275.

[217] W.C. Oliver, G.M. Pharr, Measurement of hardness and elastic modulus by instrumented indentation: Advances in understanding and refinements to methodology, Journal of Materials Research 19(01) (2004) 3-20.

[218] J. Van der Merwe, C. Ball, J. Matthews, Epitaxial Growth, JW Matthews (Academic, New York, 1975) (1975) 494.

[219] L. Bobb, H. Holloway, K. Maxwell, E. Zimmerman, Oriented growth of semiconductors—II homoepitaxy of gallium arsenide, Journal of Physics and Chemistry of Solids 27(10) (1966) 1679-1685.

[220] B.M. McSkimming, A. Alexander, M.H. Samuels, B. Arey, I. Arslan, C.J. Richardson, Metamorphic growth of relaxed single crystalline aluminum on silicon (111), Journal of Vacuum Science & Technology A: Vacuum, Surfaces, and Films 35(2) (2017) 021401.

[221] L. Velasco, A.M. Hodge, Growth twins in high stacking fault energy metals: Microstructure, texture and twinning, Materials Science and Engineering: A 687 (2017) 93-98.

[222] J. Eady, L. Hogan, Some crystallographic observations of growth-twinned dendrites in aluminium, Journal of Crystal Growth 23(2) (1974) 129-136.

[223] M. Hall, M. Thompson, Epitaxy and twinning in foils of some noble metals condensed upon lithium fluoride and mica, British Journal of Applied Physics 12(9) (1961) 495-498.

[224] S. Ino, S. Ogawa, Multiply twinned particles at earlier stages of gold film formation on alkalihalide crystals, Journal of the Physical Society of Japan 22(6) (1967) 1365-1374.

[225] S. Ino, Stability of multiply-twinned particles, Journal of the Physical Society of Japan 27(4) (1969) 941-953.

[226] C. Hetherington, U. Dahmen, J. Penisson, Atomic Structure of Interfaces in Mazed Au Bicrystals, MRS Proceedings, Cambridge Univ Press, 1996, p. 215.

[227] K. Westmacott, S. Hinderberger, T. Radetic, U. Dahmen, PVD growth of fcc metal films on single crystal Si and Ge substrates, MRS Proceedings, Cambridge Univ Press, 1999, p. 583.

[228] N. Thangaraj, K. Westmacott, U. Dahmen, Epitaxial growth of (011) Al on (100) Si by vapor deposition, Applied Physics Letters 61(1) (1992) 37-39.

[229] D. Cherns, G. Anstis, J. Hutchison, J. Spence, Atomic structure of the NiSi2/(111) Si interface, Philosophical Magazine A 46(5) (1982) 849-862.

[230] N. Tsuji, Y. Ito, Y. Saito, Y. Minamino, Strength and ductility of ultrafine grained aluminum and iron produced by ARB and annealing, Scripta Materialia 47(12) (2002) 893-899.

[231] R. Hayes, D. Witkin, F. Zhou, E. Lavernia, Deformation and activation volumes of cryomilled ultrafine-grained aluminum, Acta Materialia 52(14) (2004) 4259-4271.

[232] J. Hirsch, Recent development in aluminium for automotive applications, Transactions of Nonferrous Metals Society of China 24(7) (2014) 1995-2002.

[233] J. Hirsch, T. Al-Samman, Superior light metals by texture engineering: optimized aluminum and magnesium alloys for automotive applications, Acta Materialia 61(3) (2013) 818-843.

[234] M.E. Fine, Precipitation hardening of aluminum alloys, Metallurgical and Materials Transactions A 6(4) (1975) 625-630.

[235] J. Park, A. Ardell, Correlation between microstructure and calorimetric behavior of aluminum alloy 7075 and Al · Zn · Mg alloys in various tempers, Materials Science and Engineering: A 114 (1989) 197-203.

[236] D. Richard, P.N. Adler, Calorimetric studies of 7000 series aluminum alloys: I. Matrix precipitate characterization of 7075, Metallurgical and Materials Transactions A 8(7) (1977) 1177-1183.

[237] L.K. Berg, J. Gjønnes, V. Hansen, X.Z. Li, M. Knutson-Wedel, G. Waterloo, D. Schryvers, L.R. Wallenberg, GP-zones in Al–Zn–Mg alloys and their role in artificial aging, Acta Materialia 49(17) (2001) 3443-3451.

[238] H. Chen, B. Yang, Effect of precipitations on microstructures and mechanical properties of nanostructured Al-Zn-Mg-Cu alloy, Materials transactions 49(12) (2008) 2912-2915.

[239] P. Chowdhury, H. Sehitoglu, H. Maier, R. Rateick, Strength prediction in NiCo alloys–the role of composition and nanotwins, International Journal of Plasticity 79 (2016) 237-258.

[240] K. Youssef, R. Scattergood, K. Murty, C. Koch, Nanocrystalline Al–Mg alloy with ultrahigh strength and good ductility, Scripta Materialia 54(2) (2006) 251-256.

[241] C. Koch, R. Scattergood, K. Darling, J. Semones, Stabilization of nanocrystalline grain sizes by solute additions, Journal of Materials Science 43(23-24) (2008) 7264-7272.

[242] T. Chookajorn, H.A. Murdoch, C.A. Schuh, Design of stable nanocrystalline alloys, Science 337(6097) (2012) 951-954.

[243] A. Detor, C. Schuh, Microstructural evolution during the heat treatment of nanocrystalline alloys, Journal of Materials Research 22(11) (2007) 3233-3248.

[244] A.J. Detor, C.A. Schuh, Tailoring and patterning the grain size of nanocrystalline alloys, Acta Materialia 55(1) (2007) 371-379.

[245] S. Zhao, C. Meng, F. Mao, W. Hu, G. Gottstein, Influence of severe plastic deformation on dynamic strain aging of ultrafine grained Al–Mg alloys, Acta Materialia 76 (2014) 54-67.

[246] P.V. Liddicoat, X.-Z. Liao, Y. Zhao, Y. Zhu, M.Y. Murashkin, E.J. Lavernia, R.Z. Valiev, S.P. Ringer, Nanostructural hierarchy increases the strength of aluminium alloys, Nature Communications 1 (2010) 63.

[247] R.Z. Valiev, Y. Estrin, Z. Horita, T.G. Langdon, M.J. Zehetbauer, Y. Zhu, Producing bulk ultrafine-grained materials by severe plastic deformation: ten years later, JOM 68(4) (2016) 1216-1226.

[248] T.J. Rupert, J.C. Trenkle, C.A. Schuh, Enhanced solid solution effects on the strength of nanocrystalline alloys, Acta Materialia 59(4) (2011) 1619-1631.

[249] C. Koch, D. Morris, K. Lu, A. Inoue, Ductility of nanostructured materials, MRS Bulletin 24(02) (1999) 54-58.

[250] Y. Wang, M. Chen, F. Zhou, E. Ma, High tensile ductility in a nanostructured metal, Nature 419(6910) (2002) 912-915.

[251] R. Valiev, Nanostructuring of metals by severe plastic deformation for advanced properties, Nature Materials 3(8) (2004) 511-516.

[252] M. Mata, J. Alcala, Mechanical property evaluation through sharp indentations in elastoplastic and fully plastic contact regimes, Journal of Materials Research 18(07) (2003) 1705-1709.

[253] P. Gallagher, The influence of alloying, temperature, and related effects on the stacking fault energy, Metallurgical Transactions 1(9) (1970) 2429-2461.

[254] O. Johari, G. Thomas, Substructures in explosively deformed Cu and Cu-Al alloys, Acta Metallurgica 12(10) (1964) 1153-1159.

[255] A. Rohatgi, K.S. Vecchio, G.T. Gray, The influence of stacking fault energy on the mechanical behavior of Cu and Cu-Al alloys: deformation twinning, work hardening, and dynamic recovery, Metallurgical and Materials Transactions A 32(1) (2001) 135-145.

[256] Y. Zhang, N.R. Tao, K. Lu, Effect of stacking-fault energy on deformation twin thickness in Cu–Al alloys, Scripta Materialia 60(4) (2009) 211-213.

[257] M. Chandran, S. Sondhi, First-principle calculation of stacking fault energies in Ni and Ni-Co alloy, Journal of Applied Physics 109(10) (2011) 103525.

[258] T. Schulthess, P. Turchi, A. Gonis, T.-G. Nieh, Systematic study of stacking fault energies of random Al-based alloys, Acta Materialia 46(6) (1998) 2215-2221.

[259] G.H. Campbell, D.K. Chan, D.L. Medlin, J.E. Angelo, C.B. Carter, Dynamic observation of the fcc to 9r shear transformation in a copper $\Sigma = 3$ incoherent twin boundary, Scripta Materialia 35(7) (1996) 837-842.

[260] J. Gu, L. Zhang, S. Ni, M. Song, Formation of large scaled zero-strain deformation twins in coarse-grained copper, Scripta Materialia 125 (2016) 49-53.

[261] R.L. Fleischer, Solution hardening by tetragonal dist ortions: Application to irradiation hardening in F.C.C. crystals, Acta Metallurgica 10(9) (1962) 835-842.

[262] R.L. Fleischer, Substitutional solution hardening, Acta Metallurgica 11(3) (1963) 203-209.